ELECTRICAL CHARACTERIZATION OF A THREE-PHASE, TRACER, INJECTION TEST

A Dissertation

Presented in Partial Fulfillment of the Requirements for the

Degree of Doctor of Philosophy

with a

Major in Geology

in the

College of Graduate Studies

University of Idaho

by

Robin E. Nimmer

December, 2005

Major Professor: James L. Osiensky, Ph.D.

UMI Number: 3196089

INFORMATION TO USERS

The quality of this reproduction is dependent upon the quality of the copy submitted. Broken or indistinct print, colored or poor quality illustrations and photographs, print bleed-through, substandard margins, and improper alignment can adversely affect reproduction.

In the unlikely event that the author did not send a complete manuscript and there are missing pages, these will be noted. Also, if unauthorized copyright material had to be removed, a note will indicate the deletion.
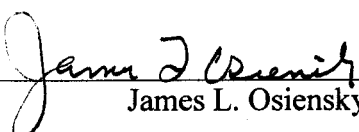
UMI®
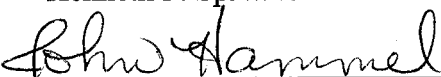
AUTHORIZATION TO SUBMIT DISSERTATION

This dissertation of Robin E. Nimmer, submitted for the degree of Doctor of Philosophy with a major in Geology and titled "Electrical Characterization of a Three-Phase, Tracer, Injection Test." has been reviewed in final form, 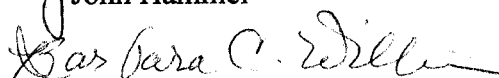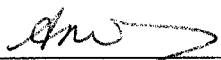as indicated by the signatures and dates given below. Permission is now granted to submit final copies to the College of Graduate Studies for approval.
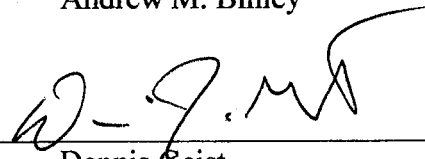
Major Professor _____ Date _12-14-05_
James L. Osiensky
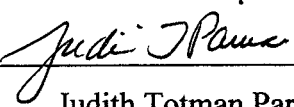
Committee Members _____ Date _12/6/05_
Kenneth F. Sprenke

_____ Date _12/6/05_
John Hammel

_____ Date _12/14/05_
Barbara C. Williams

_____ Date _12/8/05_
Andrew M. Binley

Department
Administrator _____ Date _12/14/05_
Dennis Geist

Discipline's
College Dean _____ Date _12/14/05_
Judith Totman Parrish

Final Approval and Acceptance by the College of Graduate Studies

_____ Date _1-2-06_
Margrit von Braun

ABSTRACT

A three-phase, radial-injection, tracer experiment was conducted from November, 1999 to April, 2000 in partially saturated, fractured basalt on the University of Idaho campus. Phase 1 characterizes the injection of potassium chloride (KCl) solution into a centrally located injection well in the partially saturated zone for 76 days. Phase 2 represents monitoring during the dilution of the KCl plume by 34 days of tap-water injection. A 63-day monitoring period composes Phase 3. The test was monitored using electrical, geophysical methods: mise-à-la-masse (MALM), self-potential (SP) and electrical resistance tomography (ERT).

Hole-surface and hole-hole MALM measurements and surface SP measurements were analyzed for changes over time. Contour maps of changes from baseline show that hole-surface MALM was able to track the lateral evolution of the tracer plume; however, SP measurements proved to be inconclusive due to noise and variability. The hole-hole MALM measurements helped delineate the depth of preferential tracer migration in the fractured basalt. SP and MALM methods were fairly insensitive to the tap-water injection.

Surface and cross-hole ERT data were analyzed to monitor dilution and displacement of the plume during Phases 2 and 3. A problem with current leakage due to faulty wiring plagued Phase 1. Images of surface ERT delineated areas of increased and decreased resistivities. Increasing resistivities are attributed to dilution/displacement of the KCl solution by tap-water invasion or the influx of seasonal recharge. Decreasing resistivities resulted from migration of the residual KCl solution. Cross-borehole ERT was conducted between the injection well and each of seven observation wells. The data were then inverted to evaluate changes in resistivity. Resistivity changes at the injection well suggest elevations and directions where tap water migrated away from the injection well. Observation well resistivities show increases and decreases at specific locations and in clusters owing to dilution by tap water or recharge water, and redistribution of the KCl, respectively.

Finite-element, forward modeling of ERT was conducted to evaluate the effects of a 3-D heterogeneity by a 2-D inversion model. 3-D effects as image artifacts include 1) borehole inversion effects (BIE), examined by simulating two boreholes with a resistivity

contrast to the host medium; a target heterogeneity was included in certain simulations, and 2) shadow effects (SE), examined by moving a target out of the image plane. BIE were shown to increase as the resistivity contrast of the fill and borehole diameter increased. The imaged location of target heterogeneities also was affected by BIE. However, ratios of time-sequenced data significantly reduced BIE. SE were found to be related to the target distance out of the image plane to a limit beyond which the effects become insignificant.

ACKNOWLEDGEMENTS

DEDICATION

I dedicate this work to every teacher throughout my life, each with their own unique influence.

TABLE OF CONTENTS

LIST OF TABLES

LIST OF FIGURES

CHAPTER 1. INTRODUCTION

Detection and monitoring of contaminants within the vadose zone is part of an important early warning system to prevent ground-water contamination. A conductive contaminant plume (e.g. inorganic contaminants) with liquid phase continuity throughout will provide conductive pathways for the flow of current that correspond approximately to the hydraulic pathways through which the plume evolved. The need exists to test the application of electrical, geophysical methods to detect and monitor the evolutionary dynamics of conductive plumes within vadose zones in fractured rock.

A long-term, radial injection, tracer test was conducted in the shallow, fractured basalt vadose zone using an electrolyte tracer. The expected benefit of the study was the development of a better understanding of the electrical signatures that develop due to current channeling through conductive contaminant plumes in variably saturated media. The objective of this study was to conduct a field experiment in the vadose zone in fractured basalt to test the degree to which four electrical geophysical methods can track the migration of potassium chloride (KCl) solution and tap water from an injection well, and to determine the migration pathways of the fluids through these electrical signatures.

1.1 Electrical methods description

The field experiment was designed to test self potential (SP), mise-à-la-masse (MALM), surface electrical resistance tomography (ERT), and cross-borehole ERT methods to track spatial changes in voltages and resistivity over time as a conductive plume evolved. SP and hole-surface MALM provide areal images of voltages. Hole-hole MALM provides downhole voltages. Surface ERT affords 3-D resistivity images. Cross-sectional images of resistivity are supplied by cross-borehole ERT. Other electrical methods including resistivity survey lines were not part of the experimental design due to limited resources.

1.1.1 SP

Self potentials (SP) commonly are considered to be noise that is to be separated from measurements of voltage during electrical resistivity surveys. SP are electrical potentials that develop in the earth by fluid streaming, bioelectric activity in vegetation, varying electrolytic concentrations in ground water, telluric currents and other geochemical actions (Telford, et al. 1990). However, when non-polarizing potential electrodes (surface or downhole) are used, measurement of SP generally is standard practice and may provide useful information for environmental applications. SP varies over time because of natural (telluric) currents in the ground caused by changing ionospheric currents (Sharma, 1986).

1.1.2 MALM

MALM is also called the "charged-body potential" method. MALM is a variation of galvanic resistivity methods and was developed originally to map electrically conductive earth materials by passing a current directly into the zone of interest while electrical potentials are measured at the land surface or in boreholes (Parasnis, 1967). The MALM method allows for the direct measurement of voltages about a single, point source of electric current imbedded in the conductive body of interest. The resulting voltage distribution for an area of investigation incorporates all factors that contribute to its development at the particular time of measurement.

1.1.3 Surface ERT

The 3-D nature of geologic structures invites the use of a 3-D resistivity technique and inversion routine to provide 3-D interpretation of the data. Surface ERT is a three-dimensional, electrical, imaging technique where the electrodes are located at land surface arranged in a rectangular grid. This method uses a two to four-electrode array to measure resistances, which are then inverted to generate a 3-D resistivity distribution.

1.1.4 Cross-borehole ERT

Cross-borehole ERT provides images of the subsurface resistivity distribution in the intervening space between two wells. Electrodes are located downhole and may also be located at land surface. This method uses a two to four-electrode array to measure a large number of resistances by applying sequences of exciting and recording potential differences to multiple electrode pairs. The resistance data are inverted to generate a resistivity distribution or tomogram.

1.2 Field site and tracer test

It was the original intention of the study to conduct an injection experiment near a rock face where electrodes were installed directly into the cliff face. Approximately a 15-mile radius was searched for such a site, though none were chosen due to access problems or lack of electricity. Consequently, a non-cliff site was selected on the University of Idaho campus in Moscow, Idaho on a College of Agricultural and Life Sciences cow pasture, still posing obvious limitations (Figure 1.1). The field site is located on the north flank of a 12-m high hill about 100 m from the crest of the hill. To the east was a horse pasture. A trailer borrowed from the Idaho Geological Survey was placed on site to house equipment and for protection from the elements. Power for the trailer and equipment was accessed from a power pole near the top of the hill.

The experiment was conducted in the partially-saturated flow top of the uppermost basalt flow of the Wanapum Formation of the Columbia River Basalt Group. Depth to basalt was approximately 3 m at the field site. The basalt was overlain by clayey-silt layer (~0.3 m thick) and clean silt. Drill cuttings indicated both dense and weathered basalt underlie the field site.

Eight, 15.2-cm (6 in) diameter wells were drilled by air rotary by McPherson and Wright Well Drilling (Figure 1.2); seven penetrated perched water and one is believed to have penetrated the true water table. The injection well is centrally located and is the shallowest (4.6 m). Seven observation wells were drilled for water-level measurements,

water-sample collection for electrical conductivity measurements, neutron probe measurements and housing downhole electrodes. The deepest well is ES7 (7.5 m). Borehole video logs were recorded for each well prior to any well disturbance revealing many small fractures, but no obvious major fracture zones.

A total of 89 downhole electrodes were installed, but only 66 were used in the cross-borehole ERT experiments and hole-hole MALM. It was determined after the electrodes were in place that it would be beneficial to also have surface electrodes for use with ERT; however, there were only 100 available circuit switches (two switch boxes were not working).

The surface electrode field was comprised of three types of surface electrodes (Figure 1.2). MALM and SP used 224 porous-pot, land-surface electrodes on 1.3-m spacings about the injection well. Cross-borehole ERT used 34 stainless-steel, land-surface electrodes that were positioned along transects through the injection well and each observation well. Insulated copper wires were run from the downhole to inside the trailer. Inside the trailer, these wires were connected to 51 "switch boxes" (two electrodes to a switch box) on a connected string of 13 cables (4 switch boxes to a cable). The previously mentioned surface electrodes were permanent. Surface ERT used 100 brass, land-surface, stake electrodes on 1.3 m spacings alternating with the porous pot electrodes and were slightly off-center from the injection well; these electrodes were temporary, installed prior to data collection and removed following the last measurement.

The reference electrode was a porous pot; the distant current electrode consisted of three stainless-steel stakes connected by a copper wire. The reference electrode was placed 74.5 m to the west of the injection well. The distant current electrode was located 62.4 m to the southwest of the injection well. Land-use constraints prevented these electrodes from being placed closer to a distance at infinity. The reason for the close proximity of the distant current electrode and reference electrode to one another was the intended placement of a north-south trending fence near the east side of the trailer to cordon off the field site from cows. The animals were relocated so the fence was not installed.

Initially, the tracer experiment was expected to be completed in less than two weeks. The hydraulic conductivity was such that the injection flow rate was much slower than anticipated. Considering the length of time to collect the measurements this proved to be
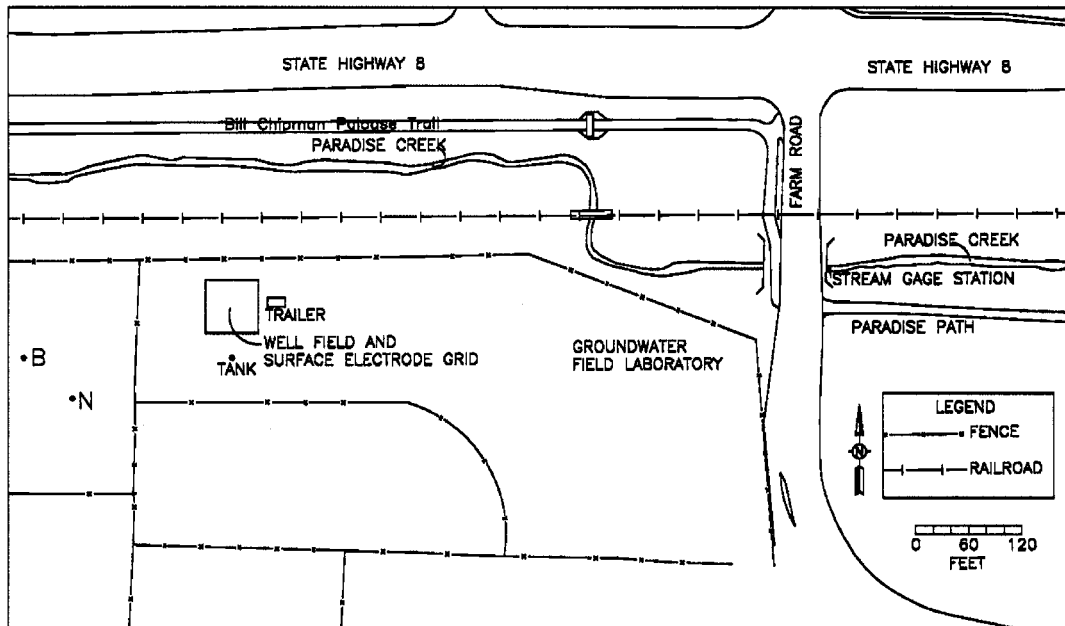
Figure 1.1. Site location of field experiment. B and N are distant electrodes.

KEY

- SP & MALM porous-pot electrode
- Cross-borehole ERT stainless-steel electrode
- Surface ERT brass electrode
- Well
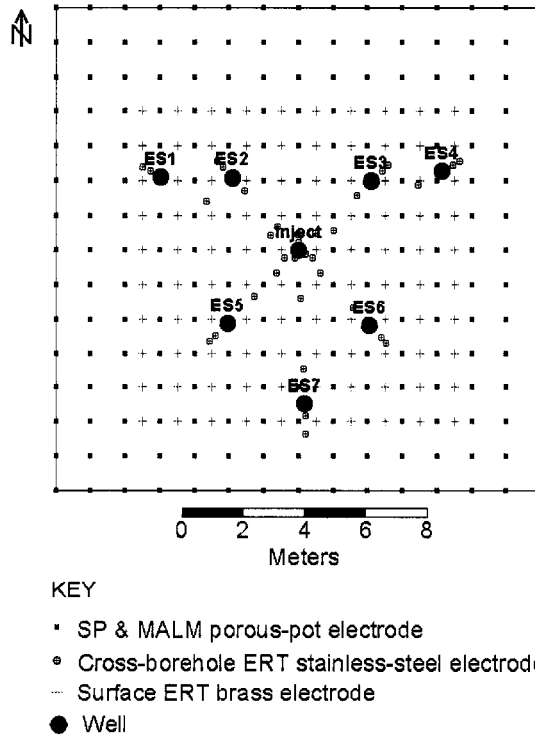
Figure 1.2. Well and surface-electrode locations (see Figure 1.1 for location of grid).

highly beneficial. A long-term, radial-injection, tracer experiment was conducted from November 6, 1999-April 27, 2000. The experiment endured rain, snow, sun, and mid-range to freezing temperatures. The experiment was divided into three phases. Phase 1 consisted of an injection of potassium chloride (KCl) solution for 76 days. At the beginning of the experiment (Phase 1; t=0 d), the injection well was filled to the top of the basalt with 34.8 liters (l) of the KCl solution, with a constant electrical conductivity of 0.601 siemens/meter (S/m). The water level was maintained in the well through a gravity feed drip system from a polyethylene tank located to the south of the electrode grid area. A total of 765 l of KCl solution was injected during Phase 1. Phase 2 began on January 19, 2000 immediately after the KCl tracer injection ended. Beginning on this day, day 77, saline water was pumped from the injection well, and the injection stream was changed to tap water with an electrical conductivity of 0.0294 S/m. Phase 2 of the experiment continued for a 34 days during which 342 l of tap water were injected. Phase 3, began on day 111 (February 24, 2000), and continued for 62 days until April 27, 2000.

1.3 Data collection

SP and MALM measurements were taken manually at each of the 224 porous pot electrodes by completing an electrical circuit through the distant current electrode to the receiver system that recorded all measurements. Potential electrodes for the hole-hole MALM, surface ERT and cross-borehole 3DSR were connected to switch boxes in the GISCO Multi-Electrode Cable System ME-100™. Voltages were measured automatically by program request. However, due to frequent system failures the data were saved manually on ten-minute intervals.

Over the duration of the experiment, electrical data sets were collected. SP's were measured 11 times. Baseline SP (data prior to the injection of KCl on November 6, 1999) values were measured on November 1 and November 5, 1999. MALM data were collected 19 times. Baseline MALM data were collected on October 27 and November 1, 1999. Cross-borehole ERT data were also collected 19 times. No baseline cross-borehole ERT data

were collected because all but one electrode in the injection well was above the water level; this precluded electrical connection. Surface ERT data were collected three times as weather and time permitted. Baseline surface ERT data were collected on October 30 and 31, 1999. Not all data are presented in this dissertation due to limited space available in the manuscripts written for publication and filtering of data known to be corrupted by various transmitter/receiver problems.

Non-electrical data were also collected before and during the experiment. Water levels were measured in each of the boreholes. During the unsaturated period of the experiment, measurements represented standing water in the borehole that seeped from fractures containing perched water. Soil temperatures and soil suction were also measured at the site. A neutron probe was used to measure wetness near the observation wells several times during the experiment; however rapidly rising water levels effectively precluded the collection of useful data. Water samples were collected for each of the observation wells during the experiment to document changes in electrical conductivity of the borehole waters.

1.4 Hypotheses

The experiment was designed to test several hypotheses regarding the application of the electrical geophysical methods within the partially saturated vadose zone in fractured basalt. The hypotheses are: 1) the addition of KCl solution would cause a definable SP anomaly to develop over time; 2) the injection of a direct MALM current into the source of an evolving KCl plume would allow the plume dynamics to be mapped over time; 3) surface ERT, because of the relatively large number of measurements, would provide complimentary information to the other methods on the evolution of the KCl plume dilution; 4) cross-borehole ERT between an injection well containing the source material, and several nearby observation wells, would provide detailed information on the KCl plume dilution over time.

1.5 Organization of dissertation

This dissertation is divided into seven chapters. Chapter 2 is a paper published in the journal, Environmental Geosciences, titled "Using mise-à-la-masse to delineate the migration of a conductive tracer in partially saturated basalt" (Nimmer and Osiensky, 2002a), and describes the results for the first 34 days of the hole-surface MALM experiment. Chapter 3 is the paper "Direct current and self potential monitoring of an evolving plume in partially saturated and fractured rock" (Nimmer and Osiensky, 2002b), published in the Journal of Hydrology, and describes the SP and MALM experiments. Chapter 4 consists of the paper, "Charged body potential monitoring of an electrolyte plume emanating from a dripping source" (Nimmer and Osiensky, 2003), published in Environmental Science and Health, Part A – Toxic/Hazardous Substances & Environmental Engineering. This paper also describes the MALM experiment, and was submitted for publication prior to the paper in Chapter 3. Chapter 5 is the manuscript "Electrical resistivity imaging of conductive plume dilution" (Nimmer et al., in review). This paper has been submitted for review to Hydrogeology Journal, and describes the ERT experiments. Chapter 6 consists of the manuscript "Three-dimensional effects in two-dimensional cross-borehole imaging" (Nimmer et al., in review). This paper has been submitted for review to the Journal of Applied Engineering and Environmental Geophysics (JEEG). This last paper is based on cross-borehole ERT hypothetical modeling, and is not directly related to the field experiment. Conclusions and recommendations are presented in Chapter 7.

References

Nimmer, R.E., and J.L. Osiensky. 2002a. Using mise-à-la-masse to delineate the migration of a conductive tracer in partially saturated basalt. Environmental Geosciences, Vol. 9, No. 2, pp. 81-87.

Nimmer, R.E., and J.L. Osiensky. 2002b. Direct current and self potential monitoring of an evolving plume in partially saturated fractured rock. Journal of Hydrology, Vol. 267, Nos. 3-4, pp. 258-272.

Nimmer, R.E., and J.L. Osiensky. 2003. Charged body potential monitoring of an electrolyte plume emanating from a dripping source. Environmental Science and Health, Part A – Toxic/Hazardous Substances & Environmental Engineering, Vol. A38, No. 5, pp. 737-752.

Nimmer, R.E., J.L. Osiensky, A.M. Binley, K.F. Sprenke and B.C. Williams. In Review. Electrical resistivity imaging of conductive plume dilution. Hydrogeology Journal.

Nimmer, R.E., J.L. Osiensky, and A.M. Binley. In Review. Three-dimensional effects in two-dimensional cross-borehole imaging. Journal of Engineering and Environmental Engineering.

Parasnis, D.S., 1967. Three-dimensional electric mise-à-la-masse survey of an irregular lead-zinc-copper deposit in central Sweden. Geophysical Prospecting, Vol. 15, No. 3, pp.407-437.

Sharma, P.W., 1986. Geophysical Methods in Geology. PTR Prentice-Hall, Inc., New Jersey.

Telford, W.M., Geldart, L.P., and Sheriff, R.E., 1990. Applied Geophysics. Cambridge University Press, United Kingdom.

CHAPTER 2. USING MISE-À-LA-MASSE TO DELINEATE THE MIGRATION OF A CONDUCTIVE TRACER IN PARTIALLY SATURATED BASALT[1]

Robin E. Nimmer and James L. Osiensky

Department of Geological Sciences, University of Idaho, Moscow, ID 83844-3022, USA

Abstract

Borehole-surface mise-à-la-masse (MALM) measurements were taken over time during a radial injection tracer experiment in partially saturated, fractured, Columbia River basalt. In this experiment, an enhanced conductivity tracer stream was energized directly through a current electrode placed in the bottom of the injection well. A constant concentration tracer solution of potassium chloride was injected continuously above a perched water table at an average rate of 10 liters/day under a constant hydraulic head for 34 days. An asymmetrical ground water mound developed over time during which electrical potential measurements were taken to delineate migration of the tracer. A 15 by 15 array of porous pot electrodes (copper sulfate), located symmetrically about the centrally located injection well, was used for the borehole-surface MALM. Ratios of electrical potentials/baseline were contoured over time to delineate anomalies caused by the presence of tracer solution in the fractured basalt. Borehole-surface measurements delineated the lateral migration of tracer over time and locations of clay filled fractures.

Key words: fractured rock, electrical resistivity, vadose zone, preferential flow paths, tracer test, mise-à-la-masse, vadose zone

---

2.1. Introduction

Delineation of preferential flow paths in saturated and unsaturated fractured media is pivotal to the success of remediation efforts to solve many subsurface contamination problems. Methods to delineate preferential flow paths typically are invasive and involve extensive drilling programs. These investigations are very expensive and are limited by the physical number of measurement points (i.e. boreholes).

Electrical geophysical methods may provide cost effective and noninvasive tools to help delineate preferential flow paths that contain fluids with contrasting electrical properties. In saturated and unsaturated porous media, the electrical properties are dominated by the porosity fraction and the conductivity of the fluids that exist in the pore spaces (Archie, 1942; Keller and Frischknecht, 1966). The presence of conductive fluids (e.g. inorganic contaminants) within the pore spaces will increase the electrical conductivity of porous media. The presence of resistive fluids (e.g. organic contaminants) will decrease the electrical conductivity of the media.

Many investigators (too numerous to list all here) have researched various surface and borehole-to-surface electrical methods to evaluate the migration characteristics of conductive tracer plumes. Fried (1975) describes the use of electrical resistivity measurements to evaluate the velocity and direction of migration of a sodium chloride tracer from a single well. Jaemtlid et al. (1984) use the mise-à-la-masse (MALM) method to delineate fracture zones in crystalline rock in Sweden. White (1988) describes use of the method of Fried (1975) in New Zealand. Sjostrom and Sill (1991) and Bevc and Morrison (1989) use borehole-to-surface electrical methods to track the movement of saline tracers in ground water. Asch and Morrison (1989) describe advantages of using combinations of surface and subsurface electrodes for electrical resistivity investigations. Wang et al. (1991) use borehole-to-surface MALM in an attempt to detect new fractures formed by hydraulic fracturing in an injection well. Osiensky (1995) and Osiensky and Donaldson (1995) describe a modified MALM experiment to delineate a tracer plume in fluvial sediments. Osiensky (1997) describes the use of the MALM method to define plume length and the location of the center of mass of hypothetical contaminant plumes. Greenhalgh and Shunhua

(1998) develop a formula for calculating the electrical potential distribution in a heterogeneous 2-D or 3-D earth for any number of current electrode sources or sinks.

According to Parasnis (1967), the MALM method, first suggested by Schlumberger (1920), can be interpreted as "excitation of the mass." MALM also is known as the charged body potential method. The MALM method is a variation of galvanic resistivity methods and was developed originally to delineate the extent of electrically anomalous zones in the subsurface. Specifically, the MALM method was designed to map an electrically conductive orebody by passing an electric current directly into the body while electrical potentials, under steady state conditions, are measured at the land surface or in boreholes (Parasnis, 1967). According to Ketola (1972), the entire conductive body acts as a current electrode and attains nearly the same potential.

The principle of the MALM method is to ground a single current electrode directly in a conductive body of earth materials. For this paper, the conductive body is a relatively conductive tracer plume emanating from a borehole filled with a conductive tracer solution. Access to the conductive body may be at the land surface or through boreholes. A second current electrode that serves as a current sink is driven into the ground at an infinite distance (i.e., far enough to have negligible influence) from the first current electrode. The circuit is completed through a wire connecting the two electrodes. In a typical MALM application, the electrical potentials (i.e., voltages) are measured at a movable potential electrode. Electrical potentials are measured with a high impedance voltmeter or with an electrical resistivity receiver. The measured electrical potential at each location represents the voltage difference between a fixed, reference, potential electrode (base station) and the movable potential electrode. The reference electrode generally is located at the land surface an infinite distance (i.e., for practical purposes, a large distance) from the area where electrical potentials are being measured. According to Ketola (1972), the actual position of the reference electrode should be selected by trial and error measurements so that the potential differences measured are positive.

The MALM method allows for the direct measurement of the electrical potential distribution for uncertain boundary conditions. The resulting electrical potential distribution for an area of investigation incorporates all factors that contribute to its development at the particular time of measurement. Where baseline data can be collected, subsequent data sets

can be compared for evaluation of changes that occur over time. If care is taken to collect subsequent data sets under similar conditions as the baseline data set (e.g., similar moisture contents and temperatures of surface soils, same depth to the water table, etc.), changes due to contaminant migration can be delineated.

The governing equation for the flow of electricity in a conductive medium is Ohm's Law given as:

$$J_x = -\sigma \frac{\partial V}{\partial x}$$ Eqn. 2.1

where: J_x is the current density (electrical current per unit area), σ is the electrical conductivity, and V is the electrical potential.

The electrical conductivity of porous media is given by the Archie (1942) formula as:

$$\sigma_m = a\sigma_w S^n \phi^m$$ Eqn. 2.2

where: ϕ is the porosity, S is the fraction of pores containing water (i.e., S=1 for complete saturation), σ_w is the electrical conductivity of the pore water, m is an empirical exponent based on the texture of the rock. Values range between 1.3 in loosely packed granular media to about 2.2 in well-cemented granular rocks (Parkhomenko, 1967), a and n are empirical constants used to force the formula to fit the behavior of the rock type of interest (Keller, 1987).

According to Keller (1987), for a given porosity and water saturation, fracture porosity typically will exhibit the highest rock conductivity due to the simpler shape of the pores while vuggy porosity will result in the lowest conductivity because of the complex pores. Changes in the electrical potential distribution that occur over time are due to changes in the electrical conductance of the porous medium through which the controlled electrical current is passed. If the effects of "noise" can be identified and separated from the measured electrical potentials, the differences between baseline and subsequent data sets will reflect changes in the moisture contents and the electrical conductivity of the pore water in accordance with the Archie (1942) formula.

2.2. Field demonstration

2.2.1 Site geology

The test site for this field demonstration is located on the University of Idaho campus in Moscow, Idaho along the eastern edge of the Columbia River Plateau within the Moscow-Pullman ground water basin. Two basalt formations of the Columbia River Basalt Group exist at the test site. The experiments were conducted in the uppermost basalt flow (i.e., the Lolo Flow of the Priest Rapids Member) of the Wanapum Formation, which dates to 14.5 million years ago (Bush and Seward, 1992).

The Lolo basalt flow is covered by 1.5 to 2 meters (m) of alluvial sediments and Pleistocene Palouse loess (Provant, 1995). The loess is comprised of eolian volcanic, glacio-fluvial and glacio-lacustrine sediments. The alluvial sediments are made up of reworked loess with basalt and granite fragments. An approximately 0.5 m thick layer of clay forms the sediment-basalt contact at the research site.

The Lolo basalt flow has a weathered and fractured, vesicular flow top overlying a more massive interior. Fractures near the surface typically are filled with clay due to weathering of the basalt. Fractures deeper in the flow contain less clay. The field experiment was conducted in the upper portion of the flow. Many of the fractures at the test site are filled with clay. The amount of clay in the fractures affects the flow of electricity and the open area available for water flow. A more detailed description of the Lolo flow structure at the research site is presented in Nimmer et al. (2001a).

2.2.2 Tracer test

A 173-day, time-series field experiment was completed using borehole-surface MALM to track an evolving, vadose zone, tracer plume in the weathered, fractured, Lolo basalt flow. The tracer test began on November 6, 1999 and extended to April 27, 2000. This paper is limited to the borehole-surface MALM data collected during the first 34 days of the experiment.

A centrally located, vadose zone, injection well was drilled with air-rotary on the University of Idaho campus specifically for these experiments (Figure 2.1). The well was
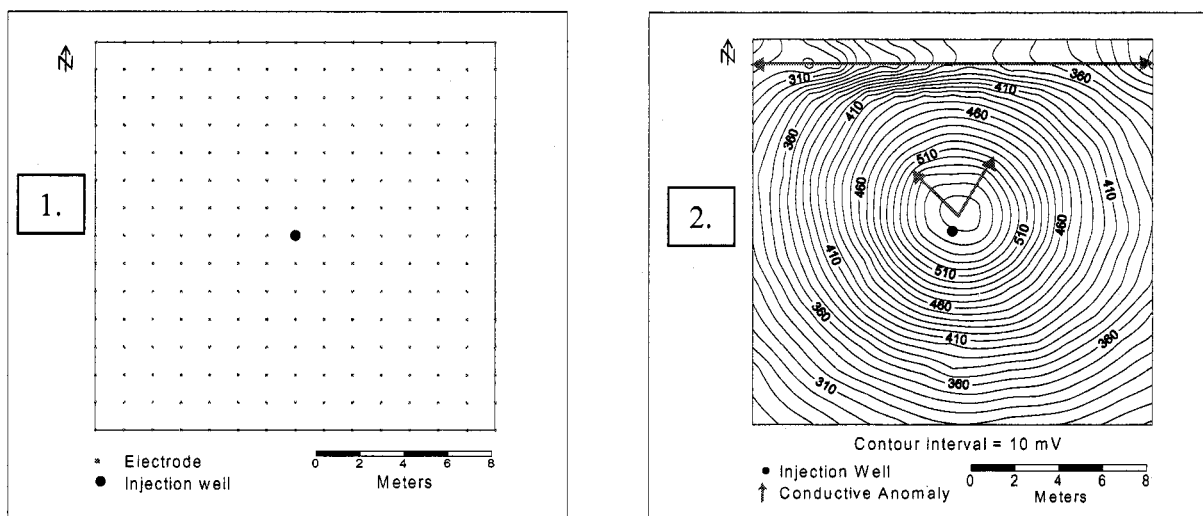
Figure 2.1. Site location map of the injection well and porous pot electrodes for the tracer experiment.

Figure 2.2. Contour map of baseline electrical potentials at the test site (t = 0 days).

constructed with 0.15 m diameter schedule 80 PVC surface casing through the sediments and is open hole in the basalt. The bottom of the well is 4.575 m below ground surface; the completion depth was based on the depth of perched ground water relative to a gently sloping land surface. A copper wire current electrode was placed in the center of the injection well 10 cm above the bottom of the hole on a 0.013 m (0.5 in) diameter schedule 40 PVC pipe. The insulated wire was run up the outside of the PVC pipe to the land surface for direct connection to a receiver/transmitter system.

Baseline and time-series electrical potentials were measured by the borehole-surface MALM method using a fixed, "grid array" of land surface potential electrodes. This array was chosen over a "radial array" to be consistent with a finite difference grid for numerical modeling of the tracer experiment to help with the interpretation of the field data. The modeling results are not presented in this paper. All electrodes were kept in place for the duration of the time-series experiments. The electrode array consisted of a 15 by 15 grid of 224 non-polarizing, disposable, copper sulfate, porous pot electrodes (the type used by Osiensky and Donaldson, 1995) on 1.3 m centers located symmetrically about the injection

well (Figure 2.1). The porous pots were buried 15 centimeters below the ground surface and kept moist for the duration of the tests.

The reference electrode, also a porous pot electrode, was located at the land surface (buried 15 cm) 74.5 m to the west of the injection well. The distant current electrode (i.e., current sink) consisted of a triangle of three stainless steel stakes (spaced 1 m apart and connected by a copper wire) driven 0.3 m into the surface soil 62.4 m to the southwest of the injection well. All electrical connections were weather proofed with silicone rubber caulk and electrical tape to preclude any current leakage or moisture penetration. In addition, all wires were elevated above the ground surface. Both the reference electrode and the distant current electrode were placed as described above instead of at infinity as in a typical MALM application because of land use constraints.

The current source for this experiment was a portable, lead-acid battery, powered GISCO ResiStar RS-100M™ transmitter/receiver system. The transmitter generated rectangular pulses as exciting signals of alternate polarity. A 2-cycle, 1-second period, time-domain signal was transmitted for all MALM measurements because of time constraints during the experiments. Several other signal lengths were evaluated during baseline testing and the 2-cycle, 1-second period was found to give satisfactory results. Electrical potentials were measured one at a time at each of the 224 porous pot electrodes by completing an electrical circuit through the reference electrode to the receiver system that recorded all potential measurements. All electrical potential data were evaluated for integrity and those values with a standard deviation greater than 10 (or 1.0%) were filtered from the data sets prior to analysis.

At time = 0 (initial filling of borehole with tracer solution), the injection well was filled with 34.8 liters of tracer solution from a heated, polyethylene storage tank that contained 795 liters of potassium chloride solution with a constant, electrical conductivity of 0.601 S/m. This formed a 1.91 m long column of conductive tracer solution that extended from the bottom of the borehole to the top of the basalt layer 2.67 m below land surface. The tracer solution level in the injection well was maintained at this depth for the duration of the experiment through a drip system. A total of 342 liters of tracer solution was injected over the first 34 days of the experiment at a nearly constant, average rate of 10.07 liters/d.

2.3. Field data interpretation

Electrical potentials were measured for the 15 by 15 grid of porous pot electrodes six times over the 34-day tracer injection period evaluated herein. The measurement period began 0.83 days after initial tracer injection. Baseline data were collected five days prior to the initial tracer injection. The baseline data were collected under the conditions of an empty injection well with the exception of 10 cm of standing water that accumulated in the bottom of the well after drilling. The water originated from perched water that drained from an overlying fracture zone. This standing water submerged the current electrode. The electrical conductivity of the standing water in the injection well under baseline conditions was 0.1153 S/m.

Ratios of the measured electrical potentials/baseline electrical potentials for the porous pot electrodes were contoured for each measurement period (i) to allow for evaluation of major shape changes in the potential distributions over time. The data are examined by contouring the electrical potentials by the ratio method as follows:

$$V_{rat_{t_i}} = \frac{V_{t_i}}{V_{t_0}}$$

Eqn. 2.3

where: $V_{rat_{t_i}}$ is the ratio of electrical potentials/baseline for time period t_i, V_{t_i} is the electrical potential at time t_i, V_{t_0} is the electrical potential at time $t_0 = 0$ (baseline), i is the measurement period from 1 to 6.

Examination of the data by ratios is preferred over differences (i.e. subsequent data set minus a baseline data set) to evaluate changes between measurement periods because the ratios of voltage (or apparent resistivity) are linearly related to ratio of electrical conductivity, whereas the differences are not. Direct subtraction of the data sets may also compound measurement errors (Slater and Sandberg, 2000). All contour maps of the field data were produced with SURFER© 7 using point kriging to grid the electrical potential data. The data sets are referred to by time in days after the tracer was injected.

Figure 2.2 is a contour map (plan view) of the baseline electrical potentials in millivolts (mV) ($t = t_0 = 0$ days) for the grid of porous pot electrodes. Figure 2.2 shows a

linear conductive anomaly along the northern border of the test site that channels current away from the test site in the east and west directions. The existence of this feature was not known prior to conducting the experiments. Excavation in the anomalous zone after the MALM experiments were completed indicated that a buried, 0.05 m (2 in) diameter galvanized steel pipeline is present at the site at a depth of approximately 1 m. Figure 2.2 also shows conductive anomalies immediately north and south of the injection well. Details of these anomalies are masked by the steep potential gradient near the injection well. However, distortions in the contours from radial symmetry are obvious and the bull's eye is not centered around the injection well due to the presence of the conductive anomalies.

Under ideal conditions, with all else constant (e.g., soil moisture content, soil temperature, depth to ground water, etc.), all temporal changes in the electrical potential distribution from baseline conditions could be attributed to evolution of the tracer plume. Variations in soil temperature and moisture contents between measurement periods were recorded during this experiment (Nimmer et al., 2001b). However, their significance on the measured electrical potentials was not quantified. Application of these relationships is beyond the scope of this paper. However, it is believed that the changes in the electrical potential distribution over time due to the perched water table fluctuations and variations in soil temperature and moisture contents were minor relative to the evolution of the tracer plume during the 34-day tracer injection period evaluated in this paper. Many of the major shape changes in the potential distribution that developed during the first 17 days of the experiment remained to the end of tracer injection period evaluated herein.

Figure 2.3 presents a shaded contour map for $V_{rat0.83d}$ (immediately after filling of the injection well with conductive tracer solution); this figure shows that filling of the injection well with electrolyte changed the current distribution compared to the baseline case and accentuated the *in situ* heterogeneities within the test site. The pipeline anomaly along the northern border of the test site that is definable in the baseline voltage map (Figure 2.2) is also delineated in Figure 2.3. In addition, the contours appear to enclose an evolving tracer plume emanating away from the injection well; however, only about 10 liters of concentrated tracer solution are known to have migrated away from the injection well for $t_1 = 0.83d$.

Finite difference modeling of the tracer experiment confirmed that the borehole-surface

MALM measurements taken during $t_1 = 0.83d$ would be insensitive to such a small volume
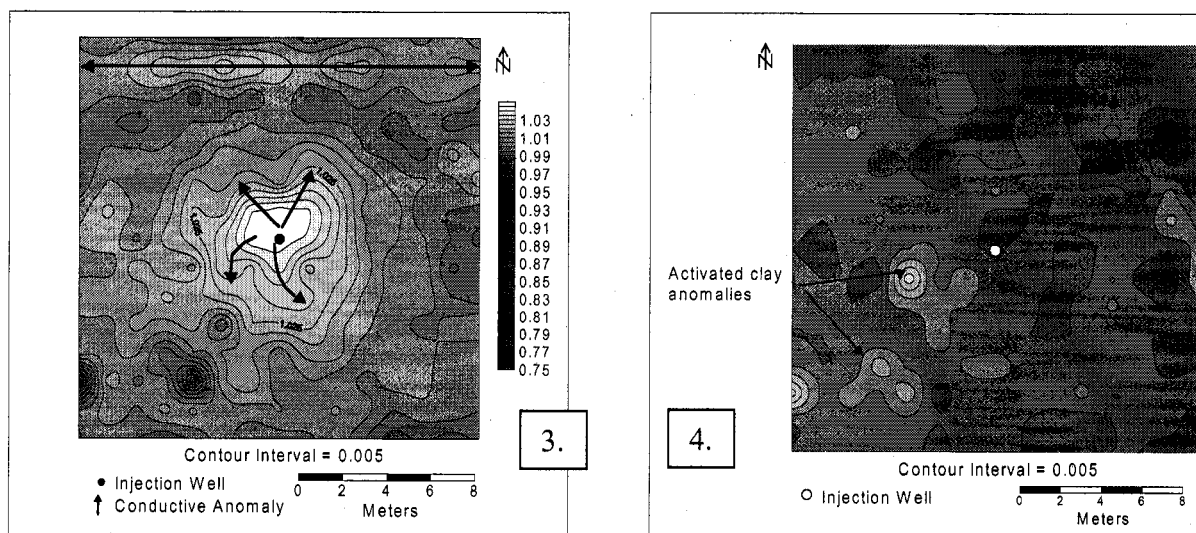
Figure 2.3. Shaded contour map of $V_{rat_{0.83d}}$ values for the grid array of porous pot electrodes. Shading scale is the same for Figures 2.3 through 8.

Figure 2.4. Shaded contour map of $V_{rat_{3d}}$ values for the grid array of porous pot electrodes.

of tracer solution within the 4.57 m thick zone of injection. This "pseudo plume" shaped anomaly shown in Figure 2.3 is believed to be the imaging of clay filled fractures and preferential flow paths (i.e., fracture zones) containing perched water. These anomalies developed because the tracer filled borehole in effect formed a quasi "vertical line source" of current compared to a point source of current for the original baseline data set; therefore, the geometry of the current distribution within and near the injection well was considered to have changed significantly for the scale of this investigation. For this reason $t_1 = 0.83d$ was considered the "new" baseline for analysis of the evolving tracer plume.

Subsequent data sets (2 through 6) also were analyzed by the ratio method. These resulting new data sets were contoured to illustrate the effect that the developing tracer plume had on the electrical potential distribution over time since filling of the injection well. Shaded contour maps of the new data sets are presented in this paper. Most of the changes

that occurred were less than 5%. However, the most dramatic of the changes that developed before $t_5 = 25d$ (prior to when measurable precipitation occurred) were carried through $t_6 = 34d$. Therefore, it is assumed that these major shape changes were real and can be attributed reasonably to the evolution of the conductive tracer plume.

Figures 2.4 through 2.8 present contour maps for V_{rat3d} through V_{rat34d}, respectively. Figures 2.4, 2.5, and 2.6 show anomalies strengthening in magnitude with time to the west (left) of the injection well. These anomalies are believed to be due to selective activation of clay filled fractures by contact with the tracer solution. Resistivity of clay filled fractures should be lower than clean fractures. However, the anomalies appear to be more resistive in the V_{rat} maps (i.e. V_{rat} values >1). It is believed that an increasing percentage of the current was being distributed to the tracer plume over time causing changes in the current density in the anomalous areas. Very little precipitation occurred up to this point in the experiment and soil moisture contents and soil temperatures were relatively stable.
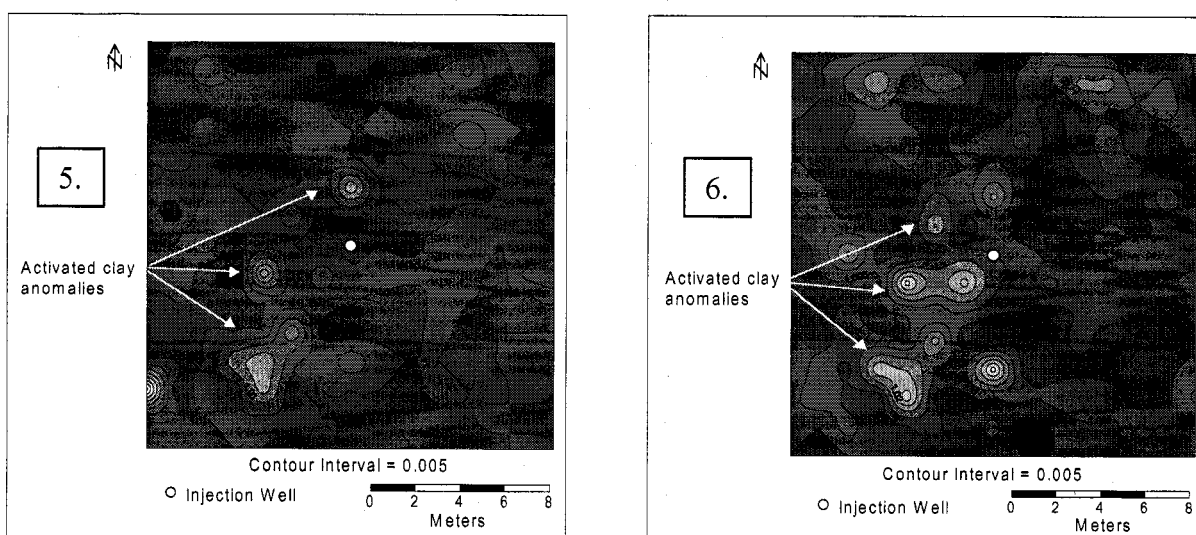
Figure 2.5. Shaded contour map of V_{rat11d} values for the grid array of porous pot electrodes.

Figure 2.6. Shaded contour map of V_{rat17d} values for the grid array of porous pot electrodes.

The evolving tracer plume is shown in Figures 2.7 and 2.8. Comparison of both of these figures with Figures 2.4, 2.5 and 2.6 shows the continued presence of the activated clay anomalies to the west (left) of the injection well. In addition, new, strong anomalies can be seen
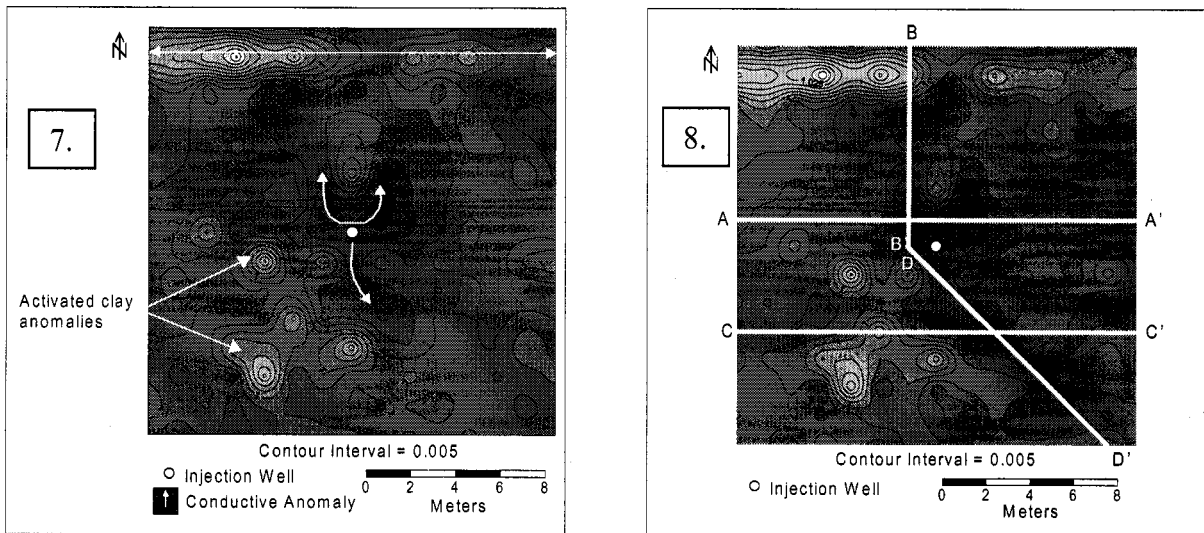
Figure 2.7. Shaded contour map of $V_{rat_{25d}}$ values for the grid array of porous pot electrodes.

Figure 2.8. Shaded contour map of $V_{rat_{34d}}$ values for the grid array of porous pot electrodes. White lines show the locations of the V_{rat} profiles presented in Figures 2.9-12.

emanating from the injection well. The most obvious of these new anomalies is a "bull horns" shaped anomaly just north of the injection well, and a single bull-horn shaped anomaly just south of the injection well. The buried pipeline anomaly along the northern boundary of the test site also reappears. The bull horn anomalies are believed to be segments of the tracer plume migrating through the preferential flow paths delineated in the pseudo-plume anomaly (Figure 2.3). The tracer plume does not appear gradually in Figures 2.4, 2.5 and 2.6 because of masking by the steep potential gradient near the current electrode. In addition, a certain threshold mass of tracer solution is required for detection by the MALM method at the depth of this investigation. Effects of appreciable precipitation, increased soil

moisture contents, and cooling soil temperatures to near freezing are believed to be minor relative to the overwhelming effects caused by the tracer plume.

Figures 2.9 to 2.12 present V_{rat} profiles through four extensions of the evolving tracer plume shown in Figure 2.8. Significant changes (i.e., vertical gaps) between the plotted V_{rat25d} and V_{rat34d} values relative to the V_{rat3d}, V_{rat11d}, and V_{rat17d} values indicate the approximate locations of the tracer plume along the profiles.

2.4. Summary

Borehole-surface MALM measurements were collected over a 34-day period during a radial injection tracer experiment in partially saturated, fractured basalt. Changes in the surface electrical potential distributions during the first 17 days of the tracer test show activated clay anomalies developing to the west of the injection well due to contact with the tracer solution. Anomalies that developed between 17 and 34 days to the north and south of the injection well delineate the size and shape of the evolving tracer plume.

Acknowledgements
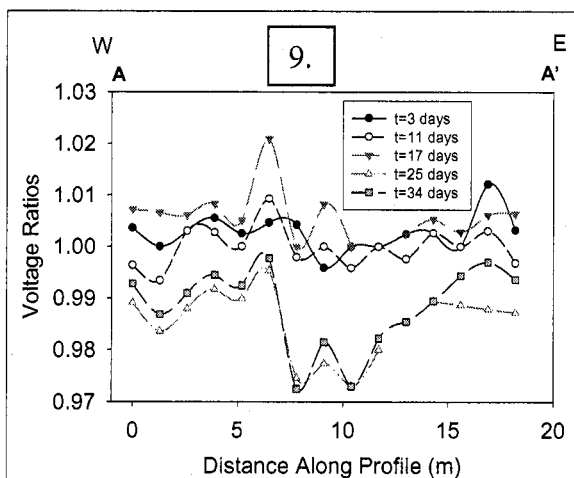
Figure 2.9. Graph of V_{rat} values for the data sets 2 through 6 along the A to A' transect (location shown in Figure 2.8).
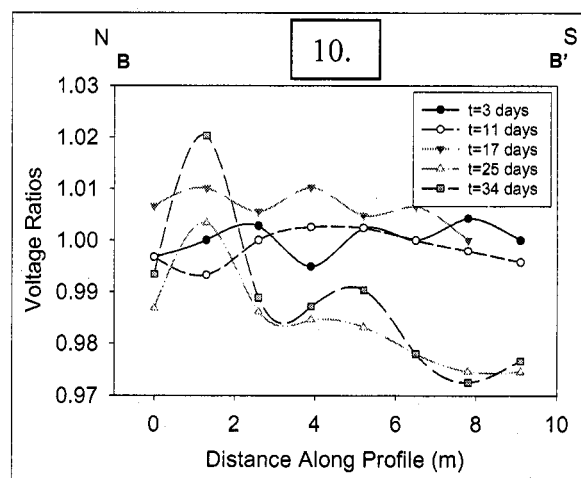
Figure 2.10. Graph of V_{rat} values for the data sets 2 through 6 along the B to B' transect (location shown in Figure 2.8).
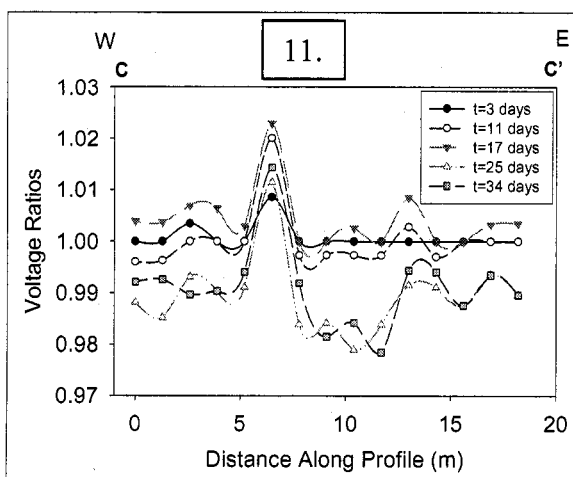
Figure 2.11. Graph of V_{rat} values for the data sets 2 through 6 along the C to C' transect (location shown in Figure 2.8).
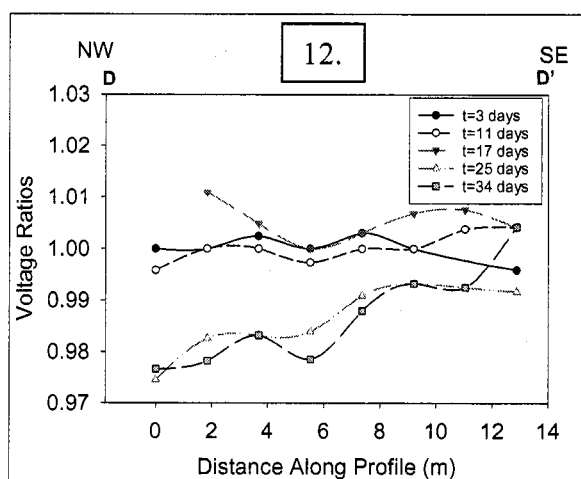
Figure 2.12. Graph of V_{rat} values for the data sets 2 through 6 along the D to D' transect (location shown in Figure 2.8).

References

Archie, G.E., 1942. The electrical resistivity log as an aid in determining some reservoir characteristics. Am. Inst. Min. Metallurg. Pet. Eng. Tech. Paper 1422, 146-154.

Asch, T., and Morrison, H.F., 1989. Mapping and monitoring electrical resistivity with surface and subsurface electrode arrays. Geophysics 54 (2), 235-244.

Bevc, D., and Morrison, H.F., 1989. Borehole-to-surface electrical resistivity monitoring of a salt water injection experiment. Proceedings of the Society of Exploration Geophysicists 59th Annual International Exposition and Meeting, Oct. 29-Nov. 2, Dallas, TX, 216-218.

Bush, J.H., and Seward, W.P., 1992. Geologic field guide to the Columbia River Basalt, Northern Idaho and Southeastern Washington. Idaho Geological Survey Information Circular 49.

Fried, J.J., 1975. Groundwater Pollution, Theory, Methodology, Modelling and Practical Rules. New York: Elsevier.

Golden Software, Inc., 1999. Surfer 7, Contouring and 3D Surface Mapping for Scientists and Engineers, Golden, CO.

Greenhalgh, S.A., and Shunhua, C., 1998. Applied potential modeling of simple orebody structures. In ASEG 13th International Geophysical Conference and Exhibition; Conference Papers, Exploration Geophysics 29, 3-4 (pp. 391-395). Melborne, Austrailia.

Jaemtlid, A., Magnusson, K-A., Olsson, O., and Stenberg, L., 1984. Electrical borehole measurements for the mapping of fracture zones in crystalline rock. Geoexploration 22 (3-4), 203-216.

Keller, G.V., 1987. Rock and mineral properties. Electromagnetic Methods in Applied Geophysics - Theory, Volume 1, Society of Exploration Geophysicists, 13-51.

Keller, G.V., and Frischnecht, F.C., 1966. Electrical methods in geophysical prospecting. International Series of Monographs in Electromagnetic Waves, V. 10, New York: Pergamon.

Ketola, M., 1972. Some points of view concerning mise-à-la-masse measurements. Geoexploration 10, 1-21.

Nimmer, R.E., Osiensky, J.L., and Sprenke, K.F., 2001a. Borehole-surface and cross-borehole mise-à-la-masse delineation of a radial injection tracer experiment in partially saturated fractured basalt. In SAGEEP'01 (BHL-2). Denver, CO.

Nimmer, R.E., Ralston, D.R., Wylie, A. and Johnson G., 2001b. A recirculating tracer test in fractured basalt. In P.K. Link and L.L. Mink (Ed.), Geology, Hydrogeology, and Environmental Remediation, Idaho National Engineering and Environmental Laboratory, Eastern Snake River Plain, Idaho. GSA Special Paper 353. Chapter 17, 263-277.

Osiensky, J.L., 1995. Time series electrical potential field measurements for early detection of groundwater contamination. J. Environ. Sci. Health A30 (7), 1601-1626.

Osiensky, J.L., and Donaldson, P.R., 1995. Electrical flow through an aquifer for contaminant source leak detection and delineation of plume evolution. Journal of Hydrology 169 (2), 243-263.

Osiensky, J.L., 1997. Ground water modeling of mise-à-la-masse delineation of contaminated ground water plumes. Journal of Hydrology 197 (1), 146-165.

Parasnis, D.S., 1967. Three-dimensional electric mise-à-la-masse survey of an irregular lead-zinc-copper deposit in central Sweden. Geophys. Prosp. 15 (3), 407-437.

Parkhomenko, E.I., 1967. Electrical properties of rocks, monographs in geoscience. New York: Plenum Press.

Provant, A.P., 1995. Geology and hydrogeology of the Viola and Moscow West Quadrangles, Latah County, Idaho and Whitman County, Washington. M.S. Thesis, University of Idaho, Moscow, ID.

Schlumberger, C., 1920. Etude sur la prospection electrique du sous-sol. Paris: Gauthier-Villars.

Slater, L.D., and Sandberg, S.K., 2000. Resistivity and induced polarization monitoring of salt transport under natural hydraulic gradients. Geophysics 65 (2), 408-420.

Sjostrom, K.J., and Sill, W.R., 1991. An electrical technique for the determination of ground water flow parameters. In Proceedings of SAGEEP'91 (pp.119-127). Knoxville, TN.

Wang, T., Stodt, J.A., Stierman, D.J., and Murdoch, L.C., 1991. Mapping hydraulic fractures using a borehole-to-surface electrical resistivity method. Geoexploration 28, 349-369.

White, P.A., 1988. Measurement of ground-water parameters using salt-water injection and surface resistivity. Ground Water 26 (2), 179-186.

CHAPTER 3: DIRECT CURRENT AND SELF POTENTIAL MONITORING OF AN EVOLVING PLUME IN PARTIALLY SATURATED FRACTURED ROCK[2]

Robin E. Nimmer and James L. Osiensky

Department of Geological Sciences, University of Idaho, Moscow, ID 83844-3022,USA

Abstract

Hole-surface and hole-hole mise-à-la-masse (MALM) measurements and surface self potential (SP) measurements were taken over a 173-day period during an 8-well, radial injection, tracer experiment in partially saturated, fractured, Columbia River basalt. A potassium chloride tracer stream was injected into the fractured basalt and was energized directly for the MALM experiments. The constant concentration, tracer solution was injected for 76 days above a perched water table at an average rate of 10.07 liters/day. Tracer injection was followed by a 34-day period of tap water injection and a 63-day drainage period. The associated changes in potential distributions and SP's over time indicate that an asymmetrical, vadose zone plume evolved in the fractured basalt. Hole-surface and SP measurements were used to track the lateral evolution of the tracer plume; however, there was some noise and variability in the SP data. The hole-hole measurements helped delineate the depth of preferential tracer migration in the fractured basalt.

Key words: mise-à-la-masse, self potential, fractured rock, preferential flow paths, vadose zone, tracer test

---

3.1. Introduction

Cost effective delineation of zones of contamination in partially saturated and saturated fractured media is critical to the success of remediation efforts for many subsurface contamination problems. Basic hydrogeologic methods for detecting ground water contamination often are inefficient, particularly in fractured rock. Hydrogeologic methods to delineate contaminant migration pathways generally are invasive and often involve extensive drilling programs. Delineation within the vadose zone is extraordinarily difficult using conventional detection methods of drill and sample because of heterogeneity and the existence of unidentified, preferential pathways for contaminant migration. However, surface electrical geophysical methods provide cost effective and minimally invasive tools to help delineate contaminated zones and preferential flow paths that contain a continuous liquid phase with contrasting electrical properties.

One minimally invasive, electrical method that is relatively fast and efficient was first suggested by Schlumberger (1920). According to Parasnis (1967), the method later became known as the mise-à-la-masse (MALM) method which can be interpreted as "excitation of the mass". MALM also is known as the charged body potential method. MALM is a variation of galvanic resistivity methods and was developed originally to map electrically conductive earth materials by passing a current directly into the zone of interest while electrical potentials are measured at the land surface or in boreholes (Parasnis, 1967). Self potentials (SP) commonly are considered to be noise that is to be separated from resistivity measurements such as MALM. However, when non-polarizing potential electrodes (e.g., copper sulfate or silver chloride) are used, measurement of SP generally is standard practice and may provide useful information for environmental applications. However, SP varies over time because of natural (telluric) currents in the ground caused by ionospheric currents (Sharma, 1986). Measurement of MALM potentials and SP at the land surface is relatively easy and can be accomplished with a simple, hand-held, high impedance voltmeter or with an electrical resistivity receiver.

Several investigators have researched various surface and hole-to-surface electrical methods to evaluate the migration characteristics of conductive tracers below the water table.

Fried (1975) described the use of electrical resistivity measurements to evaluate the velocity and direction of migration of a sodium chloride tracer from a single well. White (1988, 1994) described use of the method of Fried (1975) in New Zealand. Sjostrom and Sill (1991), and Bevc and Morrison (1989, 1991) used hole-to-surface electrical methods to track the movement of saline tracers in ground water. Dey and Morrison (1979), and Wilt and Tsang (1985) showed that downhole current electrodes placed in an electrolytic contaminant zone produce significantly stronger anomalies than surface arrays. Osiensky (1995), and Osiensky and Donaldson (1995) described a modified MALM experiment to delineate a tracer plume in fluvial sediments. Osiensky (1997) described the use of the MALM method to define plume length and the location of the center of mass of hypothetical contaminant plumes. Nimmer et al. (2001) described hole-surface and hole-hole MALM measurements during the first 34 days of the experiment described herein.

Many investigators have used or have simulated various surface, hole-surface, and hole-hole resistivity methods, and SP methods to evaluate environmental, geothermal and mining related applications. Only a selected few are mentioned here. Beasley and Ward (1986) simulated hole-hole and hole-surface MALM responses to a hypothetical fracture zone in a geothermal system. Brown (1989) compared hydraulic and electrical conductivities of a single fracture and showed that current flow and water flow followed similar pathways through the fracture. Wang et al. (1991) used hole-surface MALM in an attempt to detect new fractures formed by hydraulic fracturing in an injection well. Street et al. (1993) used MALM to detect seepage from a leaking PVC lined tailings pond. Sato and Mooney (1960) suggested that SP anomalies associated with conducting ore bodies were due to the electrochemical effects of concentration gradients of minor ground water constituents such as Fe^{2+} and Fe^{3+}. Nourbehecht (1963) simulated diffusion potentials due to vertical concentration gradients. Abaza and Clyde (1969) measured streaming potentials caused by the migration of NaCl and KCl solutions of various concentrations through Ottawa sands. Sill (1982) simulated the electrochemical effects due to diffusion of brines associated with a geothermal system and concluded that the resulting SP anomalies would be small. Thanassoulas (1989) and Thanassoulas and Lazou (1993) used SP to map deep fracture zones in geothermal systems. Birch (1993, 1998) used surface SP measurements to detect the

position of water tables. Stierman (1984) used MALM, and attempted to use surface SP measurements, to detect contaminated ground water near a waste disposal site.

3.2. Basic considerations

The MALM method allows for the direct measurement of the electrical potential distribution about a single, point source of electric current. The SP method involves the measurement of spontaneous ground potentials from various unidentified sources. Background SP's may be created by fluid streaming, bioelectric activity in vegetation, varying electrolytic concentrations in ground water, telluric currents and other geochemical actions (Telford, et al. 1990). The resulting MALM electrical potential distribution and SP's for an area of investigation incorporate all factors that contribute to their development at the particular time of measurement. However, where data can be collected in time-series, temporal changes that occur can be evaluated.

In saturated and unsaturated porous media, the electrical properties are dominated by the porosity fraction, and the conductivity of the fluids that exist in the pore spaces (Keller and Frischknecht, 1966; Archie, 1942). A conductive contaminant plume (e.g. inorganic contaminants) with liquid phase continuity throughout will provide conductive pathways for the flow of current that correspond approximately to the hydraulic pathways through which the plume evolved.

The electrical conductivity of porous media (σ_m) is given by the Archie (1942) formula as (Keller, 1987):

$$\sigma_m = a\sigma_w S^n \phi^m \qquad \text{Eqn. 3.1}$$

where: ϕ is the porosity, S is the fraction of pores containing water (i.e., S=1 for complete saturation), σ_w is the electrical conductivity of the pore water, n is an empirical exponent based on the texture of the rock. Values range between 1.3 in loosely packed granular media to about 2.2 in well-cemented granular rocks (Parkhomenko, 1967), and a and m are empirical constants used to force the formula to fit the behavior of the rock type of interest.

According to Keller (1987), for a given porosity and water saturation, fracture porosity typically will exhibit the highest rock conductivity due to the simpler shape of the pores while vuggy porosity will result in the lowest conductivity because of the complex pores. For this study, the conductive body of interest was a relatively conductive, electrolyte tracer plume emanating from a vertical borehole filled with a conductive tracer solution. The borehole was located in the vadose zone and penetrated into the top of a perched water table. An irregularly shaped, fracture dominated, vadose zone plume developed over time as the conductive tracer solution migrated away from the borehole through primarily subhorizontal fractures in the upper portion of a single basalt flow. Changes in the MALM electrical potentials, and SP's over time were evaluated to delineate the evolution of the tracer plume.

3.3. Field demonstration

3.3.1 Site geology

The field site is located at the University of Idaho Ground Water Research Site in Moscow, Idaho (Figure 3.1). The field demonstration was conducted in the weathered, vesicular flow top of the uppermost flow of the Wanapum Formation (14.5 million years old). Several fracture zones were detected in borehole video logs for test wells at the site. The fresh basalt contains open fractures while the weathered zones contain fractures partially filled with halloysite clay derived from oxidative weathering of the basalt (Hosterman et al., 1960). Clay also fills many vesicles. According to Keller and Frischknecht (1966), 95% of resistivity measurements in Columbia River basalts fall within the range between 132 and 500 ohm-m, with an average of 257 ohm-m.

Basalt at the test site is overlain by approximately 3 m of Palouse loess (Pleistocene) and recent alluvium (Provant, 1995). The loess is composed of a silty loam with mostly quartz and feldspar in addition to small percentages of sand and clay. Alluvial sediments consist of reworked loess with basalt and granitic fragments.

3.3.2. Tracer test

A long-term, radial injection tracer test was conducted from November 6, 1999 and to April 27, 2000. Saline water was injected into partially saturated, fractured basalt during the first 76 days (d) of the test, followed by 34 d of tap water injection and a 63 d drainage phase.

Eight wells with a diameter of 15.2 cm were drilled by air-rotary specifically for these experiments. The injection well was centrally located within the group of seven observation wells (Figure 3.1). Figure 3.2 shows the well logs for the eight wells. The wells ranged in depth
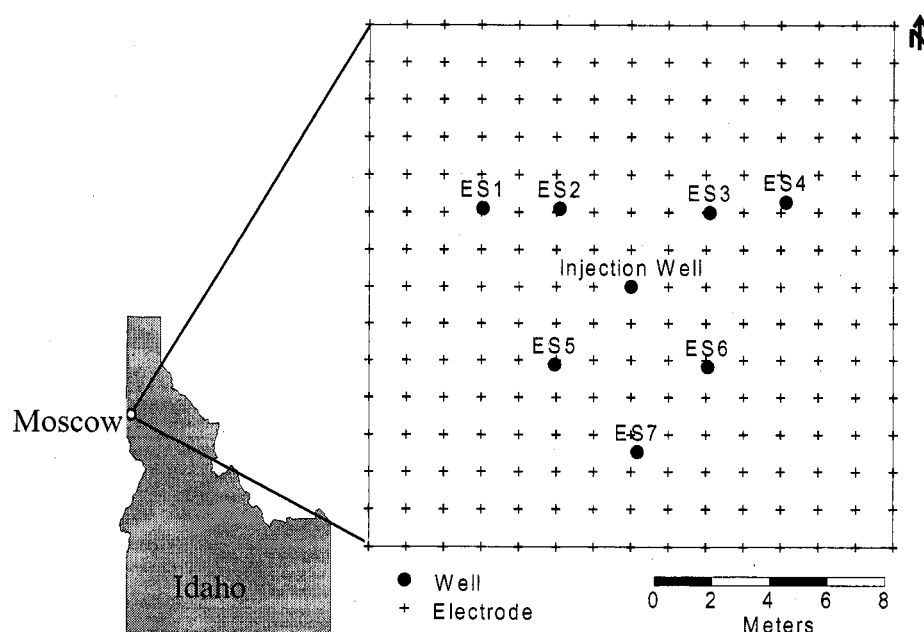
Figure 3.1. Site location map of the wells and porous pot electrodes for the tracer experiment.

from 4.6 m (injection well) to 7.5 m (well ES7) relative to the gently sloping land surface. The topography slopes approximately 11% toward the north over the entire site area. The observation wells penetrated the top of a perched water table such that standing water was present in the bottoms of all of the wells after drilling. The wells were cased with 15.2-cm diameter, schedule 80 PVC pipe through the sediments and left open through the basalt. An inner PVC liner (schedule 40) with a diameter of 5.1 cm was placed in each observation well;

hacksaw slots were made in the bottom 10 cm to allow water to enter the pipe for sampling. Electrodes were attached to the outside of each PVC liner.
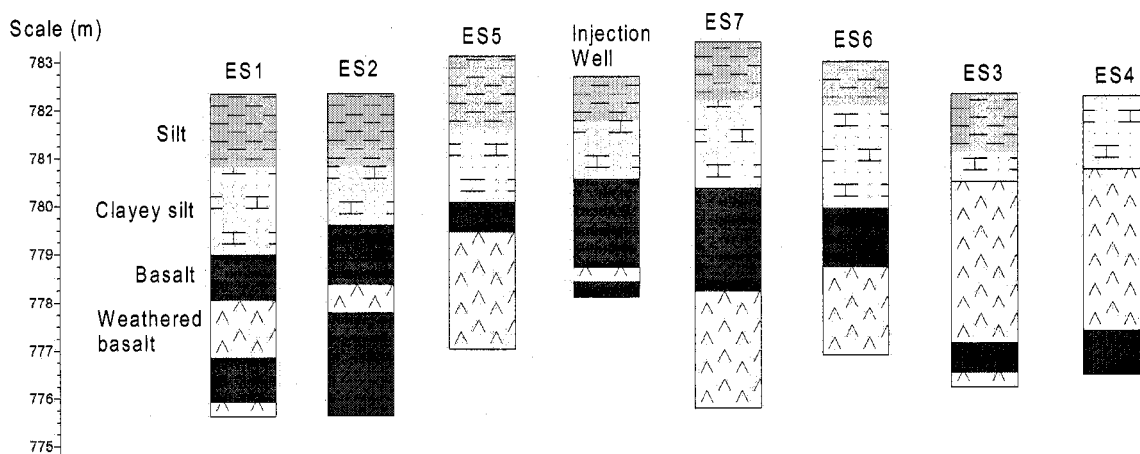
Figure 3.2. Well logs for observation wells and the injection well.

A total of 89 downhole electrodes were installed but only 66 electrodes were used in this hole-hole MALM experiment due to a limited number of circuit switches. Downhole electrodes were constructed of insulated, 14 gauge, copper, Type UF underground feeder cable. A 25 cm-length of insulation was stripped from the end of each wire, and the bare wires were wrapped around the PVC liners to approximate point electrodes. Electrodes were placed 10 cm from the bottom of each liner and at 30 cm intervals to the top of basalt (Figure 3.3). A liner was placed in the bottom of each well and centered. Each borehole annulus was filled with a 10 cm thick sand pack followed by dampened silt to the land surface. The dampened silt provided electrical connection between the electrodes and the borehole walls. The injection well was not backfilled but did contain a 1.3 cm diameter, PVC pipe that was fitted with electrodes. Well ES1 contained the most electrodes (ten). The current electrode for both MALM experiments was placed 10 cm above the bottom of the injection well, and five potential electrodes were placed above the current electrode on 30 cm intervals.

A 15 by 15 grid array of 224 non-polarizing, porous pot electrodes on 1.3 m-spacings were installed symmetrically around the injection well for the hole-surface MALM and SP measurements (Figure 3.1). These electrodes were tested for integrity prior to the start of the tracer injection. The reference electrode also consisted of a porous pot, and the distant
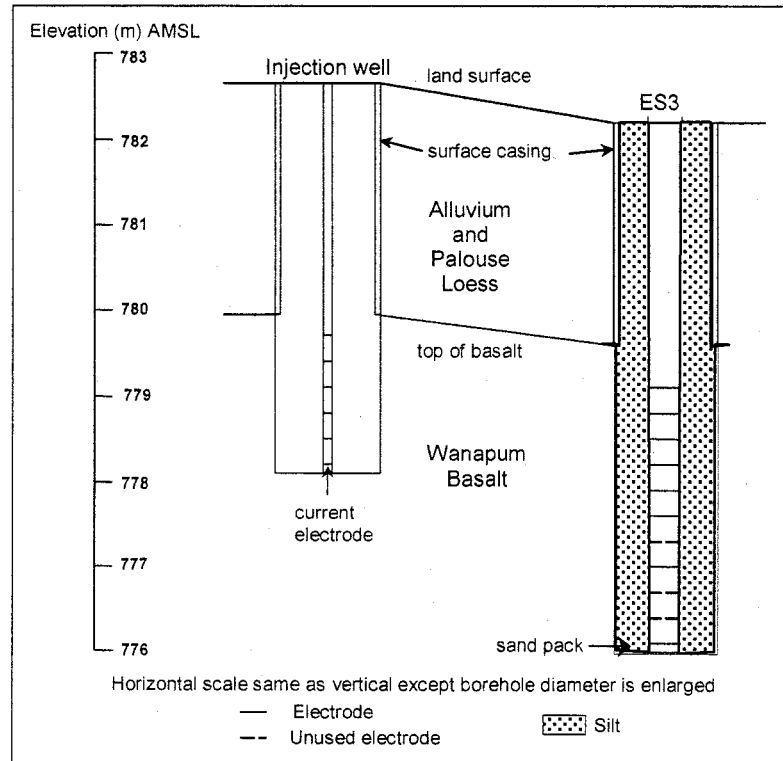
Figure 3.3. Cross section between the injection well and one of the observation wells, ES3, showing representative well and electrode completion details.

current electrode consisted of three stainless steel stakes connected by a copper wire. These electrodes were placed 74.5 m to the west and 62.4 m to the southwest of the injection well, respectively, due to land use constraints.

A portable, ResiStar RS-100M™ by GISCO was used as the transmitter/receiver system. The unit contained a 12-volt, lead-acid battery for the current source. A 2-cycle, 1-second time domain signal was transmitted. Other signal lengths were tried but the 2-cycle, 1-second period was found to give satisfactory results. The current was controlled by the transmitter/receiver and varied approximately ± 5 mA, by design, during each measurement period; the potentials were back-calculated from recorded resistivity values external to the transmitter/receiver based on an average current of 230 mA. The transmitter generated rectangular pulses as exciting signals of alternate polarity during MALM. SP and MALM measurements were taken manually at each of the 224 porous pot electrodes by completing an electrical circuit through the reference electrode to the receiver system that recorded all

measurements. Potential electrodes for the hole-hole MALM were wired directly to a GISCO Multi-Electrode Cable System ME-100™ and measured automatically by program request.

The tracer experiment was designed with three distinct phases. Phase 1 began with the addition of the electrolyte tracer. At t=0 d, the injection well was filled to the top of the basalt layer with 34.8 liters (L) of saline water, with a constant electrical conductivity of 0.601 S/m. This formed a 1.91 m-long column of conductive tracer solution that extended from the bottom of the borehole to the top of the basalt layer 2.67 m below land surface. A constant head was maintained at the top of the basalt layer in the injection well through a drip system from a heated, polyethylene, storage tank that contained a mixture of tap water and potassium chloride (KCl). A nearly constant injection rate of 10.07 L/d was maintained throughout the experiment. A total of 765 L of saline water was injected during Phase 1 (76 d). Phase 2 began immediately after tracer injection ended. Beginning on day 77, the saline water was evacuated from the injection well and the injection stream was changed to tap water with an electrical conductivity of 0.0294 S/m. Phase 2 of the experiment continued for a 34 d period during which 342 L of tap water were injected. Phase 3 consisted of a drainage period (no water injected) from day 111 to day 173 of the experiment.

3.4. Data interpretation

3.4.1. Introduction

Data sets were collected 19 times for both the hole-surface MALM and the hole-hole MALM and 11 times for SP throughout the 173-day experiment. During Phase 1, ten hole-surface MALM, nine hole-hole MALM, and nine SP data sets were collected. Four hole-surface MALM and five hole-hole MALM data sets were acquired during Phase 2. No SP measurements were taken during Phase 2. Five hole-surface MALM, five hole-hole MALM and two SP data sets were collected during Phase 3. The data were filtered using threshold standard deviations of S>10 (1.0%) for MALM and S>15 (1.5%) for SP. In this study, the standard deviation is the percentage difference between two consecutive resistivity readings used by the transmitter/receiver system to compute the average (recorded) resistivity for each

electrode. No porous pot electrodes needed to be replaced during the experiment. All SP data were collected prior to collection of the MALM data when both measurements were taken on the same day.

Baseline data for MALM were collected 5 days prior to the tracer injection. SP baseline data were collected one day prior to the tracer injection. Baseline data were collected with 10 cm of standing water in the injection well that drained from an overlying fracture zone. Electrical conductivity of the standing water in the injection well was 0.1153 S/m.

Tracer injection began at time t=0 d. The first post-baseline data set for SP was completed at t=0.069 d (100 minutes); data collection for hole-surface MALM, and hole-hole MALM was completed at t = 0.83 d. Changes from baseline incorporate an immediate, major change in the current distribution near the injection well from a point source of current before the tracer test to a quasi-cylindrical source of current after filling of the injection well due to the conductive water column. Because of this, the first SP and MALM data sets collected after tracer injection began are considered "new baselines" from which the evolution of the tracer plume is evaluated for all three phases of the experiment.

3.4.2. Data analyses

3.4.2.1. Hole-surface MALM

All contour maps were produced with SURFER© 7. Figure 3.4 is a contour map showing changes in the potential distribution caused by addition of electrolyte tracer to the injection well; the contour map presents ratios of potentials ($V_{rat_{0.83d}}$) based on (Daily and Ramirez, 1995):

$$V_{rat_{0.83d}} = \frac{V_{0.83d}}{V_{0d}}$$

Eqn. 3.2

where: $V_{0.83d}$ are the potential measurements for t = 0.83 d and V_{0d} are the potential measurements for the baseline data set (t = 0 d).

An amoeboid shaped anomaly emanating from the injection well to the north and south is delineated. This anomaly is believed to reflect direct current flow into a fracture

zone that drained perched ground water at a depth of 3.5 m below land surface during drilling of the injection well. The amoeboid shaped anomaly referred to as the "pseudo-plume" anomaly is partly an artifact of radial bias imposed by the geometry of the MALM experiment (i.e., single current electrode). A distinct east-west trending anomaly is detected in the northern portion of the site. A 5 cm diameter, galvanized steel pipe was excavated 0.76 m below land surface in this area (beneath row 2 of electrodes) following the completion of the experiments. The existence of this pipe was not known before the experiment began; however, the anomaly caused by the pipe did provide useful control points for the data interpretations. Very complex changes in the current distribution were created by filling of the injection well with electrolyte tracer. Therefore, potentials for $V_{0.83d}$ are considered to be the "new baseline" from which changes in the potential distribution due to tracer migration over time are evaluated.
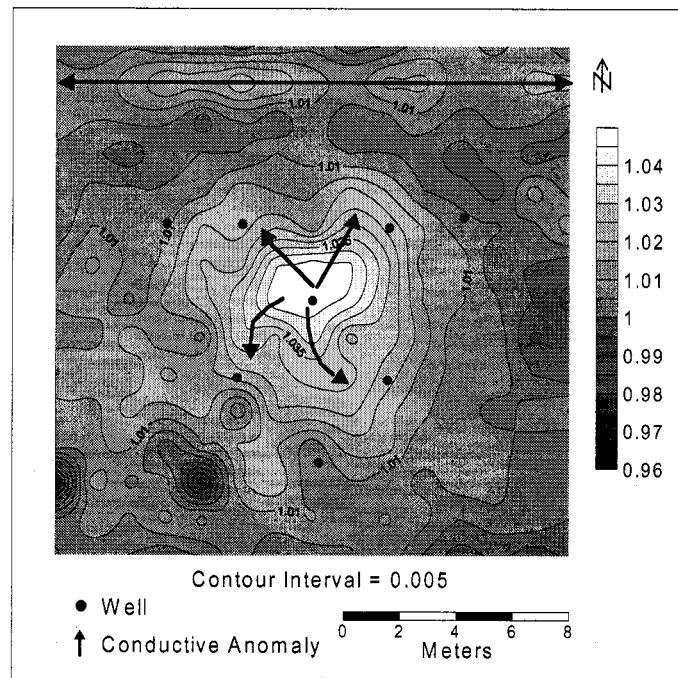
Figure 3.4. Shaded contour map of $V_{rat_{0.83d}}$ values for the grid array of porous pot electrodes for the hole-surface MALM data.

Changes subsequent to the new baseline (i.e., after 0.83 d) are shown in Figure 3.5. The contour maps present ratios of potentials ($V_{rat_{t_i}}$) according to:

$$V_{rat_{t_i}} = \frac{V_{t_i}}{V_{0.83d}}$$
Eqn. 3.3

where: t_i is the elapsed time in days since initial filling of the injection well and V_{t_i} are the potential measurements.

The current electrode was approximately a point source of current in the baseline case but once the injection well was filled with electrolyte, the current electrode became a 1.91 m long cylindrical column of conductive liquid. Changes from the new baseline were evaluated to delineate the evolution of the tracer plume. The following selected data sets are presented in Figures 3.5: $V_{rat_{3d}}$, $V_{rat_{25d}}$, $V_{rat_{82d}}$ and $V_{rat_{173d}}$. $V_{rat_{t_i}}$ values equal to 1 indicate no change since 0.83 d. $V_{rat_{t_i}}$ values < 1 indicate a reduction in potentials since 0.83 d. $V_{rat_{t_i}}$ values > 1 indicate an increase in potentials since 0.83 d. The shaded scales of the contour maps are inconsistent for visual enhancement; however, the contour interval is consistent. The actual magnitude of the values does not necessarily define increases or decreases in resistivity spatially between different time periods. However, consistent shape changes in the contours between different time periods are indicative of the approximate locations of changes in resistivity.

The electrolyte tracer migrated away from the injection well through a complex system of fractures in the basalt. Over time, bull's eye anomalies increased in magnitude and in number southwest of the injection well. Comparison of the contour maps for $V_{rat_{3d}}$ and $V_{rat_{25d}}$ (Figures 3.5a and 3.5b) illustrates these anomalies that are believed to reflect fractures that contain clay. Results of 3-D, finite difference, forward modeling (not presented in this paper) showed that electrolyte contact with clay-filled fractures causes preferential current channeling and selective activation of the clay-filled fractures during MALM. It is interesting to note that these anomalies appear relatively more resistive than baseline conditions. However, as the tracer plume evolved through preferential pathways, more and more of the current was channeled into those pathways causing other areas to appear relatively more resistive. It is important to note that current channeling through finite conductive bodies, such as clay filled cavities, routinely causes elevated potentials in the

regions of ingress and regress. Thus, increased potentials are expected in areas external to the migrating plume.

Anomalies in the $V_{rat_{25d}}$ contour map (Figure 3.5b) have two main similarities to the anomalies shown in the contour map for $V_{rat_{0.83d}}$ (Figure 3.4). The first noticeable feature is the apparent reappearance of the pseudo-plume anomaly near the injection well. A second

a) t=3 d   b) t=25 d   c) t=82 d   d) t=173 d
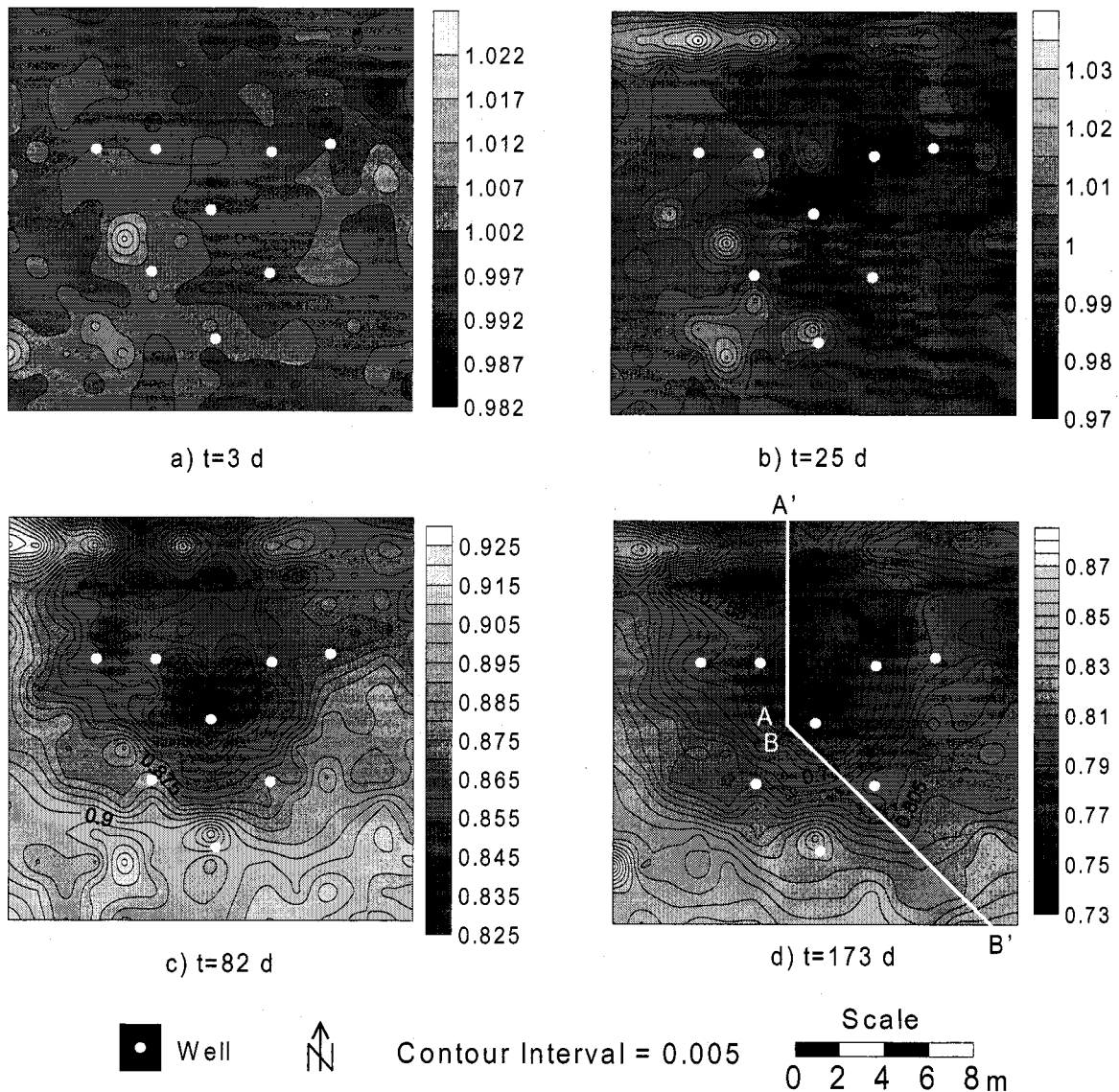
Figure 3.5. Shaded contour map of a) $V_{rat_{3d}}$, b) $V_{rat_{25d}}$, c) $V_{rat_{82d}}$ and d) $V_{rat_{174d}}$ values for the grid array of porous pot electrodes for the hole-surface MALM data.

feature to reappear is the pipeline anomaly. These reappearances are very interesting. The pseudo-plume anomaly in Figure 3.4 developed when electrolyte first filled the injection well and created electrical continuity between the column of electrolyte solution and the fracture pathway(s) that contained perched ground water. Reappearance of the anomaly after 25 d of tracer migration indicates that the tracer followed the same pathways delineated in Figure 3.4. However, the threshold conductivity contrast needed for detection by MALM did not develop until day 25 of the experiment. Similarly, the pipeline anomaly reappeared due to a change in the current distribution caused by the evolution of the tracer plume and the concomitant increase in current channeling into the fracture zone. It is interesting to note that the pipeline anomaly exhibits elevated potentials with respect to its surroundings due to increased current channeling into the plume and away from the pipeline.

Contour maps for $V_{rat_{82d}}$ and $V_{rat_{173d}}$ (Figures 3.5c and 3.5d) show that the plume continued to grow northward and spread laterally to the end of the experiment. These figures suggest that hole-surface MALM was not very sensitive to Phase 2 (injection of tap water into the plume) and Phase 3 (drainage) of the experiment. Slight changes in resistivity were measured; however, no definable zone of increased resistivity developed around the injection well during tap water injection. Hydrodynamic dispersion is believed to have mixed the injected tap water with the tracer solution in the basalt reducing the resistivity contrast.

Electrical conductivity (EC) of the water in the observation wells was measured during the experiment. EC of the water in wells ES2, ES3, ES6 and ES7 increased from baseline over time and peaked in mid-January (i.e. approximately t=70 d) as follows: ES2 increased 14% (from 1227 to 1404 μS/cm), ES3 increased 124% (from 970 to 2170 μS/cm), ES6 increased 52% (from 1221 to 1854 μS/cm), and ES7 increased 44% (from 1477 to 2130 μS/cm). The contour maps in Figure 3.5 show that the plume migrated in the direction of these four wells. No significant increases in EC of the water in wells ES1, ES4, and ES5 were measured during the experiment.

Potential profiles were developed through areas of the plume anomaly delineated in the contour maps. These plots show actual $V_{rat_{ti}}$ values (i.e., unaffected by smoothing generated by the kriging algorithm). Locations of the profile lines are shown on Figure 3.5.

Figure 3.6 shows the south-north profile along A-A'. Figure 3.7 shows the northwest-southeast
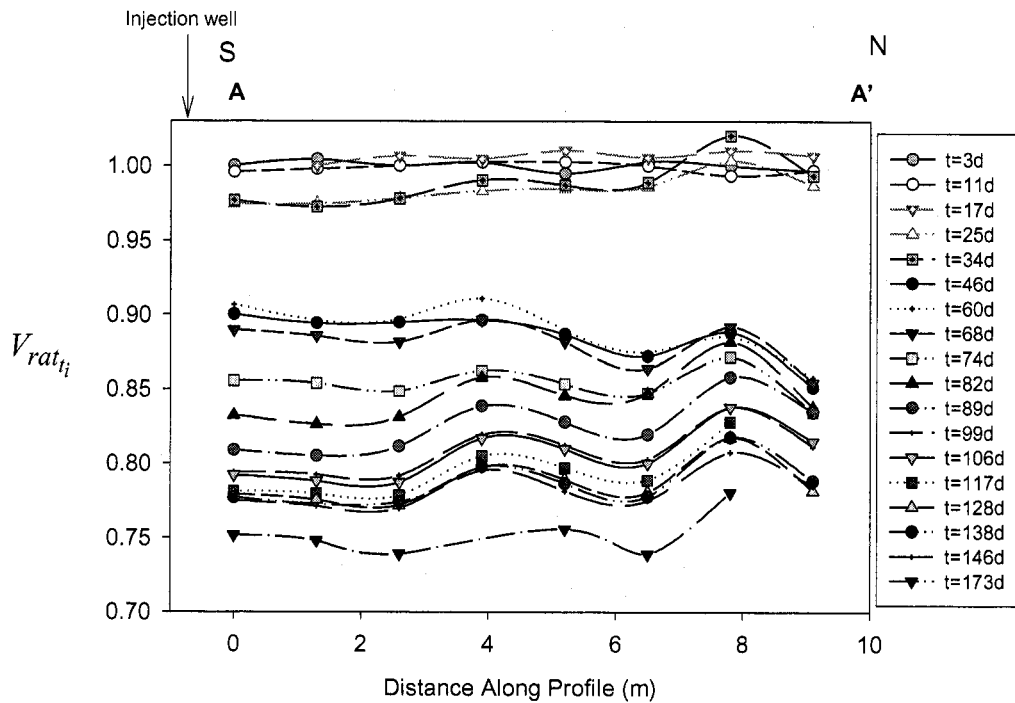
Figure 3.6. Plot of $V_{rat_{t_i}}$ values along south-north profile line A-A' for hole-surface MALM (location of profile line shown on Figure 3.5).

diagonal profile along B-B'. Because the electrolyte tracer plume caused a decrease in resistivity, the $V_{rat_{t_i}}$ values were expected to decrease continuously over time as the plume evolved. The plots beginning with $V_{rat_{25d}}$ and $V_{rat_{34d}}$ show the smallest $V_{rat_{t_i}}$ values near the injection well area as expected. The large drop in $V_{rat_{t_i}}$ values between $V_{rat_{34d}}$ and $V_{rat_{46d}}$ is believed to have been caused by migration of tracer to the true water table or possibly by current leakage through the rain wetted wires. Along the A-A' profile (Figure 3.6), the smallest $V_{rat_{t_i}}$ values were measured in the northern area of the site for $V_{rat_{46d}}$ through $V_{rat_{74d}}$. It is unknown why this temporary phenomenon occurred because injection of electrolyte tracer was ongoing. After t=74 d, the smallest $V_{rat_{t_i}}$ values again were measured in the southern area of the profile near the injection well and $V_{rat_{t_i}}$ values decreased continually in

most areas of the test site as the tracer plume evolved. Along the profile B-B' (Figure 3.7), the potential gradient continued to increase as concentrations in the plume increased.
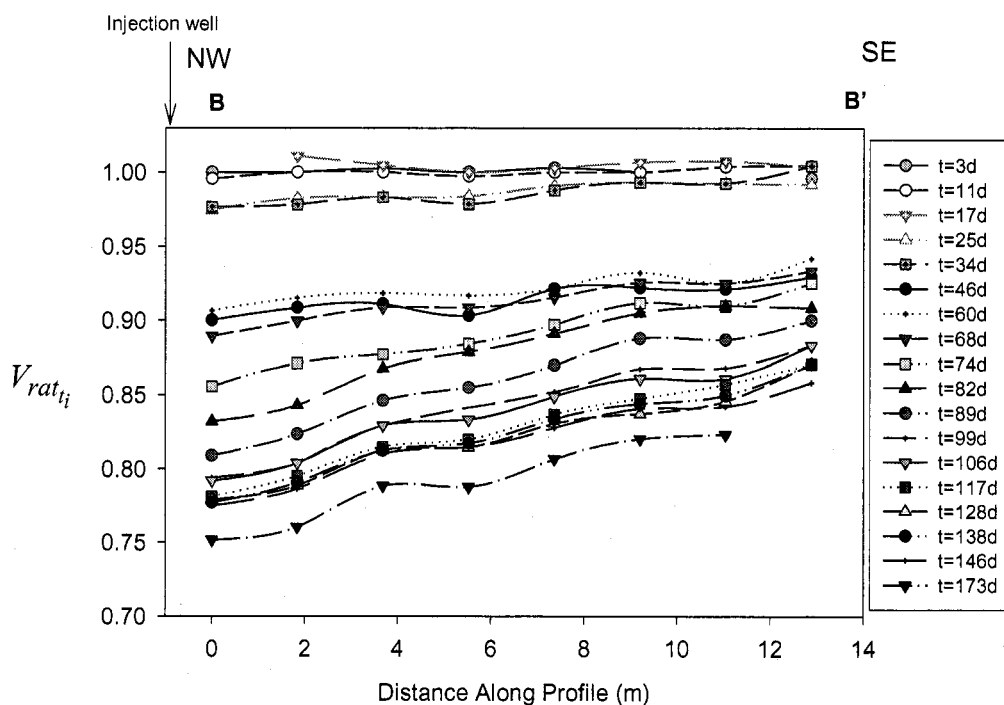
Figure 3.7. Plot of $V_{rat_{t_i}}$ values along northwest-southeast diagonal profile line B-B' for hole-surface MALM (location of profile line shown on Figure 3.5).

3.4.2.2. Self potentials

When the SP method is used in environmental problems compared to mineral exploration it is more sensitive to extraneous effects including varying soil conditions, ground saturation levels, changes in topography, lateral resistivity variations and by effects of variations in telluric currents (Sharma, 1997). The SP data presented in this paper were affected by significant noise; however, certain major changes that developed over the course of the tracer injection experiment can be attributed reasonably to evolution of the electrolyte tracer plume. SP measurements collected on November 5, 1999 were considered to represent baseline conditions for t=0 d. Figure 3.8 presents a contour map of differences in SP ($SP_{diff_{0.069d}}$) that developed between t=0 d (filling of the injection well) and t=0.069 d (100 min) according to:

$$SP_{diff_{0.069d}} = SP_{0.069d} - SP_{0d} \qquad\qquad \text{Eqn. 3.4}$$

where: $SP_{0.069d}$ are the measured SP's for t = 0.069 d and SP_{0d} are the baseline SP values.

The $SP_{diff_{0.069d}}$ values varied from approximately +290 to –200 mV over the grid of porous pot electrodes. No precipitation occurred during this period and fluctuations in air and soil temperatures were minor. Anomalies on the contour map are attributed to filling of the injection well with electrolyte. $SP_{diff_{0.069d}}$ values = 0 indicate no change occurred from baseline conditions. $SP_{diff_{0.069d}}$ values > 0 indicate SP was greater in the subsequent data set, and $SP_{diff_{0.69d}}$ values < 0 indicate SP was less in the subsequent data set. Although anomalies are delineated in Figures 3.8 it is unclear what they represent. The anomalies are not similar to the anomalies produced by hole-surface MALM because a direct current is not applied. In addition, SP is not believed to impose a radial bias on the data like MALM (Figure 3.4) at the scale of this investigation because of the very slow rate of tracer migration during the experiment.

The first post-baseline SP data set ($SP_{0.069d}$) was considered to represent "new baseline" conditions, from which subsequent SP changes since filling of the injection well with electrolyte were evaluated in plan view and in profile. These $SP_{diff_{t_i}}$ values were derived according to:

$$SP_{diff_{t_i}} = SP_{t_i} - SP_{0.069d} \qquad\qquad \text{Eqn. 3.5}$$

where: t_i is the elapsed time in days since initial filling of the injection well, and SP_{t_i} are the SP measurements.
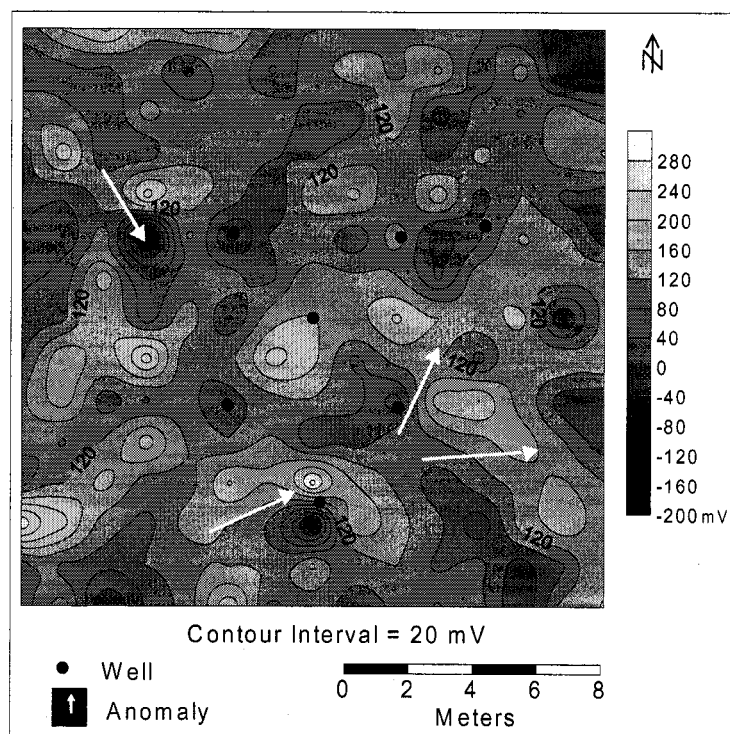
Figure 3.8. Shaded contour map of $SP_{diff_{0.069d}}$ for the grid of porous pot electrodes.

Figure 3.9 presents contour maps for (a) $SP_{diff_{3d}}$, (b) $SP_{diff_{17d}}$ and (c) $SP_{diff_{150d}}$. $SP_{diff_{t_i}}$ values ranged from approximately +120 to –950 mV over the course of the injection experiment. The shaded scales of the contour maps are inconsistent for visual enhancement; however, the contour interval is consistent. The most obvious anomalies that first appeared in Figure 3.9a and increased in strength over time were 1) a bull's eye near well ES1 with positive values embedded in an area with negative values, 2) two bull's eyes near well ES7, one with positive or small negative values and the other with larger negative values, and 3) an arcuate shaped, strongly negative anomaly to the east of wells ES4 and ES6. A fourth anomaly developed after t=3 d extending from the injection well to the northeast between wells ES2 and ES3 (Figure 3.9b). This feature increased in size and strength over time and merged with anomalies one and three. The first three anomalies were detected in the $SP_{diff_{0.69d}}$ contour map and developed too soon after the tracer was injected to be indicative of actual locations of electrolyte tracer. The bull's eyes in the first and second anomalies may have been caused by "weak" electrodes (i.e., possibly loss of copper sulfate from certain porous

pots). The third anomaly may reflect heterogeneities in the basalt in the form of weathered zones in contact with the electrolyte tracer. The fourth anomaly is the only persistent anomaly that developed over time and may be the result of the tracer plume migrating toward the north as indicated by the hole-surface MALM data.
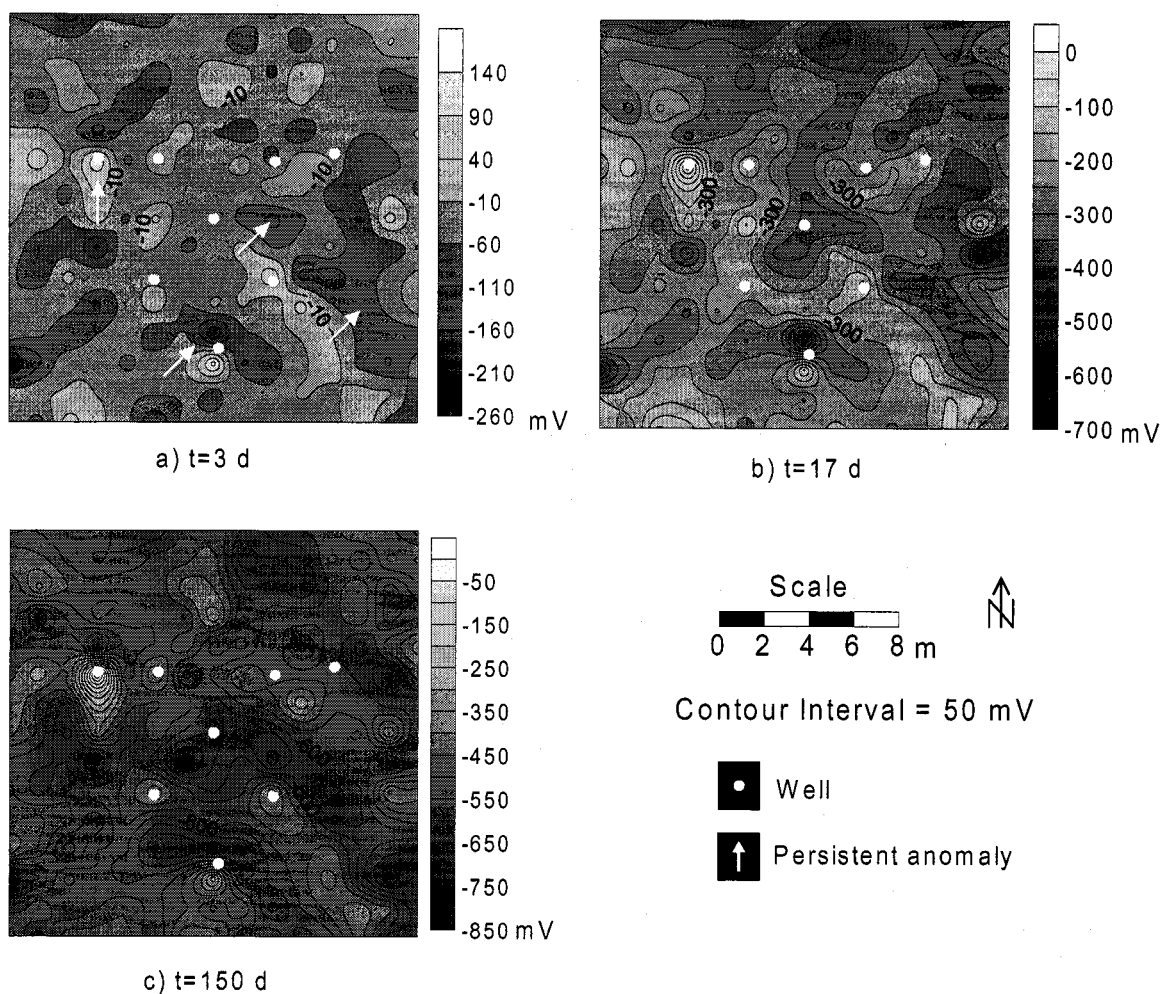
Figure 3.9. Shaded contour maps for a) $SP_{diff_{3d}}$, b) $SP_{diff_{17d}}$ and c) $SP_{diff_{150d}}$ for the grid array of porous pot electrodes from the SP data.

Figures 3.10 and 3.11 are plots of $SP_{diff_{t_i}}$ values along the profile lines shown on Figure 3.5 for hole-surface MALM. The profile locations were selected based on the conductive pathways identified in the hole-surface MALM contour maps to allow direct

comparison of the information derived from the two methods. A-A' is the south-north profile, and B-B' is the northwest-southeast diagonal profile of $SP_{diff_{t_i}}$ values. SP was affected by a greater amount of noise than hole-surface MALM as indicated by the large variations in $SP_{diff_{t_i}}$ values along each profile line. Large magnitude $SP_{diff_{t_i}}$ values at single points may represent readings at "weak" electrodes due to the loss of copper sulfate over time from specific porous pots. The most general feature seen in the plots of $SP_{diff_{t_i}}$ values is the continual development of very strong negative SP's over most of the study area as the tracer plume evolved. Segments along the profile lines where the SP values decreased most significantly (i.e., greater separation between the line graphs) and continually in magnitude over time are attributed to the presence of the tracer plume. Figure 3.10 (A-A') does not provide any strong
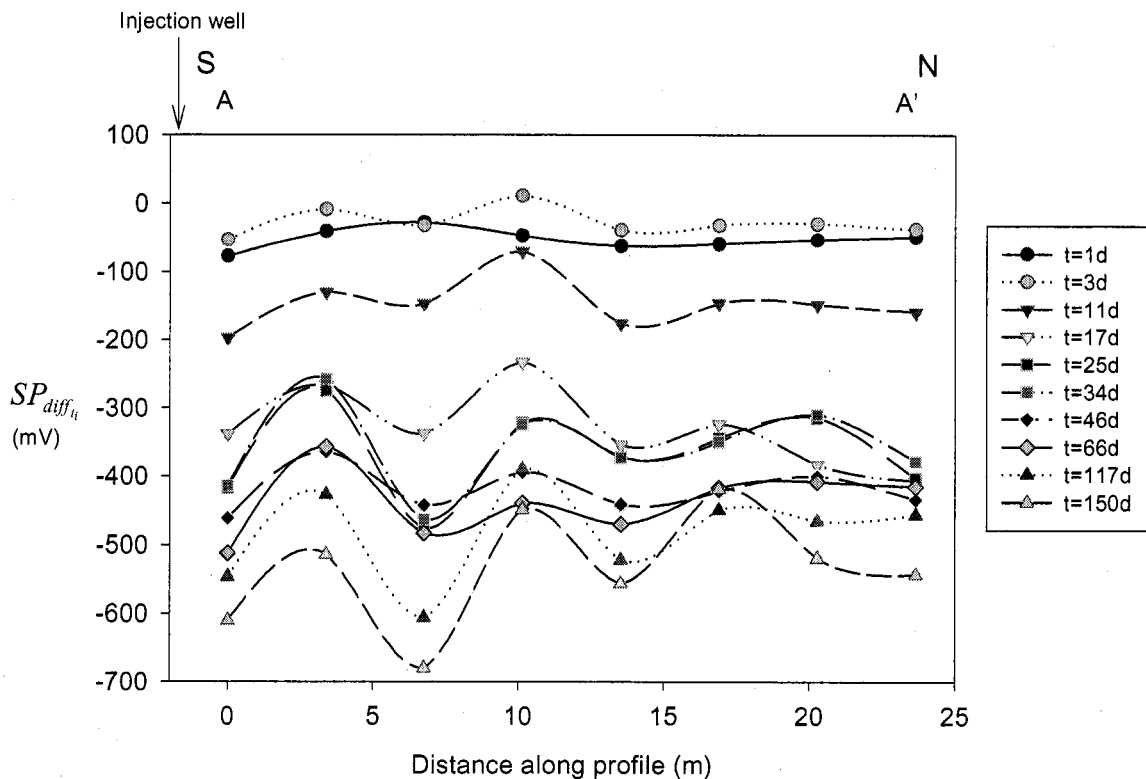
Figure 3.10. Plot of $SP_{diff_{t_i}}$ values along south-north profile A-A' (location of profile shown on Figure 3.5).

indications of the tracer plume's existence because SP values did not decrease continually over any portion of the profile line. Northwestern sections of profile B-B' (Figure 3.11), beginning on approximately t=11 d, show relatively more negative $SP_{diff_{t_i}}$ values and greater separation between the line graphs than along the rest of the profile suggesting presence of the plume. In addition, a major decrease in $SP_{diff_{t_i}}$ values was detected between t=11 d and t=17 d. This jump in $SP_{diff_{t_i}}$ values may have been caused by tracer reaching the water table. SP appeared to be more sensitive to migration of tracer to the water table than hole-surface MALM. $SP_{diff_{t_i}}$ values continually became more negative after t=3 d over most of profile B-B'.
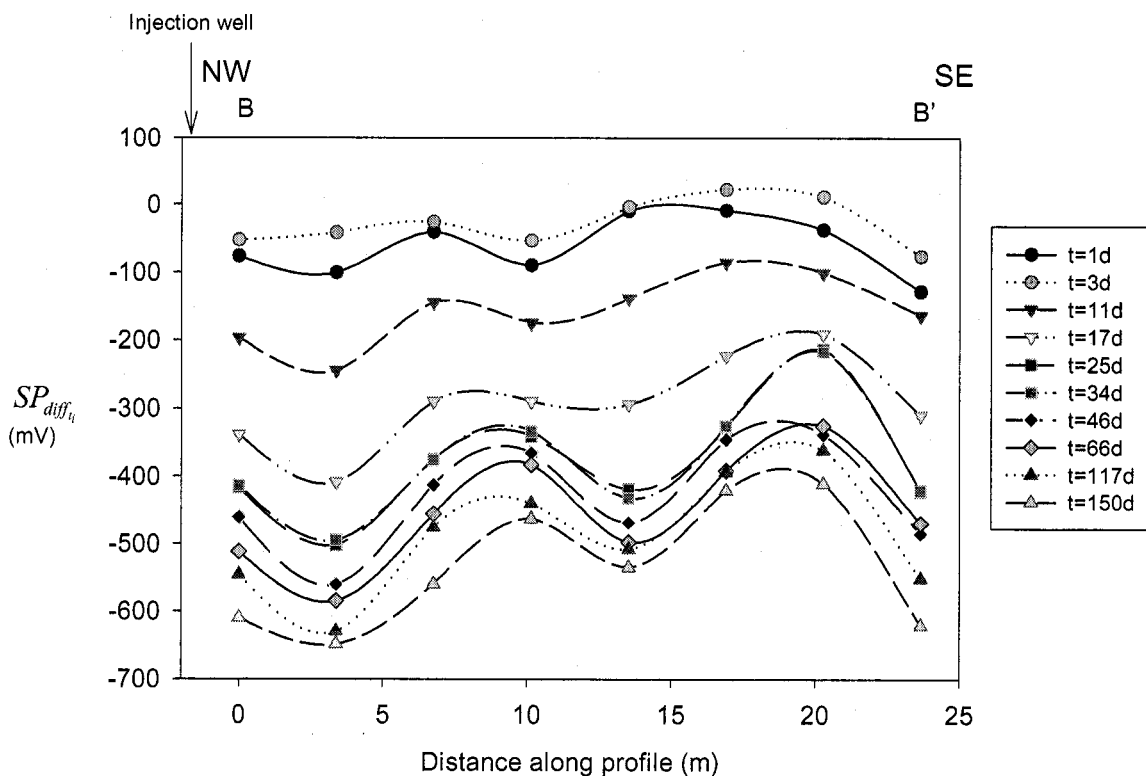
Figure 3.11. Plot of $SP_{diff_{t_i}}$ values along northwest-southeast diagonal profile B-B' (location of profile shown on Figure 3.5).

3.4.2.3. Vertical distribution of MALM potentials

Although hole-hole MALM is an invasive technique, it provides some general information about the vertical distribution of tracer near the wells. Figure 3.12 presents a representative hole-hole, cross section of equipotentials between ES3 and ES5 for t=11 d. The hole-hole potential data provide relatively little information near the observation wells and in the zones between the wells because there are very few data points available for kriging. However, the equipotentials near the injection well form a bull's eye suggesting that a preferential current pathway developed within the injection well. The location of this apparent pathway is consistent with a wet fracture zone detected during drilling of the well. This "weeping" fracture zone was visible in the borehole video log for the well that was produced shortly after drilling. It is believed that a current pathway formed in the injection well in response to preferential, current channeling through the electrolyte plume in this fracture zone.
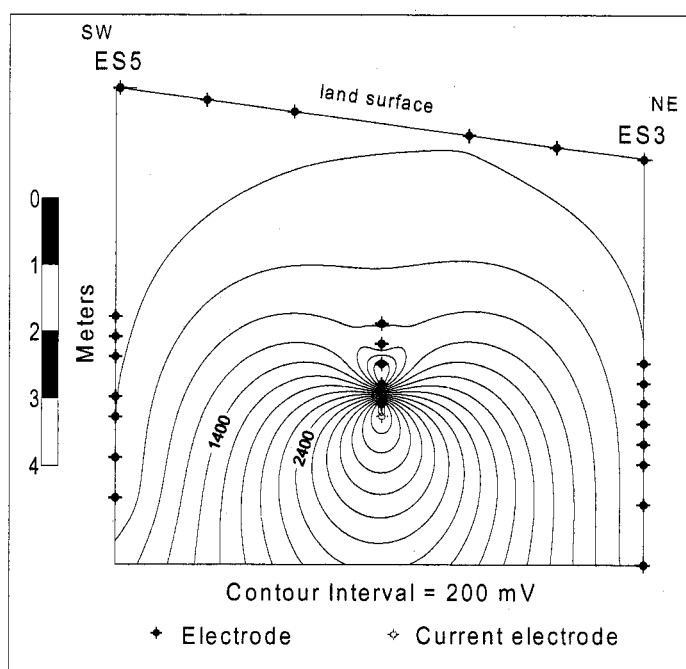
Figure 3.12. A representative hole-hole, equipotential, contour map between ES3 and ES5 for t=11d.

Potential data for each observation well, as $V_{rat_{25d}}$, $V_{rat_{46d}}$ and $V_{rat_{173d}}$, are presented in Figure 3.13. The profiles provide more information relative to vertical changes in potential than do equipotential, cross sections such as Figure 3.12. A general decrease in $V_{rat_{ti}}$ values occurred over time, consistent with the MALM hole-surface data. All of the profiles for the first 25 days of the experiment are relatively vertical and show little effects of the tracer plume. Slight bending in the profiles toward lower $V_{rat_{ti}}$ values (left) began after 46 d. Persistent, distinct deflections of the profiles toward lower $V_{rat_{ti}}$ values became much more pronounced by 173 d. Elevations of deflections toward lower $V_{rat_{ti}}$ values indicate
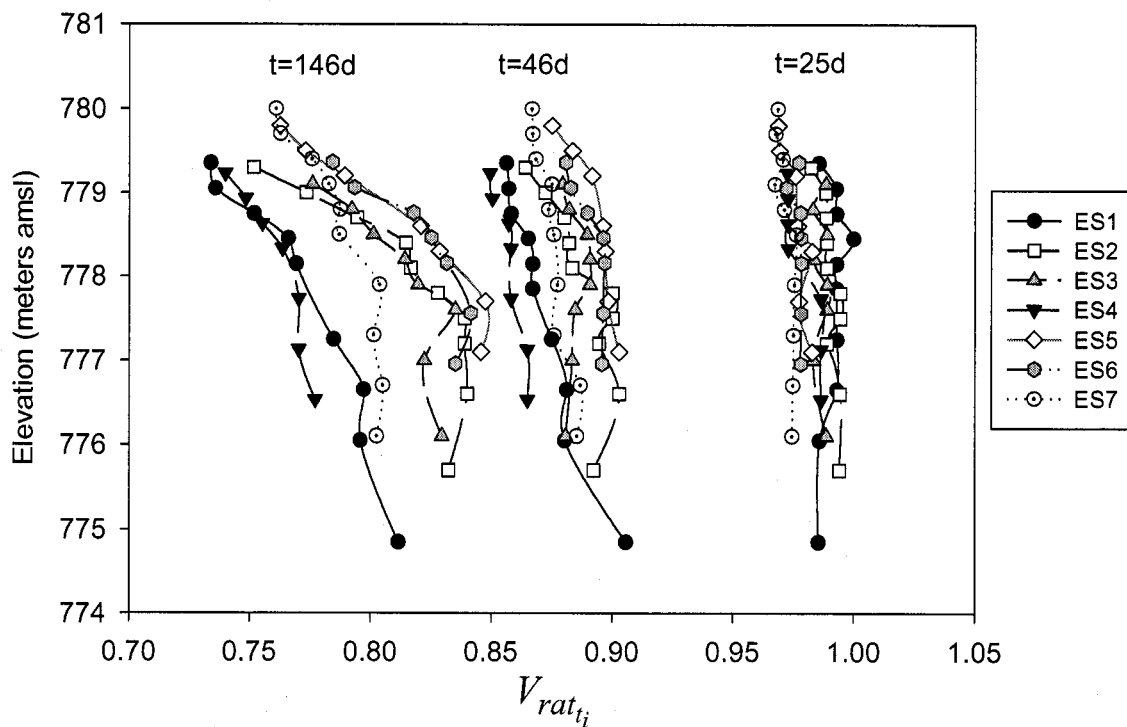
Figure 3.13. Plot of hole-hole MALM $V_{rat_{ti}}$ profiles for observation wells ES1 through ES7 for t=25 d, t=46 d and t=173 d.

approximate locations in the observation wells where resistivity decreased presumably due to tracer arrival and/or selective activation of localized clays. The greatest decrease in $V_{rat_{ti}}$

values occurred at the upper electrode locations in all seven wells, and the angle of deflection is similar for all wells. Another interesting feature in Figure 3.13 is that the profile lines for t=25 d are tightly grouped, but separation between lines became greater over time. Wells ES1 and ES4 have the greatest overall $V_{rat_{t_i}}$ decrease beginning on t=46 d and continuing through t=173 d. The group spread may be caused by the proximity of the tracer plume to the observation well, the concentration of the tracer, or the shape and position of the tracer plume. Timing of the decreases in $V_{rat_{t_i}}$ values correlates with measured increases in the EC of the water in the observation wells ES2, ES3, ES6 and ES7. However, it is not possible to quantify the volume or concentration of tracer that reached individual observation wells based on $V_{rat_{t_i}}$ values.

3.5. Summary

Hole-surface MALM is a minimally invasive and cost-effective technique that can be used to help delineate the lateral migration of conductive, tracer plumes in partially saturated fractured basalt. SP when combined with MALM provides additional details of the plume dynamics because SP does not involve a direct current like MALM. However, SP is affected by noise more than MALM and by itself does not provide enough information to delineate the tracer plume. The hole-surface MALM and SP measurements were not very sensitive to the injection of tap water during Phase 2 of the injection experiment. It is suspected that the threshold conductivity contrast needed for detection by hole-surface MALM and SP did not develop during Phase 2 of the experiment due to hydrodynamic dispersion in the basalt.

Hole-hole MALM is an invasive tool. However, it can provide very useful information about the vertical distribution and migration patterns of conductive tracers when used in combination with hole-surface MALM. Hole-hole MALM successfully delineated resistivity changes in the upper portion of the basalt flow due to tracer migration. Hole-hole MALM also defined the vertical location of an apparent current pathway that developed in the injection well during the experiment. However, hole-hole MALM was not very sensitive to Phase 2 of the experiment due to hydrodynamic dispersion within the basalt.

Acknowledgements

References

Archie, G.E., 1942. The electrical resistivity log as an aid in determining some reservoir characteristics. Am. Inst. Min. Metallurg. Pet. Eng. Tech. Paper 1422, 146-154.

Abaza, M.M.I., and Clyde, C.G., 1969. Evaluation of the rate of flow through porous media using electrokinetic phenomena. Water Resources Research 5 (2), 470-483.

Beasley, C.W., and Ward, S.H., 1986. Three-dimensional mise-á-la-masse modeling applied to mapping fracture zones. Geophysics 51 (1), 98-113.

Bevc, D. and Morrison, H.F., 1989. Borehole-to-surface electrical resistivity monitoring of a salt water injection experiment. Proceedings of the Society of Exploration Geophysicists 59th Annual International Exposition and Meeting, Oct. 29-Nov. 2, Dallas, TX, pp. 216-218.

Bevc, D. and Morrison, H.F., 1991. Borehole-to-surface electrical resistivity monitoring of a salt water injection experiment. Geophysics 56 (6), 769-777.

Birch, F.S., 1993. Testing Fournier's method for finding water table from self-potential. Ground Water 31 (1), 50-56.

Birch, F.S., 1998. Imaging the water table by filtering self-potential profiles. Ground Water 36 (5), 779-782.

Brown, S.R., 1989. Transport of fluid and electric current through a single fracture. Journal of Geophysical Research 94 (B7), 9429-9438.

Dey, A. and Morrison, H.F., 1979. Resistivity modeling for arbitrarily shaped three-dimensional structures. Geophysics 44 (4), 753-780.

Daily, W., and Ramirez, A., 1995. Electrical resistance tomography during in-situ trichloroethylene remediation at the Savannah River Site. Journal of Applied Geophysics 33, 239-249.

Fried, J.J., 1975. Groundwater Pollution, Theory, Methodology, Modelling and Practical Rules. Elsevier, New York, 330p.

Hosterman, J.W., Schied, V.E., Allen, V.T., and Sohn, I.G., 1960. Clay Deposits in the Palouse Hills area, In Investigations of clay deposits in Washington and Idaho. General Printing Office, Washington: United States.

Keller, G.V., 1987. Rock and Mineral Properties. Electromagnetic Methods in Applied Geophysics - Theory, Vol. 1, Society of Exploration Geophysicists, pp. 13-51.

Keller, G.V., and Frischknecht, F.C., 1966. Electrical Methods in Geophysical Prospecting. International Series of Monographs in Electromagnetic Waves, Vol. 10, Pergamon, New York, 525p.

Nimmer, R.E., Osiensky, J.L., and Sprenke, K.F., 2001. Borehole-surface and cross-borehole mise-à-la-masse delineation of a radial injection tracer experiment in partially saturated fractured basalt. Proceedings of SAGEEP'01, Mar. 4-7, Denver, CO, (BHL-2).

Nourbehecht, B., 1963. Irreversible Thermodynamic Effects in Inhomogeneous Media and Their Application in Certain Geoelectric Problems. Ph.D. Thesis, Massachusetts Institute of Technology, Cambridge, MA.

Osiensky, J.L., 1995. Time series electrical potential field measurements for early detection of groundwater contamination. J. Environ. Sci. Health, A30 (7), 1601-1626.

Osiensky, J.L., and Donaldson, P.R., 1995. Electrical flow through an aquifer for contaminant source leak detection and delineation of plume evolution. Journal of Hydrology 169, 243-263.

Osiensky, J.L., 1997. Ground water modeling of mise-à-la-masse delineation of contaminated ground water plumes. Journal of Hydrology 197, 146-165.

Parasnis, D.S., 1967. Three-dimensional electric mise-à-la-masse survey of an irregular lead-zinc-copper deposit in central Sweden. Geophys. Prosp., 15 (3), 407-437.

Parkhomenko, E.I., 1967. Electrical Properties of Rocks, Monographs in Geoscience. Plenum Press, New York, 314p.

Provant, A.P., 1995. Geology and Hydrogeology of The Viola and Moscow West Quadrangles, Latah County, Idaho and Whitman County, Washington. M.S. Thesis, University of Idaho, Moscow, ID.

Sato, M., and Mooney, H.M., 1960. The electrochemical mechanism of sulfide self-potentials. Geophysics 25 (1), 226-249.

Schlumberger, C., 1920. Etude sur la prospection electrique du sous-sol. Gauthier-Villars, Paris, 94p.

Sharma, P.W., 1986. Geophysical Methods in Geology. PTR Prentice-Hall, Inc., New Jersey, 442p.

Sharma, P.V., 1997. Environmental and Engineering Geophysics. Cambridge University Press, United Kingdom, 475p.

Sill, W.R., 1982. Diffusion Coupled (Electrochemical) Self-Potential Effects in Geothermal Areas. Report to the U.S. Dept. of Energy, Contract No. DE-AC07-80ID12079, University of Utah, Salt Lake.

Sjostrom, K.J. and Sill, W.R., 1991. An electrical technique for the determination of ground water flow parameters. Proceedings of SAGEEP'91, Mar. 11-14, Knoxville, TN. pp.119-127.

Street, G.J., Perry, A., and Greenham, L.J., 1993. Geophysical surveys of leaking tailings impoundments. Exploration Geophysics 24, 801-804.

Stierman, D.J., 1984. Electrical methods of detecting contaminated groundwater at the Stringfellow Waste Disposal Site, Riverside County, California. Environ. Geol. Water Sci. 6 (1), 11-20.

Telford, W.M., Geldart, L.P., and Sheriff, R.E., 1990. Applied Geophysics. Cambridge University Press, United Kingdom.

Thanassoulas, C.P., 1989. Application of the self potential technique over the Milos Geothermal Test Site. Geothermics 18 (4), 497-505.

Thanassoulas, C.P., and Lazou, A., 1993. The Nestos Delta Geothermal Field and its relation to the associated self potential (SP) field. Geothermics 22 (2), 117-134.

Wang, T., Stodt, J.A., Stierman, D.J., and Murdoch, L.C., 1991. Mapping hydraulic fractures using a borehole-to-surface electrical resistivity method. Geoexploration 28, 349-369.

White, P.A., 1988. Measurement of ground-water parameters using salt-water injection and surface resistivity. Ground Water 26 (2), 179-186.

White, P.A., 1994. Electrode arrays for measuring groundwater flow direction and velocity. Geophysics 59 (2), 192-201.

Wilt, M.J., and Tsang, C.F., 1985. Monitoring of subsurface contaminants with borehole/surface resistivity measurements. Lawrence Berkeley Laboratory Report LBL-19106, pp. 176-177.

CHAPTER 4: CHARGED BODY POTENTIAL MONITORING OF AN ELECTROLYTE PLUME EMINATING FROM A DRIPPING SOURCE[3]

Robin E. Nimmer and James L. Osiensky

Department of Geological Sciences, University of Idaho, Moscow, ID 83844-3022,USA

Abstract

Hole-surface charged body potential (CBP) measurements were taken over a 173-day period during a drip-injection, tracer experiment in partially saturated, fractured basalt. A continuous, enhanced conductivity, potassium chloride (KCl) solution was dripped into the fractured basalt and energized directly through a current electrode placed in the conductive solution. The constant concentration, KCl solution was introduced above a perched water table at an average rate of 10.07 liters/day under a constant hydraulic head for 76 days. The KCl drip period was followed by a 34-day tap water drip period and a 62-day drainage period. Hole-surface CBP measurements were taken over time to delineate the evolution of the asymmetrical, vadose zone, plume. A 15 by 15 grid of land surface based, porous pot electrodes (copper sulfate), located symmetrically about the centrally located injection borehole, was used for the hole-surface CBP experiment. Ratios of electrical potentials measured at the land surface over time were contoured and profiled to delineate the evolution of the electrolyte plume.

Key words: Charged body potential method, fractured basalt, vadose zone, electrical potentials, electrical conductivity, plume, voltage ratios

---

4.1. Introduction

Electrical geophysical methods generally provide cost effective and noninvasive tools to help delineate contaminated zones and preferential flow paths that contain fluids with contrasting electrical properties. Because the electrical properties of porous media are dominated by the porosity fraction, and the conductivity of the fluids that exist in the pore spaces (Archie, 1942; Keller and Frischnecht, 1966), the introduction of conductive fluids (e.g. inorganic contaminants) into the pore spaces will increase the electrical conductivity contrast with the rest of the porous media. Therefore, conductive contaminants that leak into the subsurface may form a conductive target body that takes the geometric form of the preferential flow paths through which the contaminants migrate.

A variation of galvanic resistivity methods known as the charged body potential (CBP) method or the mise-à-la-masse method was developed originally to delineate the extent of electrically anomalous zones in the subsurface (Parasnis, 1967). Specifically, the CBP method was designed to map electrically conductive earth materials by passing a current directly into the zone of interest while electrical potentials are measured at the land surface or in boreholes (Parasnis, 1967).

Many investigators (far too many to include here) have used or have simulated various surface and hole-surface resistivity methods, to evaluate environmental applications. Only a selected few are mentioned here. Fried (1975) described the use of electrical resistivity measurements to evaluate the velocity and direction of migration of a sodium chloride tracer from a single well. Stierman (1984) used the CBP method to detect contaminated ground water near a waste disposal site. White (1988, 1994) described use of the method of Fried (1975) in New Zealand. Sjostrom and Sill (1991) and Bevc and Morrison (1989, 1991) used hole-to-surface electrical methods to track the movement of saline tracers in ground water. Frangos (1992) used a grid of subsurface electrodes placed below a synthetically lined, disposal pond to detect leaks in the liner. Street et al. (1992) used the CBP method to detect seepage from a leaking PVC lined tailings pond. Osiensky (1995), and Osiensky and Donaldson (1995) described a modified CBP experiment to delineate a tracer plume in fluvial sediments. Osiensky (1997) simulated CBP measurements

to define plume length and center of mass for several hypothetical contaminant plumes. Daily et al. (1995) evaluated the use of electrical resistance tomography (ERT) to detect a controlled gasoline spill and hydrocarbon leaks from above ground storage tanks. Ramirez et al. (1996) evaluated ERT as a leak detection system for metal underground storage tanks. Binley et al. (1997) used CBP measurements to detect leaks from waste disposal ponds, pipes and tanks. Nimmer et al. (2001) described hole-surface and cross-borehole CBP measurements during the first 34 days of the experiment described herein.

For this paper, the target body of interest was a moderately conductive, electrolyte plume emanating from a vertical borehole filled with a potassium chloride (KCl) solution. The borehole was located in the vadose zone and penetrated fractured basalt to the top of a perched water table. A slowly evolving, irregularly shaped, plume developed over time as KCl solution was dripped continuously into the borehole. KCl solution emanating from the borehole was considered to be similar to a relatively slow leak in an underground storage tank or seepage emanating from a waste disposal facility.

4.2. Fundamental considerations

The CBP method allows for the direct measurement of the electrical potential distribution about a single, point source of electric current. The resulting electrical potential distribution for an area of investigation incorporates all factors that contribute to its development at the particular time of measurement. However, where baseline data can be collected, subsequent data sets can be evaluated for changes that occur over time.

According to Keller (1967), the electrical conductivity of porous media is given by the Archie (1942) formula as:

$$\sigma_m = a\sigma_w S^n \phi^m \qquad \text{Eqn. 4.1}$$

where: ϕ is the porosity, S is the fraction of pores containing water (i.e., $S = 1$ for complete saturation), σ_w is the electrical conductivity of the pore water, m is an empirical exponent based on the texture of the rock, a and n are empirical constants used to force the formula to fit the behavior of the rock type of interest.

According to Keller and Frischknecht (1966), 95% of electrical conductivity measurements in Columbia River basalts fall within the range between 0.0076 S/m and 0.002 S/m, with an average of 0.00389 S/m. Values for m typically range from about 1.44 in highly porous volcanic rock to 1.58 in dense igneous rock with porosities less than 4%; values for a typically range from about 3.5 for highly porous volcanic rock to 1.4 in dense igneous rock (Keller, 1967).

For a given porosity and water saturation, fracture porosity typically will exhibit the highest rock conductivity due to the simpler shape of the pores while vuggy porosity will result in the lowest conductivity because of the complex pores (Keller, 1987). Changes in the electrical potential distribution that occur over time are due to changes in the electrical conductivity of the porous medium. If the effects of "noise" can be identified and separated from the measured electrical potentials, the differences between baseline and subsequent data sets will reflect changes in the moisture contents and/or the electrical conductivity of the pore water in accordance with the Archie (1942) formula.

4.3. Field demonstration

4.3.1 Site geology

The test site for this field demonstration is located on the University of Idaho campus in Moscow, Idaho along the eastern edge of the Columbia River Basalt Plateau. The experiments were conducted in the weathered and fractured, uppermost basalt flow (i.e., the Lolo Flow of the Priest Rapids Member) of the Wanapum Formation, which dates to 14.5 million years ago (Bush and Seward, 1992).

The uppermost stratigraphic unit at the site consists of 1.5 to 2 meters of alluvial sediments and Pleistocene Palouse loess (Provant, 1992). The loess (silt and clayey silt) is composed of paleosols combined with eolian volcanic, glacio-fluvial and glacio-lacustrine sediments. The alluvial sediments are made up of reworked loess with basalt and granite fragments.

4.3.2 Tracer test

A 173-day, time-series, field experiment was completed to test hole-surface CBP measurements as a fast, efficient method to detect the presence, and track the evolution, of inorganic contaminants leaking into a shallow aquifer. The field experiment was conducted from November 6, 1999 to April 27, 2000.

Eight, 0.15 m-diameter, vadose zone, boreholes were drilled with air-rotary (no water added) for several experiments (Figure 4.1). Details of some of the additional experiments are discussed by Nimmer and Osiensky (2002). The upper portion of each borehole was cased with 0.15 m diameter, schedule 80, PVC plastic pipe through the sediments. One centrally located injection borehole was surrounded by seven monitoring wells. The injection borehole was left as uncased open borehole in the basalt. Each monitoring well was constructed with an inner casing of schedule 40, 0.05 m (2 inch) diameter, PVC pipe. The bottom 0.30 m of each PVC pipe contained hacksaw slots to allow for the sampling of KCl solution that migrated to the bottoms of the monitoring wells during the experiment.
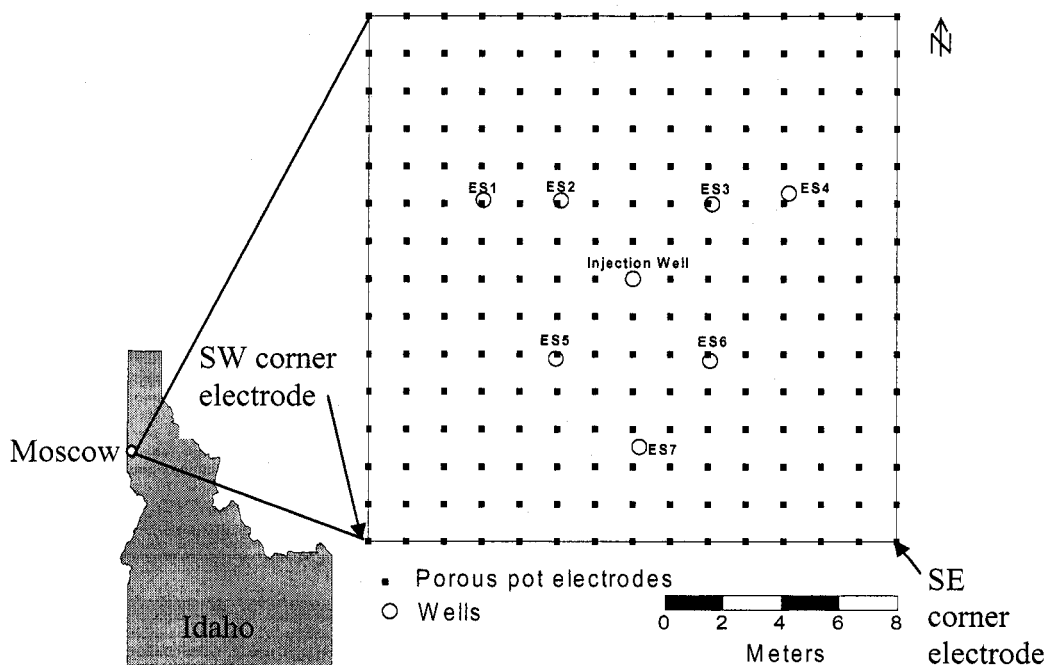
Figure 4.1. Site location map and location of wells and porous pot electrodes.

The PVC pipe was centered in each borehole and each annulus was filled with 30 cm of fine sand followed by dampened silt, tamped into place to the land surface. Well conditions were allowed to equilibrate for 60 days prior to the collection of baseline data for these experiments.

The completion depths for the monitoring wells were based on the depth of perched ground water relative to a gently sloping land surface. The deepest well is 7.49 m below land surface. The current electrode was placed 10 cm above the bottom of the uncased, injection borehole, and was constructed of 14 gauge copper, Type UF underground feeder cable. Figure 4.2 shows the well logs for each well. This figure shows the degree of variability of the weathered and unweathered zones in the basalt within a matter of a few meters.
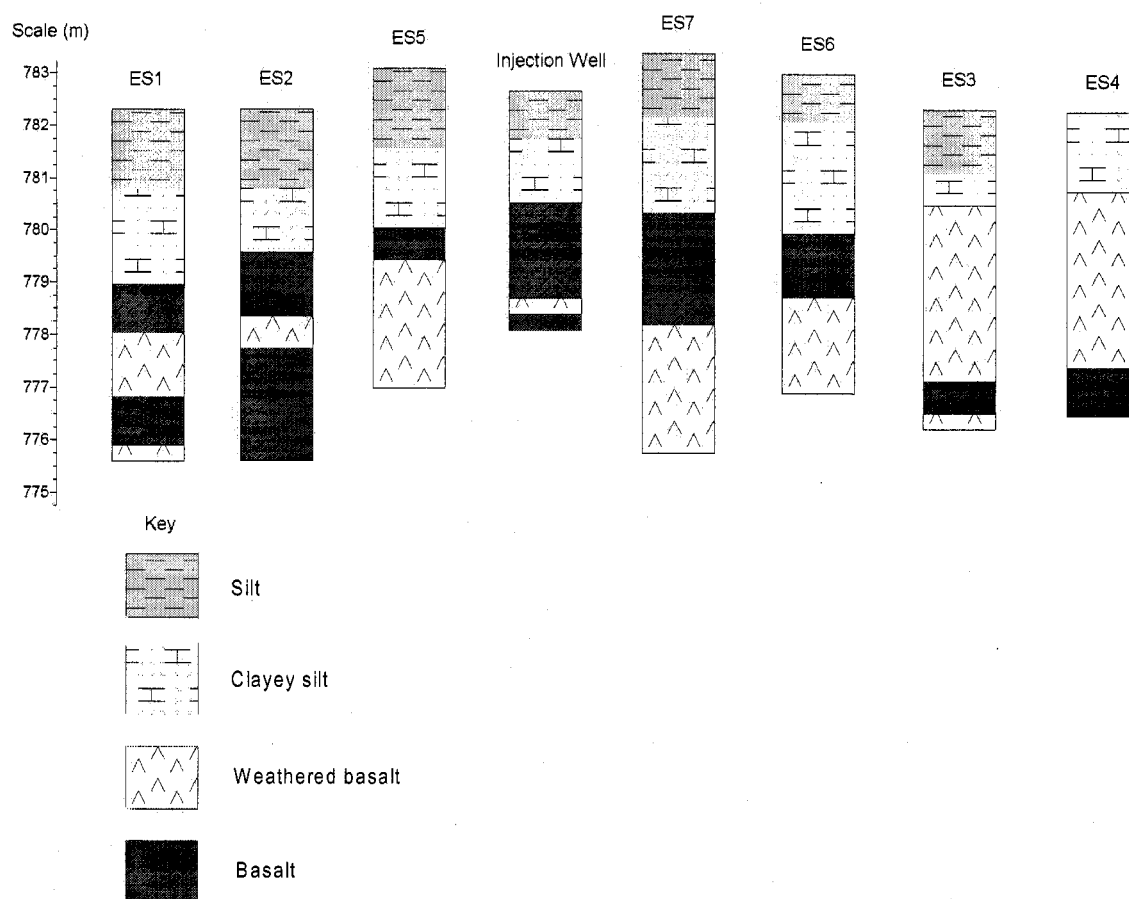
Figure 4.2. Well logs for observation wells and the injection well.

Baseline and time-series, hole-surface CBP measurements were taken on a fixed, grid of land surface potential electrodes. The grid consisted of a 15 by 15 array of 224 disposable, copper sulfate, porous pot electrodes on 1.3-meter centers located symmetrically about the injection borehole (Figure 4.1). This grid was used to give complete coverage of the area of interest and partly to be consistent with a finite-difference model used to aid data interpretation. All electrodes were permanent and remained undisturbed for the duration of the time-series experiments. The porous pot electrodes were buried 15 centimeters below the ground surface and kept moist (i.e., soil around each pot was wetted with de-ionized water when necessary) during a 52-day equilibration period prior to commencement of the experiments. A moderate rainfall event just prior to the collection of baseline data provided uniform soil moisture over the test area. Therefore, it was not necessary to wet the soil around the pots artificially during the experiment to maintain good electrical contact.

The reference electrode consisted of a porous pot as described above that was located at the land surface (buried 15 cm) 74.5 m to the west of the injection well. The distant current electrode (i.e., current sink) consisted of three stainless steel stakes driven 0.3 m into the surface soil 62.4 m to the southwest of the injection well. All electrical connections were weather proofed with silicone rubber caulk and electrical tape to preclude any current leakage. In addition, all wires were elevated above the ground surface.

The current source for the CBP experiment was a portable, lead-acid battery, powered GISCO ResiStar RS-100M™ transmitter/receiver system. The transmitter generated rectangular pulses as exciting signals of alternate polarity. A 2-cycle, 1-second period, time-domain signal was transmitted for all CBP measurements because of time constraints imposed by additional experiments. Several other signal lengths were evaluated during baseline testing and the 2-cycle, 1-second period was found to give satisfactory results. All CBP measurements were evaluated for integrity, and readings with standard deviations greater than 1.0 % were filtered from each data set prior to analysis.

At time $t = 0d$ (days), the injection borehole was filled with 34.8 liters (l) of KCl solution with a constant, electrical conductivity of 0.601 Siemens/m (S/m) from a heated, polyethylene storage tank. To avoid density effects, this KCl solution was only moderately conductive compared to some other experiments in the literature where highly conductive tracers were used (e.g., Slater et al., (1997) Slater et al., (2000), used sodium chloride (NaCl)

tracers with a conductivity of 8 S/m). KCl was used in this experiment rather than NaCl to minimize swelling of clays (derived from the weathered basalt) within the fractures. The filled borehole formed a 1.91 m-long column of conductive solution from the bottom of the borehole to the top of the basalt layer, 2.67 m below land surface. A constant head was maintained at the top of the basalt layer for the duration of the drip period (110 d) with a nearly constant, average drip rate of 10.07 l/d. A total of 765 l of KCl solution was dripped into the borehole over the first 76 days of the experiment followed by 342 l of tap water with an electrical conductivity of 0.0294 S/m over the next 34 days.

4.4. Results and data interpretation

4.4.1 Introduction

Post-baseline CBP measurements were taken 19 times over the 173-day experiment. Baseline data for the hole-surface CBP experiment were collected five days prior to introduction of the KCl solution. The baseline data set was collected under the conditions of an empty injection borehole with the exception of 10 cm of standing water that drained from an overlying, perched, fracture zone after drilling. This water, with a conductivity of 0.1153 S/m, submerged the current electrode. Subsequent CBP measurements began t=0.83d after the injection borehole was first filled (t=0d) with KCl solution.

4.4.2 Data analyses

Variations in soil temperature and soil moisture contents (i.e., soil suction) between measurement periods were recorded during this experiment; their significance on the CBP measurements was not quantified but was examined qualitatively. Between November 23 and December 10, 1999, the surface soils became nearly saturated after significant rainfall events. Around December 3, 1999 the soil temperature dropped to approximately 3°C and remained within the range from 4°C to 1°C to the beginning of March. Figure 4.3 shows soil temperature, soil moisture contents (i.e., soil suction), and CBP profiles for the two southern-most corner porous pot electrodes (SW and SE) in the electrode grid (Figure 4.1). These porous pots were used as control pots in this instance because the KCl plume is believed to

have migrated mainly to the north (illustrated later in the paper). Except for the steady downward trend in voltages, the vicinity effects of the evolving plume are believed to have been minor at these two electrodes. The two profiles in Figure 4.3 are relatively parallel to each other throughout the length of the experiment. The "spikey" variations in soil moisture and soil temperature do not correlate with changes in voltage at the two control pots. This suggests that no direct relationship existed between the CBP measurements over the 15 by 15 grid of porous pot electrodes, and variations in soil moisture and soil temperature that occurred during the experiment.
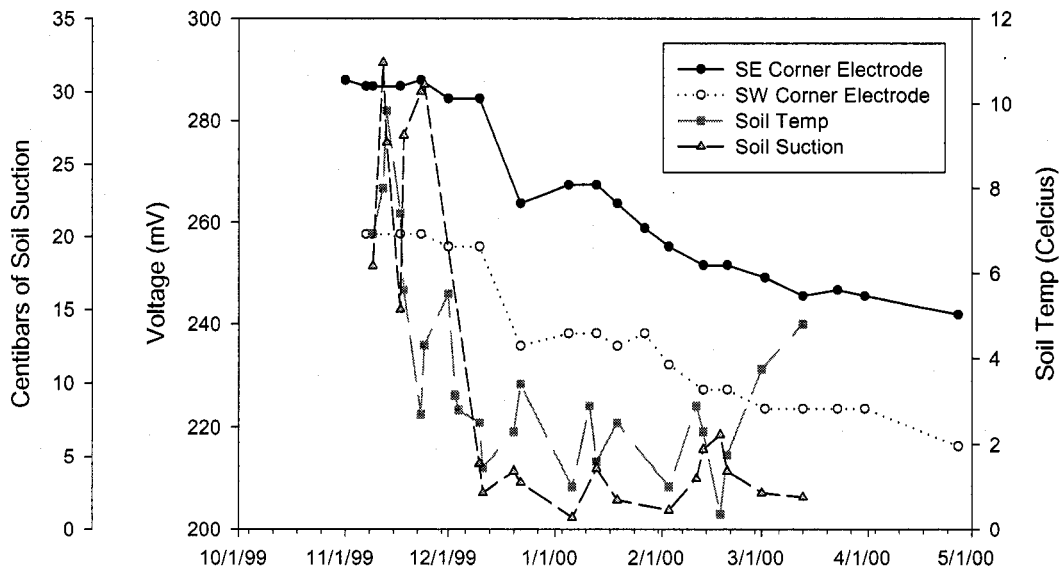
Figure 4.3. Plot of voltages at corner southernmost electrodes of grid array (SE and SW), soil suction and temperature (see Fig. 1 for electrode locations).

The data are presented as shaded contour maps (plan view) and profiles (cross sectional view) of V_{rat_t} values (voltage ratios) to delineate the spatial distribution of changes in apparent resistivity due to migration of the KCl solution. All contour maps presented in this paper were produced with SURFER© 7 using the nearest neighbor method to grid the electrical potential data at their actual measurement locations (i.e., no interpolation). Individual CBP data sets were evaluated relative to the baseline data set as the ratio of voltages for each time (t) in accordance with (Daily et al, 1995):

$$V_{rat_t} = \frac{V_t}{V_{t_0}}$$
Eqn. 4.2

where: V_t are the voltage measurements for the data set of interest and V_{t_0} are the voltage measurements for the baseline data set.

4.4.3 Hole-surface CBP measurements

Figure 4.4 is a contour map of the baseline ($t = 0d$) electrical potentials in millivolts (mV) for the grid of porous pot electrodes. This figure suggests that one very distinct, relatively conductive, anomaly trends southward away from the injection borehole. In addition, a distinct east-west trending anomaly along the northern edge of the grid of electrodes is obvious. The baseline resistivity of the site, based on evaluations of drill cuttings for the wells (Figure 4.2), is highly variable within the small area of the test site (i.e., <350 m^2). Hydrated halloysite clay, an in situ weathering by-product of the basalt, and kaolinite clay, transported from the overlying Palouse loess, fill portions of many of the fractures; minor amounts of ilmenite clay also are present in many of the fractures (Hosterman et al, 1960). All of the boreholes except the injection borehole (most shallow)

Contour Interval = 20 mV
0 2 4 6
Meters
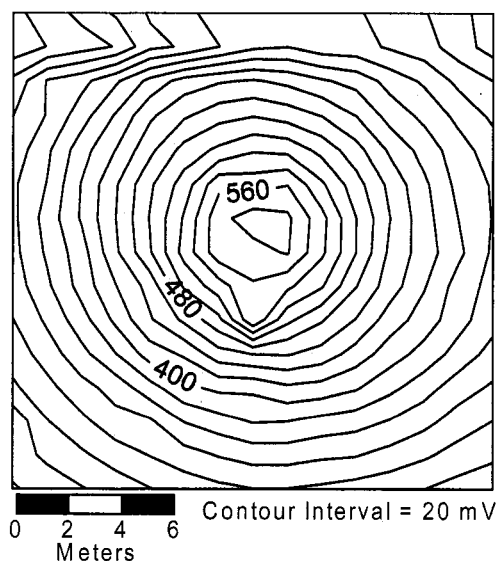
Figure 4.4. Contour map of electrical potentials (voltages) under baseline conditions.

penetrated weathered basalt with fractures partially filled with clay.

Ratios of the voltages for the first data set ($V_{rat_{0.83d}}$) were mapped to evaluate changes in the electrical potential field caused by addition of KCl solution to the injection borehole (Figure 4.5). The "pseudo-plume" shaped anomalies in Figure 4.5 reflect the combined effects of borehole irregularities and permeable fracture zones filled with perched ground water. That is, the column of KCl solution in the borehole took the shape of the actual borehole and provided an electrical conduit for preferential current flow directly into the fractures containing water. This changed the current density significantly within the borehole compared to the baseline case and accentuated the details of the electrical pathways. However, all voltage changes due to filling of the borehole were less than 5%, which normally would be considered noise.
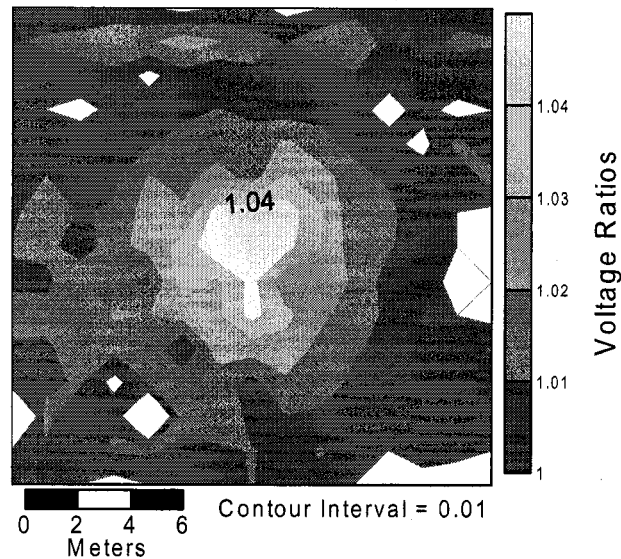
Figure 4.5. Shaded contour map of voltage ratios greater than 1.0 for $V_{rat_{0.83d}}$. Locations with voltage ratios less than 1.0 are depicted as white areas on the map.

About 8 liters of KCl solution migrated away from the injection borehole between filling of the borehole and the time that the first post-baseline data set was completed ($0.83d$). This small volume of solution was considered to be insignificant relative to the 173-d experiment evaluated herein. Therefore, from this point on in the data analysis,

$t = 0.83d$ was considered to be the "new" baseline data set from which changes in the electrical potential distribution were evaluated over time. Voltage ratios for all measurement periods beyond $t = 0.83d$ were calculated by:

$$V_{rat_{t_i}} = \frac{V_{t_i}}{V_{0.83d}}$$

Eqn. 4.3

where: t_i is the elapsed time in days since introduction of KCl solution.

$V_{rat_{t_i}}$ distributions over time were mapped within the region of the porous pot electrode grid. Figure 4.6 presents contour maps for the selected measurement periods $V_{rat_{3d}}$, $V_{rat_{34d}}$, $V_{rat_{68d}}$, $V_{rat_{99d}}$, $V_{rat_{128d}}$ and $V_{rat_{173d}}$. All contoured changes greater than 5% are shown as darker regions with $V_{rat_{t_i}} < 1$ (i.e., voltages were greater in the baseline data set). Zones with less than 5% change from baseline are mapped as $V_{rat_{t_i}} = 1$. No significant electrical conductivity increase was detected in water samples collected from the monitoring wells during the first 34 days of the experiment (Figure 4.7). No definitive changes in moisture contents in the basalt were detected by neutron moisture probe measurements in the monitoring wells during this time period. Major spatial changes in voltage were detected for $V_{rat_{68d}}$ through $V_{rat_{173d}}$. In addition, the KCl solution is believed to have migrated to four of the seven monitoring wells during the 173-day experiment based on changes in the electrical conductivity of the ground water (Table 1). Changes in the electrical conductivity of the water in these monitoring wells were consistent with development of the plume anomalies shown in Figure 4.6.

Figures 4.8, 4.9 and 4.10 present profiles of $V_{rat_{t_i}}$ values for the cross section locations shown in Figure 4.6. These profiles illustrate that potentials were relatively stable (i.e., $V_{rat_{t_i}} < 5\%$ change and only minor undulations from horizontal) until day 25 after KCl solution was introduced. A significant drop in potentials is seen in the profiles between $t = 34d$ and $t = 46d$. In addition, a steady downward trend in potentials across the entire grid of porous pot electrodes began with $V_{rat_{46d}}$ along with significant deepening of a trough in the data plot due to growth of the plume.
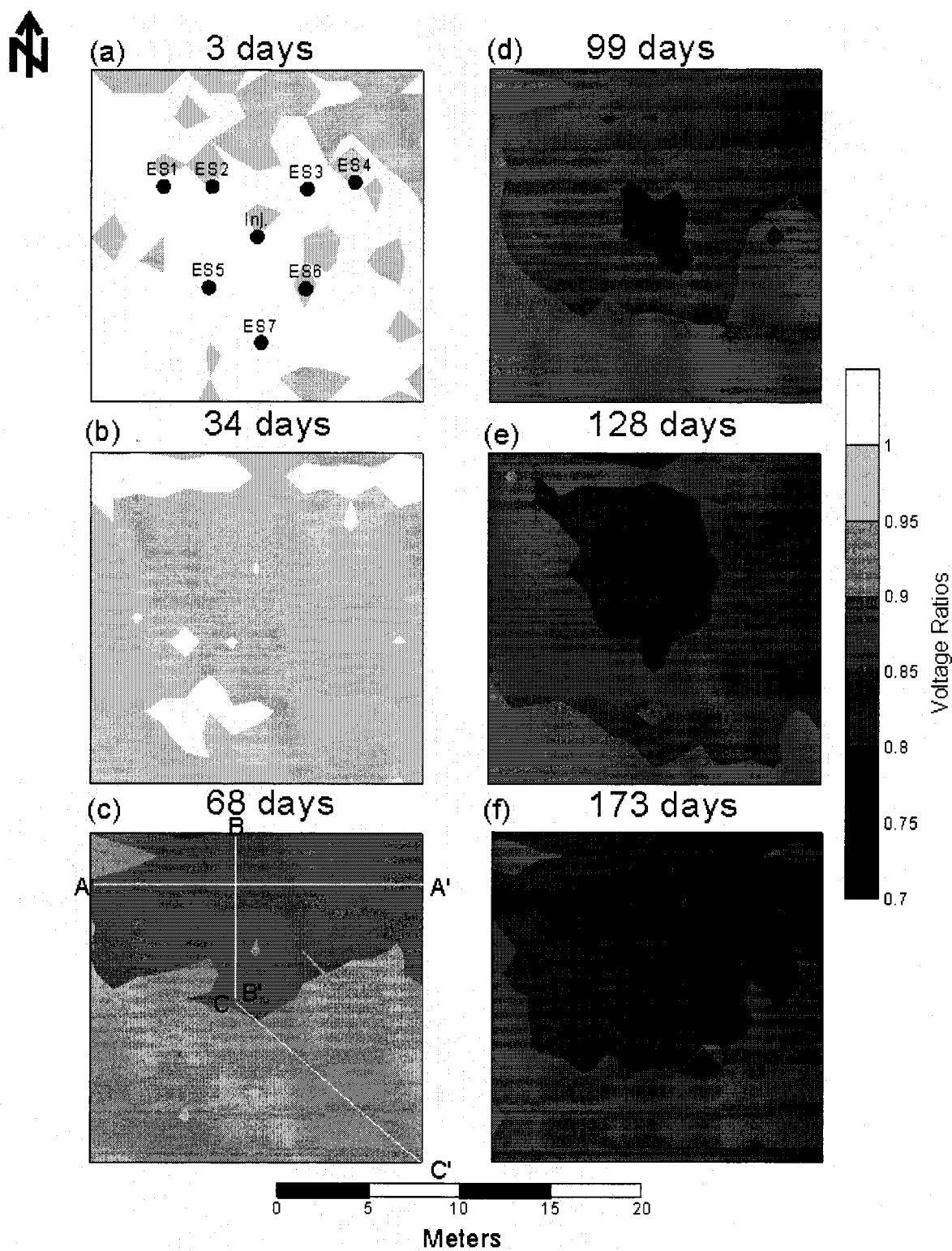
Figure 4.6. Shaded contour maps of voltage ratios for the selected measurement periods $V_{rat_{3d}}$, $V_{rat_{34d}}$, $V_{rat_{68d}}$, $V_{rat_{99d}}$, $V_{rat_{128d}}$ and $V_{rat_{173d}}$.
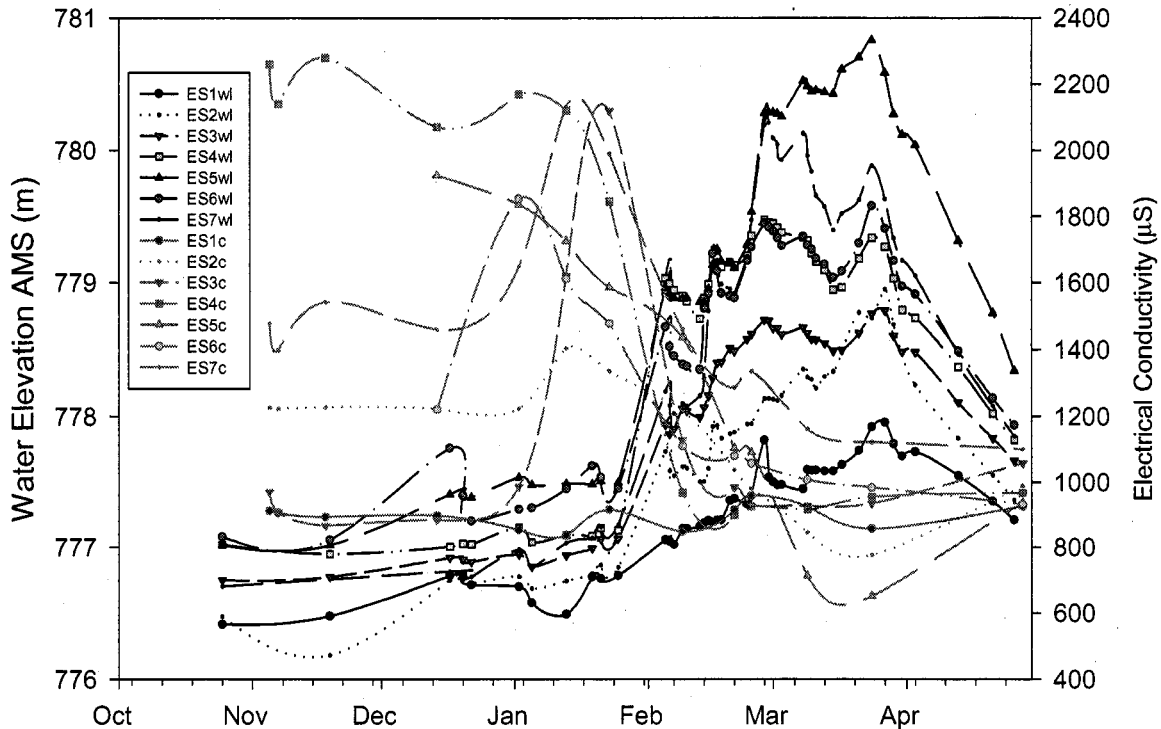
Figure 4.7. Water level elevations and electrical conductivity values for the monitoring wells before and after introduction of KCl solution. Gray lines represent electrical conductivities and the black lines represent water level elevations.

Two coincidental, unrelated events transpired between time periods $t = 74d$ and $t = 82d$. First, drip injection of KCl solution was discontinued on day 76 of the experiment. The injection borehole was pumped dry with a portable centrifugal pump and the borehole was refilled with tap water to begin the tap water, drip injection period; this process took approximately one hour. Second, water levels in the monitoring wells began to rise due to seasonal recharge. It was expected that these changes would tend to dilute the KCl plume and actually diminish its definition by the CBP method. In addition, disproportionate water level fluctuations (Figure 4.7) caused the hydraulic gradients to shift direction and magnitude over time. However, the plume anomaly generally remained fairly stable for the duration of the experiment. It is obvious that the plume anomaly evolved laterally to the north and

northeast (Figure 4.6). However, the vertical distribution of the KCl plume cannot be delineated with the data available.

The tap water, drip injection portion of the experiment concluded 110d after the start of the test; this portion of the experiment lasted for 34d . The drainage phase continued through the remainder of the test. The plume anomaly continued to evolve toward the north (Figure 4.6); however, due to water level fluctuations and changing hydraulic gradients, the direction and velocity of migration varied some over the course of the measurement period.
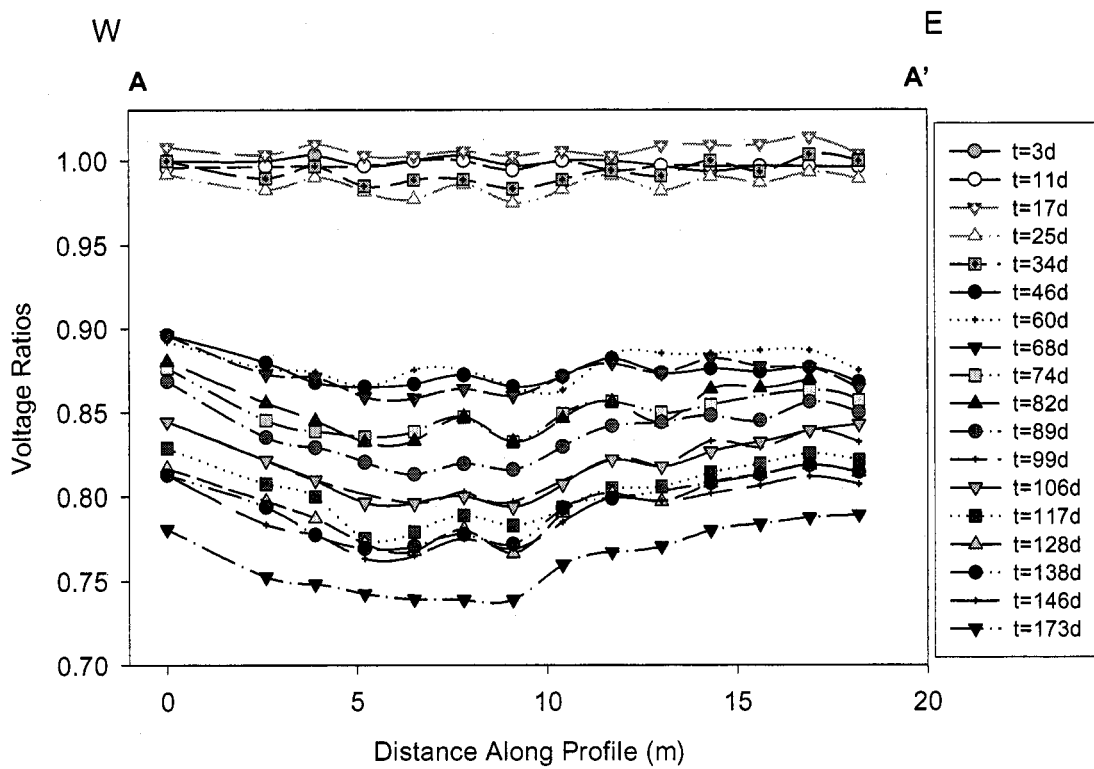
Figure 4.8. West to east profile (A-A') of CBP voltage ratios ($V_{rat_{t_i}}$ values) along row 3 of the grid of porous pot electrodes for all measurement periods (see Figure 4.6 for location of profiles).
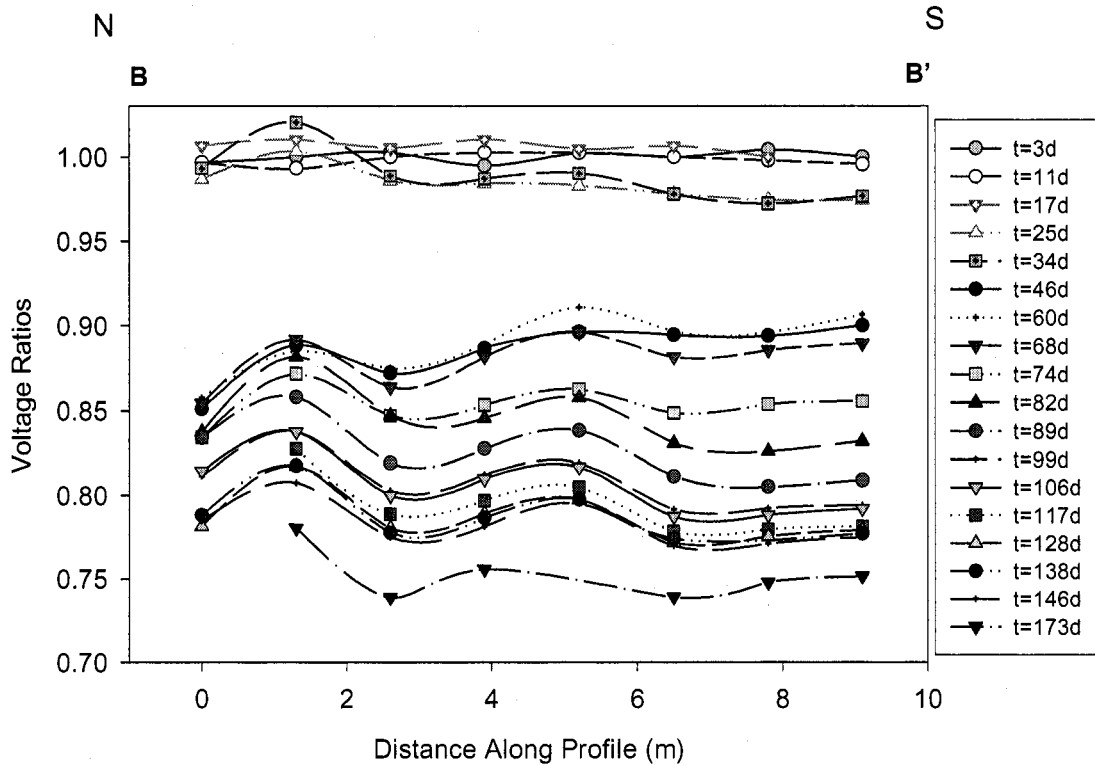
Figure 4.9. North to south profile (B-B') of CBP voltage ratios ($V_{rat_{t_i}}$ values) along the north half of column 9 of the grid of porous pot electrodes for all measurement periods (see Figure 4.6 for location of profiles).

4.5. Conclusions

Hole-surface CBP measurements were shown to be a fast, efficient method to detect the presence of conductive solutions leaking into shallow ground water. Hole-surface CBP measurements delineated the evolution of the conductive plume in the vadose zone over the 173-day measurement period. Noise related to soil moisture and soil temperature variations is not believed to have significantly influenced the CBP measurements during the experiment. In addition, the rising perched water table, and water level fluctuations changed the rate and direction of plume migration over time due to changes in the hydraulic gradients. However, overall the CBP method proved to be capable of tracking the evolution of the plume through to the end of the experiment. Actual dimensions of the plume cannot be

NW   SE

C   C'

—◎—	t=3d
—○—	t=11d
—▽—	t=17d
—△···	t=25d
—⊞·	t=34d
—●—	t=46d
····◆····	t=60d
—◆—	t=68d
—□···	t=74d
—▲—	t=82d
—●··	t=89d
—+·	t=99d
—▽—	t=106d
···■··	t=117d
—△—	t=128d
—●··	t=138d
—+—	t=146d
—▼··	t=173d

Voltage Ratios

Distance Along Profile (m)
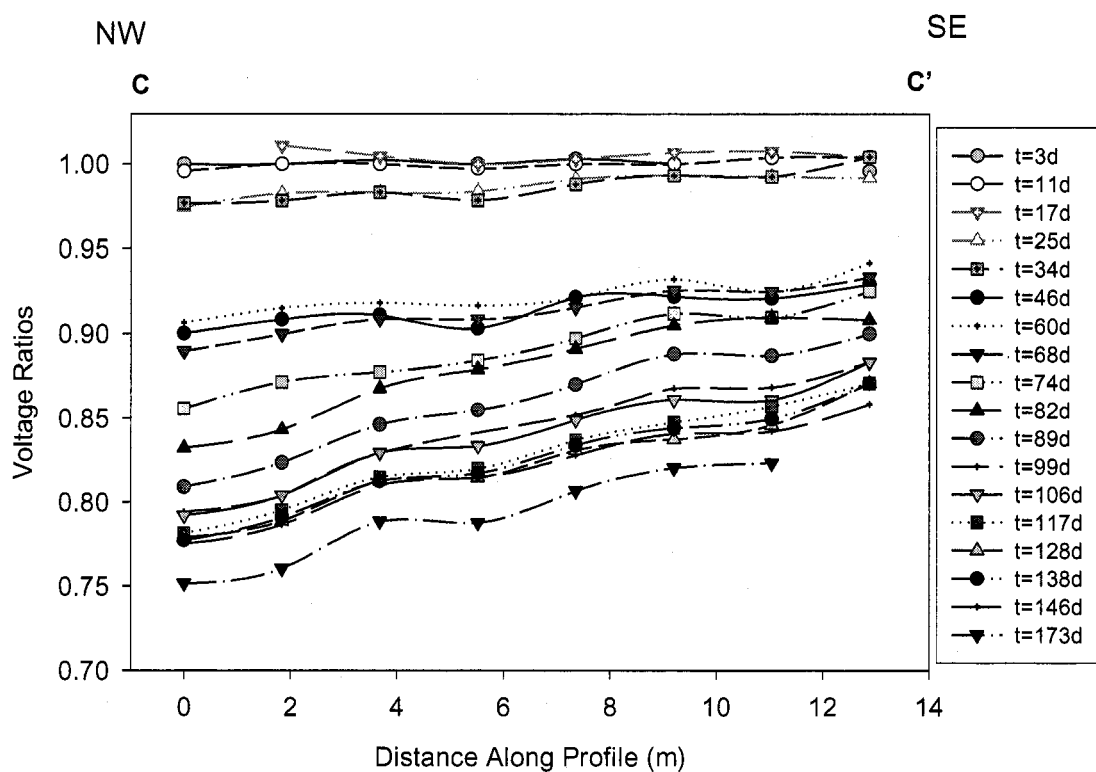
Figure 4.10. Northwest to southeast profile (C-C') of CBP voltage ratios ($V_{rat_{t_i}}$ values) along a diagonal of the grid of porous pot electrodes for all measurement periods (see Figure 4.6 for location of profiles).

determined based on the CBP measurements alone; however, certain details about the electrical potential distribution, for example, could be used effectively to guide the strategic placement of ground water monitoring wells and/or wells for remediation.

Acknowledgements

References

Archie, G.E., 1942. The electrical resistivity log as an aid in determining some reservoir characteristics. Am. Inst. Min. Metallurg. Pet. Eng. Tech. Paper 1422, 146-154.

Bevc, D. and Morrison, H.F., 1989. Borehole-to-surface electrical resistivity monitoring of a salt water injection experiment. Proceedings of the Society of Exploration Geophysicists 59th Annual International Exposition and Meeting, Oct. 29-Nov. 2, Dallas, TX, pp. 216-218.

Bevc, D., and Morrison, H.F., 1991. Borehole-to-surface electrical resistivity monitoring of a salt water injection experiment. Geophysics 56 (6), 769-777.

Binley, A., Daily, W., Ramirez, A., 1997. Detecting leaks from environmental barriers using electrical current imaging. Journal of Environmental and Engineering Geophysics 2 (1), 11-19.

Bush, J.H., and Seward, W.P., 1992. Geologic field guide to the Columbia River Basalt, Northern Idaho and Southeastern Washington. Idaho Geological Survey Information Circular 49, 35p.

Daily, W., Ramirez, A., LaBrecque, D., Barber, W., 1995. Electrical resistance tomography experiments at the Oregon Graduate Institute. Journal of Applied Geophysics 33 (4), 227-237.

Frangos, W., 1992. Electrical Detection of Leaks in Lined Waste Disposal Ponds. M.S. Thesis, Dept. of Geology and Geophysics, University of Utah, Salt Lake City, Utah, 78p.

Fried, J.J., 1975. Groundwater Pollution, Theory, Methodology, Modelling and Practical Rules. Elsevier, New York, 330p.

Hosterman, J.W., Schied, V.E., Allen, V.T., and Sohn, I.G., 1960. Clay Deposits in the Palouse Hills area, In Investigations of clay deposits in Washington and Idaho. USGS Bulletin 1091, 147p.

Keller, G.V., 1967. Supplementary guide to the literature on electrical properties of rocks and minerals. In Electrical Properties of Rocks, Monographs in Geoscience; Parkhomenko, E.I. Ed.; Plenum Press: New York, 265-314.

Keller, G.V., 1987. Rock and Mineral Properties. In Electromagnetic Methods in Applied
Geophysics - Theory, Volume 1, Society of Exploration Geophysicists, pp. 13-51.

Keller, G.V., and Frischnecht, F.C., 1966. Electrical methods in geophysical prospecting.
International Series of Monographs in Electromagnetic Waves, Vol. 10, Pergamon,
New York, 525p.

Nimmer, R.E., Osiensky, J.L., and Sprenke, K.F., 2001. Borehole-surface and cross-borehole
mise-à-la-masse delineation of a radial injection tracer experiment in partially
saturated fractured basalt. Proceedings of SAGEEP'01, Mar. 4-7, Denver, CO,
(BHL-2).

Nimmer, R.E., Osiensky, J.L., 2002. Direct current and self potential monitoring of an
evolving plume in partially saturated fractured rock. Journal of Hydrology 267,
258-272.

Osiensky, J.L., 1995. Time series electrical potential field measurements for early detection
of groundwater contamination. Journal of Environmental Science and Health A30
(7), 1601-1626.

Osiensky, J.L., and Donaldson, P.R., 1995. Electrical flow through an aquifer for
contaminant source leak detection and delineation of plume evolution. Journal of
Hydrology 169 (2), 243-263.

Osiensky, J.L., 1997. Ground water modeling of mise-à-la-masse delineation of
contaminated ground water plumes. Journal of Hydrology 197 (1), 146-165.

Parasnis, D.S., 1967. Three-dimensional electric mise-à-la-masse survey of an irregular lead-
zinc-copper deposit in central Sweden. Geophysical Prospecting 15 (3), 407-437.

Provant, A.P., 1995. Geology and Hydrogeology of The Viola and Moscow West
Quadrangles, Latah County, Idaho and Whitman County, Washington. M.S.
Thesis, University of Idaho, Moscow, ID, 116p.

Ramirez, A., Daily, W., Binley, A., LaBrecque, D., Roelant, D., 1996. Detection of leaks in
underground storage tanks. Journal of Environmental and Engineering Geophysics
1 (3), 189-203.

Sjostrom, K.J., and Sill, W.R., 1991. An electrical technique for the determination of ground
water flow parameters. Proceedings of SAGEEP'91, Mar. 11-14, Knoxville, TN.,
119-127.

Slater, L.D., Zaidman, M.D., Binley, A.M., West L.J., 1997. Electrical imaging of saline tracer migration for the investigation of unsaturated zone transport mechanisms. Hydrology and Earth Systems Sciences 1 (2), 291-302.

Slater, L.D., Binley, A.M., Daily, W., Johnson, R., 2000. Cross-hole electrical imaging of a controlled saline tracer injection. Journal of Applied Geophysics 44 (2-3), 85-102.

Street, G.J., Perry, A., and Greenham, L.J., 1993. Geophysical surveys of leaking tailings impoundments. Exploration Geophysics 24, 801-804.

Stierman, D.J., 1984. Electrical methods of detecting contaminated groundwater at the Stringfellow Waste Disposal Site, Riverside County, California. Environ. Geol. Water Sci. 6 (1), 11-20.

Suman, R.J., and Knight, R.J., 1997. Effects of pore structure and wettability on the electrical resistivity of partially saturated rocks – A network study. Geophysics 62 (4), 1151-1162.

White, P.A., 1988. Measurement of ground-water parameters using salt-water injection and surface resistivity. Ground Water 26 (2), 179-186.

White, P.A., 1994. Electrode arrays for measuring ground water flow direction and velocity. Geophysics 59 (2), 192-201.

CHAPTER 5. ELECTRICAL RESISTIVITY IMAGING OF CONDUCTIVE PLUME DILUTION[4]

[a]Robin E. Nimmer, [a]James L. Osiensky, [b]Andrew M. Binley, [a]Kenneth F. Sprenke and [c]Barbara C. Williams

[a]University of Idaho, Department of Geological Sciences, PO Box 443022, Moscow, ID 83844-3022, USA

[b]University of Lancaster, Bailrigg, Lancaster LA1 4YQ, United Kingdom

[c]University of Idaho, Department of Biological and Agricultural Engineering, PO Box 440904, Moscow, ID 83844-0904, USA

Abstract

Electrical resistance tomography (ERT) was used to monitor a conductive plume dilution experiment that was conducted in fractured basalt in order to assess its applications in this type of environment. Tap water was injected into an injection well for 34 days to dilute a pre-existing potassium chloride (KCl) plume. A 62-day monitoring period ensued, during which no fluids were introduced. Both surface ERT and cross-borehole ERT were used to monitor dilution and displacement of the plume. Surface ERT utilized a square grid of land-surface electrodes surrounding the injection well. 3-D images of surface ERT delineated areas of increased and decreased resistivities. Increasing resistivities are attributed to dilution/displacement of the KCl solution by tap-water invasion or the influx of seasonal recharge. Decreasing resistivities resulted from redistribution of residual KCl solution. Cross-borehole ERT was conducted between the injection well and each of seven surrounding observation wells. Polar plots of the injection-well resistivity data in the

---

[4]Submitted to the *HYDROGEOLOGY JOURNAL*.

direction of each observation well delineate specific locations where tap water seeped from the injection well via preferential flow paths determined by time-dependent resistivity increases. Observation well data show locations and clustered zones of resistivity changes as well as more discrete regions.

Keywords: fractures, basalt, tracer tests, electrical resistance tomography, plume.

5.1 Introduction

Fractured rock domains harbor contaminants in saturated and unsaturated zones in many areas of the world. Delineation of fracture zones is a crucial aspect of site and/or plume characterization, and ultimately is key to successful remediation efforts. Electrical geophysical methods have long been used in the mining and petroleum industries. As a relatively new method, electrical resistance tomography (ERT) has evolved into an important tool for site characterization at sites of ground-water and vadose-zone contamination. Specifically surface ERT, which provides a 3-D image, is important to environmental investigations due to the fact that all geological structures are three-dimensional; thus, a 3-D survey should provide more accurate, and more complete, images than 2-D surveys. 3-D characterization is particularly important for fractured rock characterization. The ERT methods provide cost-effective, supporting information for hydrogeological characterizations.

A field experiment consisting of two sequenced tracer injection tests was conducted in the vadose zone in fractured Columbia River Basalt. Figure 5.1a shows the site location and test plot layout of the experiment in Moscow, Idaho. The test was divided into three phases. Phase 1 was designed to saturate fractures in the vadose zone with potassium chloride (KCl) solution. The solution was expected to flow approximately radially away from the injection well through a number of mostly horizontal fractures of varying dimensions and degrees of connectivity. A conductive, fracture network with hydraulic and electrical continuity evolved over time. The Phase 1 state is referred to as "baseline" for the portion of the experiment described herein. Phase 2 was designed to test the suitability of various electrical methods to delineate spatial resistivity changes during *in situ* dilution of the

KCl plume by injection of tap water. Phase 3 was designed to measure resistivity variations in the fracture network during the post-injection monitoring period.
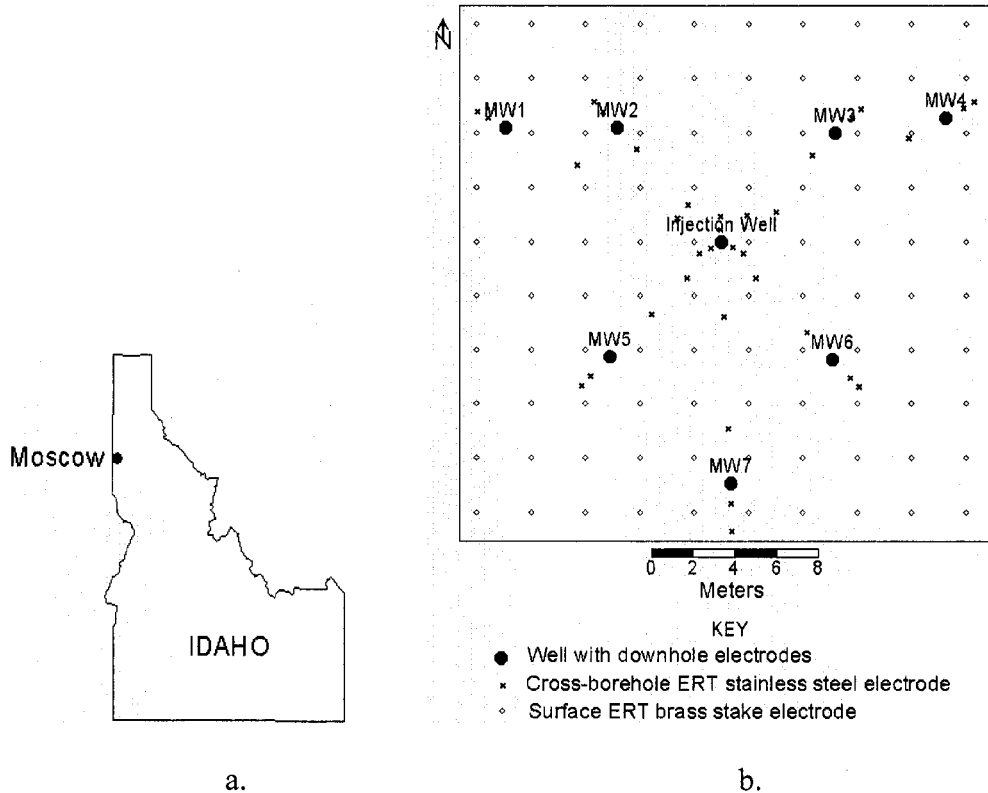
Figure 5.1. a) Geographical location map, b) Location of wells and surface electrodes.

Nimmer and Osiensky (2002a) presented results using hole-surface mise-à-la-masse (MALM) techniques for the first 34 days of Phase 1 of the experiment. Nimmer and Osiensky (2002b) described the use of SP, hole-surface MALM and cross-hole MALM during the entire experiment. They found that the MALM method proved to be capable of tracking the evolution of the plume through to the end of the experiment, though dilution by tap water showed little change. SP was affected by noise more than MALM and by itself did not provide enough information to delineate the tracer plume.

The ERT investigation described in this paper was designed to monitor changes in resistivity due to dilution and displacement of the KCl solution through the fractures during Phases 2 and 3 of the tracer experiment. Surface ERT was used to image resistivity changes three-dimensionally on a broad scale. Cross-borehole ERT between the injection well

containing the source material (i.e., tap water), and several nearby observation wells was used to provide information near the wells on the evolutionary plume dynamics.

5.2 Electrical techniques

5.2.1 Surface electrical resistance tomography

Surface ERT is a three-dimensional, electrical, imaging technique where the electrodes are located at land surface arranged in a rectangular grid. The method uses a two- to four-electrode array to measure a large number of resistances by applying sequences of exciting and recording potential differences to multiple electrode pairs within the electrode grid. These resistances are then inverted to generate a 3-D resistivity distribution. 3-D surface surveys are becoming more common due to the ready availability of multi-channel resistivity transmitter/receivers to collect the data, and faster computers to invert the data.

Surface ERT is also used for environmental applications. Industrial waste deposits and buried quarry geometry were imaged by Ogilvy et al. (1999) using surface ERT. Chambers et al. (1999) used the method successfully to image buried oil- and tar-contaminated waste deposits. Li and Oldenburg (1992) present results from an E-SCAN DC resistivity field experiment based on a pole-pole measurement scheme and an inversion algorithm for 3D problems. Park and Van (1991) described their inversion model and results from a large-scale, surface ERT experiment in unconsolidated materials involving the infiltration of water. Park (1998) attempted to improve the inversion model and results of Park and Van (1991). Dahlin et al. (2002) showed that a 3-D roll-along technique in addition to surface ERT with 3-D inversion was successful in delineating the original locations of four abandoned, low-resistivity sludge ponds.

5.2.2 Cross-Borehole electrical resistance tomography

Cross-borehole ERT provides images of the subsurface resistivity distribution in the intervening space between at least two wells. This method uses a four-electrode array to

measure a large number of resistances by applying sequences of exciting and recording potential differences to multiple electrode pairs, where most of the electrodes are located downhole. The resistance data are inverted to generate a cross-sectional resistivity distribution or tomogram. Electrodes are placed downhole and possibly also at land surface. This method has been used for over a decade in environmental investigations. Resolution of ERT is a function of electrode geometry, accuracy of the data, and measurement schemes, among other factors (Daily and Ramirez, 1995). Typical cross-borehole studies include leak detection (Daily et al., 1995a; Ramirez et al., 1996), fluid or contaminant migration (Daily et al., 1992; Daily et al. 1995b), remediation (by steam or air injection) monitoring (Ramirez et al., 1993; Daily and Ramirez, 1995; LaBrecque et al., 1996; Lundeguard and LaBrecque, 1995) and evaluation of engineered hydraulic barriers (Daily and Ramirez, 2000; Slater and Binley, 2003). More recently, research has been conducted in applying cross-borehole ERT results to determine tracer concentrations using a linear relationship (Kemna et al., 2002; Singa and Gorelick, 2005).

A relatively small number of cross-borehole ERT studies have been conducted in fractured rock. This method was used by Slater et al. (1997a) to image salinity change, and identify fracture zones in limestone. Slater et al. (1997b) examined unsaturated zone transport mechanisms through the use of cross-borehole ERT during an infiltration tracer test conducted in the vadose zone in chalk. Zaidman et al. (1999) used cross-borehole ERT in unsaturated chalk during a surface infiltration experiment to simulate the effects of heavy rainfall.

5.3 Local geology

The experiment was conducted at a vadose zone field site on the University of Idaho campus in Moscow, Idaho along the eastern edge of the Columbia River Plateau. The tests were completed in the uppermost basalt flow (i.e., the Lolo Flow of the Priest Rapids Member) of the Wanapum Formation, which dates to 14.5 million years ago (Bush and Seward, 1992). They describe a typical Columbia River Basalt flow to consist of (from top to bottom) a vesicular flow top, entablature, colonnade and pillows. However, Li (1990)

describes the structure of the Lolo flow having lateral variations. In addition, the typical, six-sided columns are not well formed.

The wells drilled for this investigation were completed near the basalt flow top, which is weathered, fractured and vesicular. A certain number of horizontal fracture zones may be laterally continuous for several meters; however, smaller fractures predominate. Vertical joints may connect the horizontal fractures. Clay, from weathering of the basalt, fills in some of the fractures.

The Lolo basalt flow is covered by about two meters (m) of alluvial sediments and Pleistocene Palouse loess (Provant, 1995) at the test site. The alluvial sediments consist of reworked loess with basalt and granite fragments. The loess is composed of a silty loam with predominantly quartz and feldspar in addition to small percentages of sand and clay. An approximately 0.5 m thick layer of silty clay forms the sediment-basalt contact at the research site.

5.4 Experimental method

5.4.1 Field-site logistics

Eight wells, each with a diameter of 15.2 cm (6 inches), were drilled by air-rotary (no water was added) to varying depths, with the distribution shown in Figure 5.1b. Prior to the KCl injection, the water table initially was located at the bottom of the deepest well, MW1 (774.75 m above mean sea level or 7.49 m below land surface). Figure 5.2 shows the lithologic heterogeneity at the site. "Weathered basalt" results from alteration by water flow through fractures. "Basalt" does contain some fractures. The observation wells penetrated various fractures containing perched ground water such that a few centimeters of standing water collected in the bottoms of all of the wells after drilling. The wells were cased with 15.2 cm-diameter PVC pipe through the sediments, and left as open hole within

Scale
(m amsl) Injection
Well

783
782
781
780
779
778
777
776
775

Injection Well   MW1   MW2   MW3   MW4   MW6   MW7   MW5

PVC pipe

Silt   Clayey silt   Weathered basalt   Basalt   Downhole ERT electrodes
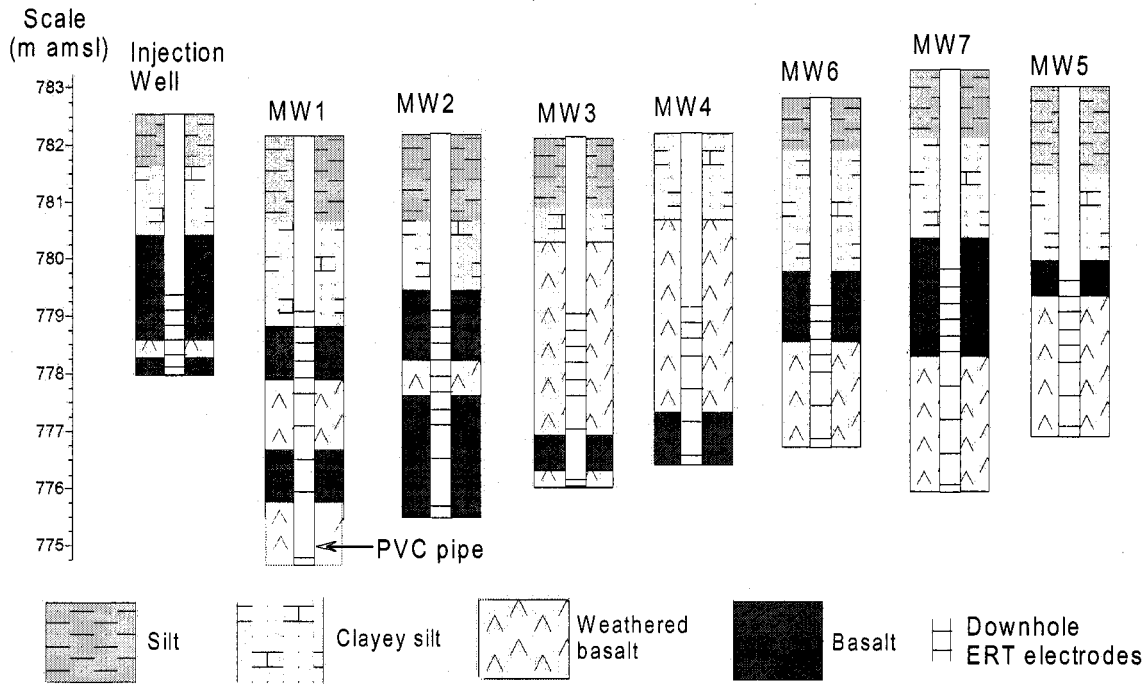
Figure 5.2. Well logs for observation wells and the injection well (modified from Nimmer and Osiensky, 2002a). Electrode locations are also shown.

the basalt. An inner PVC liner with a diameter of 5.1 cm was placed in each observation well; the bottom end of the pipe was left uncapped, and hacksaw slots were made in the bottom 10 cm to allow water to enter the pipe for water sampling. Copper, downhole electrodes were attached to the outside of each PVC liner. Each observation well annulus was filled with a 10 cm-long sand pack followed by dampened silt to the land surface to establish an electrical connection between the electrodes and the basalt medium. Electrodes in the injection well were attached to 1.3 cm diameter PVC plastic pipe and centered in the borehole. The soil around each well was mounded and covered with plastic sheeting to divert precipitation and surface runoff away from the backfilled annulus.

Surface and cross-borehole ERT were used to monitor changes in electrical resistivity within the well field over time. For cross-borehole ERT, the injection well was paired with each of seven observation wells, generating seven data sets per day of data collection. A pole-pole configuration was used for both methods. The reference electrode consisted of a porous pot, and the distant current electrode consisted of three stainless-steel stakes connected by a copper wire. These electrodes were placed 74.5 m to the west and 62.4 m to

the southwest of the injection well, respectively, due to land use constraints. The reason for the close proximity of the distant electrodes to one another was the intended placement of a north-south trending fence near the east side of the trailer to cordon off the field site from cows. The animals were relocated so the fence was not installed.

A uniform grid of 10 by 10 brass surface-stake electrodes was placed in the center of the well field for the surface ERT segment of the experiment. The electrodes were located 1.3 m apart and arranged as shown in Figure 5.1b. These electrodes were wired directly to a multi-electrode cable system attached to a transmitter/receiver system.

Sixty-six downhole copper electrodes and 34 surface stainless steel stakes were used in the cross-borehole ERT portion of the experiment (Figures 5.1b and 5.2). The downhole electrodes consisted of 14-gauge copper underground feeder cable wrapped around the each PVC liner to approximate point electrodes. The downhole electrodes were placed 10 cm from the bottom of each well and at 30 cm intervals to the top of basalt. Only 66 of the total 89-downhole electrodes were used due to the limited number of available circuit switches. The investigation originally was designed for hole-hole and hole-surface MALM experiments. After electrode placement, cross-borehole ERT was added to the investigation to help provide better vertical definition of potential flow paths. The surface stake electrodes were located along the plane between the injection well and each observation well, and were placed such that two electrodes were located on the outside (i.e. beyond) of each well and two were located between the wells for a total of 6 electrodes per array. These electrodes were spaced on multiples of 30 cm. The land-surface and downhole cross-borehole ERT electrodes were also wired directly to a multi-electrode cable system attached to a transmitter/receiver system.

5.4.2 Pretest conditions

Phase 1 of the experiment was represented by development of the initial conditions for Phase 2. Baseline electrical conductivity of the water in the bottom of the injection well prior to Phase 1 was 0.1153 S/m. Phase 1 (t= -76 d) began when the injection well was filled with 34.8 liters (l) of KCl solution with a constant electrical conductivity of 0.60 S/m from a heated polyethylene storage tank. The solution was heated to maintain a temperature of

83

approximately 10°C. A total of 765 l of solution was added to the injection well over the 76 days at an average rate of 10.07 l/d. A 1.91 m-long column of conductive fluid was maintained from the bottom of the well to the top of the basalt layer 2.67 m below land surface. A constant water level in the injection well was maintained at an elevation of 780 m above MSL through a drip system.

5.4.3 Test conditions

Phase 2 began at t=0 d when the KCl solution was pumped out of the injection well, and the well was refilled to the same elevation with tap water (electrical conductivity of 0.0294 S/m). A total of 221 liters of tap water was injected over 34 days thereby displacing and diluting some of the KCl solution in the fracture network. At t=34 d the tap-water injection ceased. Data collection continued for the next 62 days as Phase 3 of the investigation until t=96 d.

5.5 Conceptual model

During Phase 1 of the experiment an air-filled borehole in the vadose zone was filled with a KCl solution, and saturation of the fracture network began. Fluid was anticipated to flow out of the well approximately radially through larger fracture zones connected by a network of smaller features. It is likely that some of the fluid also drained from the bottom of the borehole. Clay resulting from weathering of the basalt may have reduced the hydraulic conductivity of some of the fractures. Over time a continuous fracture network was assumed to have been saturated with KCl solution. The injected tap water was exected to follow the same pathways.

5.6 Data acquisition and processing

Surface ERT resistances (*R*) measurements were collected infrequently due to the lengthy setup and take down time required as well as weather inhibitions. One data set was

collected during each of the experimental phases (i.e. three times). Because collection of complete, surface ERT data sets is very time consuming, an alternative measurement scheme was applied, called the "cross-diagonal survey" method. In this method the potential measurements are collected along the x and y-directions and along 45-degree diagonal lines from the current electrode. This reduces the total number of measurements by approximately $1/3$ (Loke and Barker, 1996). Current was injected at each of the brass surface electrodes, and resistances were measured at the electrodes in the x-direction, y-direction and along 45 degree diagonal lines crossing through each current electrode. This procedure kept the data collection time manageable. Each of the data sets consisted of 2940 measurements (including reciprocals), taking approximately 13 hours including setup and disassembly. The electrodes were installed and removed for each measurement cycle to preclude interference with other electrical methods of data collection (e.g. MALM and SP). Markers were placed at the locations of the electrodes to ease setup for each subsequent measurement period.

Resistances for cross-borehole ERT were measured eight times during Phases 2 and 3 of the experiment; however, only four data sets are presented herein. The first set of ERT measurements taken at t=4 d for all seven injection well-observation well pairs (I-M1 through I-M7) in sequence are considered to represent baseline conditions to allow evaluation of changes over time. Each complete data set of 2830 measurements (including reciprocals) was collected in approximately nine hours through a supervised, programmed switching system.

5.6.1 Resistivity determination

The resistivity (ρ) distributions were ascertained through a sequence of steps. Resistances were calculated from voltages for a four-electrode array. Data errors were filtered out and resistance ratios (R_{rat}) calculated. Resistance ratios were generated by:

$$R_{rat} = \frac{R_{t2}}{R_{t1}} * R_h$$

Eqn. 5.1

where: R_{t1} is the transfer resistance at time t$_1$, R_{t2} is the subsequent transfer resistance at time t$_2$ and R_h is the transfer resistance for the comparable homogeneous resistivity

distribution (100 Ωm) predicted by the forward model. This equation is based on the method described by Daily et al., (1995b). The RES3DMOD code (Loke, 2001) was used to generate the R_h values for the surface ERT data. A finite-element based DC resistivity forward model was used to generate the R_h values for the cross-borehole ERT data. The R_{rat} values were input into the inversion models, which generated resistivity values (ρ).

5.6.2 Data errors

Reciprocals were examined to quantiy the transfer resistance errors. In this experiment, only positive current electrodes and potential electrodes were switched. Reciprocals should provide the same transfer resistance value (Binley et al., 1995). Reciprocal errors were quantified (as a percentage) based on:

$$\%Error = \frac{|R - R_{recip}|}{R_{mean}} * 100$$

Eqn. 5.2

where: R is the resistance, R_{recip} is the reciprocal resistance and R_{mean} is the mean of the two resistances. Data with reciprocal errors greater than 5% were culled, and common data sets between the same well pairs were developed for comparison purposes. Table 5.1 lists measurement information for the inversion process for the cross-borehole data between the injection well and each observation well, and for the surface survey.

	MW1	MW2	MW3	MW4	MW5	MW6	MW7	Surface
Total number of measurements (includes reciprocals)	462	462	380	342	380	342	462	2940
% of measurements used	73	79	70	87	78	93	85	75

Table 5.1. Resistance measurements for inversions

5.6.3 Resistivity inversion

Two-dimensional, finite-element grids were developed for the forward models and inverse models for analysis of the cross-borehole ERT data. The grid for each I-MW (injection well – observation well) pair is somewhat unique due to the minor land slope variations, variable well depths, and different numbers of electrodes and electrode locations. Each grid consists of a subgrid, which extends from land surface to the bottom-most electrode. Figure 5.3 shows the subgid for well pair I-MW1. For this example, the elemental spacing in the x-direction is 0.3 m and the z-spacing (vertical) within the electrode portion of the subgrid is 0.15 m. Due to the gently sloping topography, the land surface elevation was calculated by averaging the elevations of each I-MW well pair. The spacing in the z-direction above the electrode portion of the subgrid to land surface is this separation distance divided by ten; each grid then has ten rows of elements above the upper-most electrode of
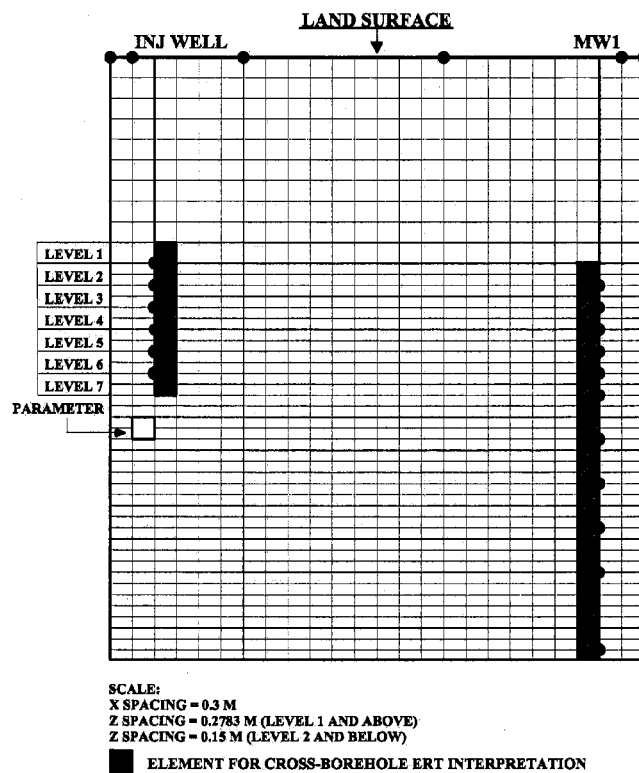
Figure 5.3. Subgrid for I-MW1, shown as an example (black circle represents electrode).

both wells. These spacings range from 0.2748 m for I-MW3 to 0.3096 m for I-MW6. Beyond the subgrid, cell sizes increase incrementally to a maximum cell size of 100 m to provide a grid space for placement of the remote electrodes and application of the boundary conditions.

The investigation originally was designed as a MALM and surface ERT experiment, but was later modified to include cross-borehole ERT to provide enhanced vertical resolution compared to cross-hole MALM. The electrode spacing was not ideal for cross-hole ERT, resulting in poor resistivity sensitivity between the wells; however, the inversion results give good vertical definition of resistivity changes at the wells. Consequently, only data near the electrode column are analyzed.

Two different inversion codes were used to invert the cross-borehole and surface ERT data. The surface data were inverted using the RES3DINV (Loke, 2001) code and included topographic corrections as well as the exact locations of the distant electrodes. A proprietary code (Binley, 2001) was used to invert the cross-borehole data. The proprietary inversion model attempts to reproduce the measured potential field by using a theoretical relationship based on Occam's approach of deGroot Hedlin and Constable (1990); RES3DINV uses this same method plus modifications described by Sasaki (1992). The area under investigation is parameterized based on the finite-element grids. The resistivity distribution is solved by the model using a minimization of the objective function:

$$\Phi(m) = \left[\mathbf{D} - \mathbf{F}(\mathbf{m})\right]^{T} \mathbf{W}^{-1} \left[\mathbf{D} - \mathbf{F}(\mathbf{m})\right] + \alpha m^{T} R m \qquad \text{Eqn 5.3}$$

where $m = \log_{e}\left(\rho^{-1}\right)$, $\mathbf{D}$ is the vector of measured resistance, $\mathbf{F}(\mathbf{m})$ contains the corresponding forward model resistances due to parameter $\mathbf{m}$, T is the matrix transfer, $\mathbf{W}$ is a vector of data variances used to weight individual measurements, R is a roughness matrix used to force smoothing of the resistivity distribution and to stabilize the inverse solution and α is a smoothing parameter. An iterative solution is reached when the data misfit is minimized to an acceptable level.

A poor aspect ratio (ratio of vertical electrode separation to well separation) existed for the cross-borehole ERT portion of this experiment causing a low sensitivity distribution in the center area between the injection well and each observation well. The signal sensitivity was greatest near the wells and at the surface electrode sites. Therefore, rather

than studying the entire resistivity image, only the near-well image values are examined. Injection well resistivity values are plotted at specific depth intervals as polar charts in the radial direction of each observation well from the injection well to evaluate the locations of potential fluid pathways (i.e. fracture zones) during tap-water injection. The measurements represent a distance of 0.224 m into the formation, calculated by subtracting the well radius from the grid element size. The polar plots show directional resistivities, which could not have been derived from single well experiments. Observation well resistivities are presented as graphs of resistivity (by grid-element elevation) versus time; resistivity values are taken from grid elements that border the inner subgrid side of the downhole electrodes (Figure 5.3). Interpretations are based on the assumption that changes in inverted resistivity values are due strictly to changes in pore-water resistivity or degree of saturation.

5.7 Hydrologic data analysis

Hydrologic data collected over the duration of the experiment at and near the field site provide information in support of the electrical data interpretation. Water levels were measured in each of the eight wells. Precipitation data in water equivalents for Moscow were provided by Qualls (2005).

Figure 5.4a shows the elevation of water levels in the wells, and daily amounts of precipitation. Water levels in the observation wells were fairly stable from the beginning of Phase 1 (t= -76 d) through at least t=4 d. Between t=4 and t=15 days (Phase 2) water levels began to rise in all the observation wells. This rise is believed to be caused by the infiltration of water from snowmelt and heavy rain. Precipitation events correlate rather well with increases in water levels in the wells. Water levels peak at approximately 66 days, but are not associated with a single, major precipitation event or a significant increase in the duration of precipitation. Coincidently, the tap-water injection phase of the experiment concluded shortly before water levels in MW5 and MW7 rose above the water level elevation in the injection well. It is important to note that water levels in the injection well remained fairly constant until approximately t=78 d. Electrical conductivity (EC) of the well waters was measured throughout the experiment (Figure 5.4b). EC of the ground water in the
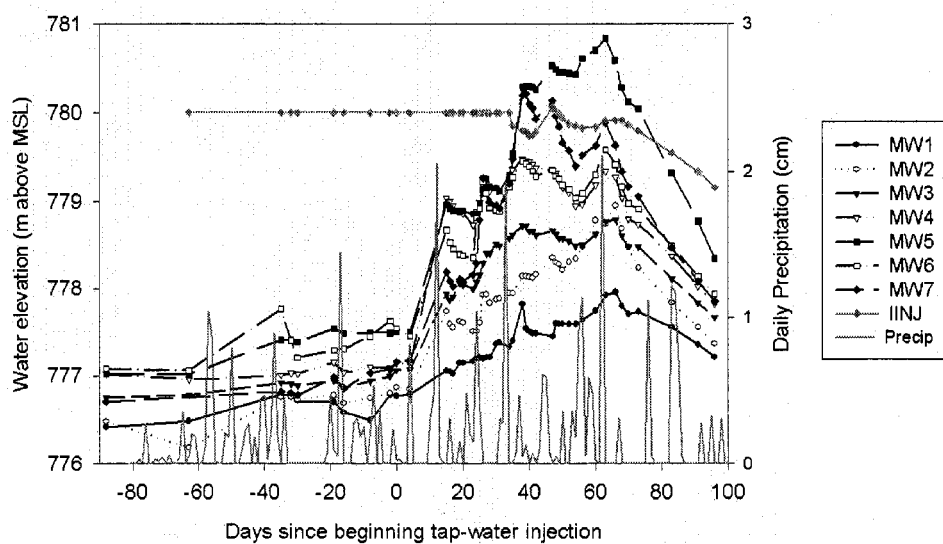
a
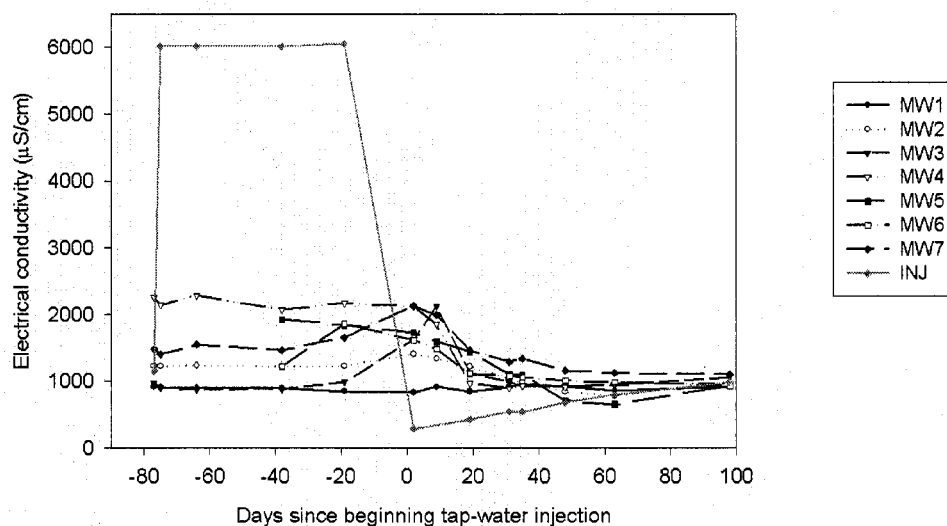
b

Figure 5.4. a) Graph of water elevation measurements in the wells and precipitation in water equivalents. b) Graph of electrical conductivity measurements of water in the wells. Day 0 represents the beginning of the tap-water injection.

observation wells began to increase following the injection of KCl solution, suggesting arrival of the plume. The EC then decreased prior to tap-water injection (Phase 2) or shortly thereafter. This probably was due to the recharge of lower conductivity water.

5.8 Surface ERT results and discussion

Surface ERT data were acquired on two occasions during this investigation. The first data set was collected at t=17 d (Phase 2). The second data set was collected at t=68 d (Phase 3).

To evaluate the resistivity changes caused by water conductivity and saturation changes, inverted ratioed values are examined. Figure 5.5 shows the resistivity values for [t=68 d / t=17 d] as images in map-view and cross-section view. Areas where the resistivities

a

b
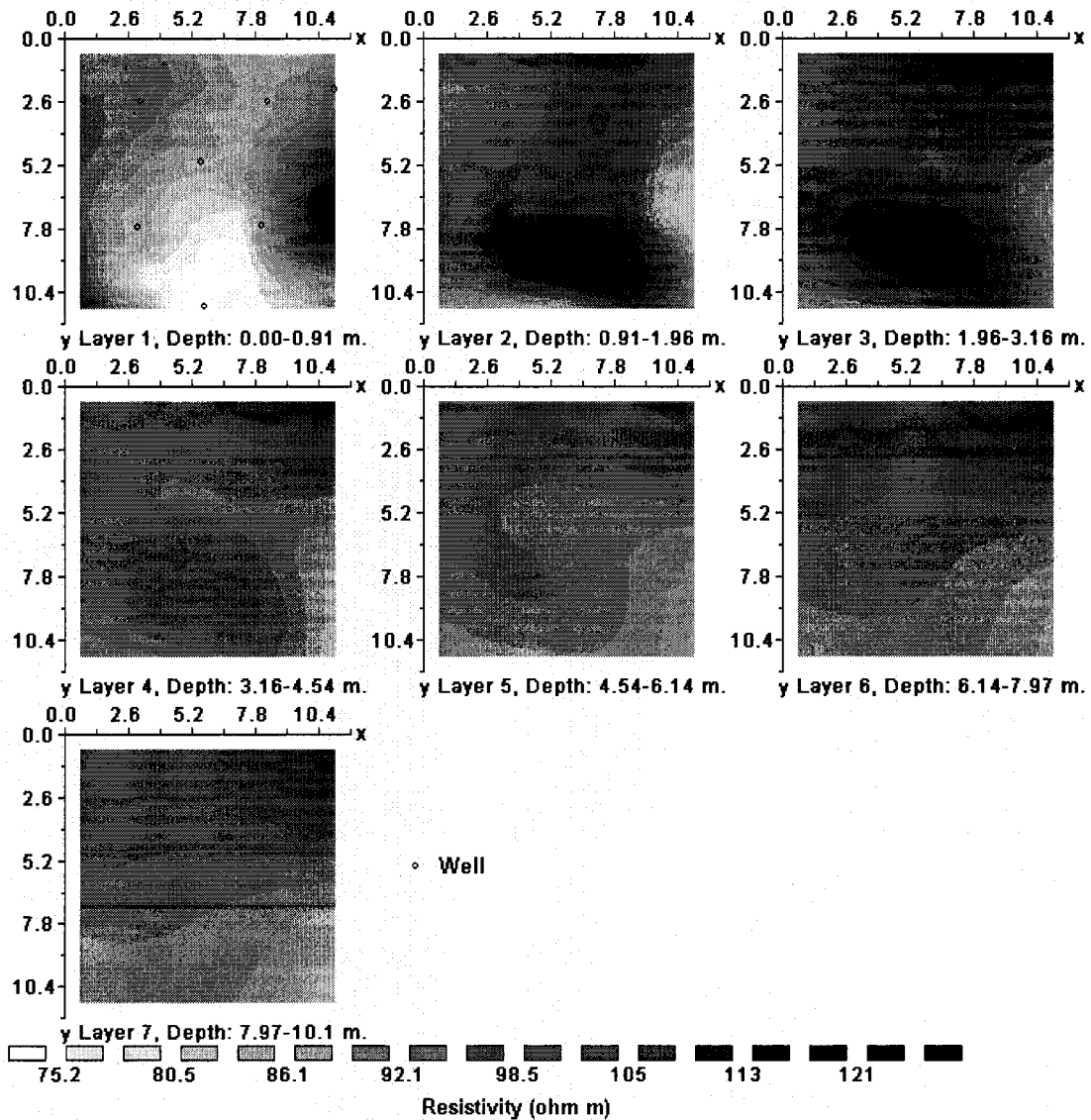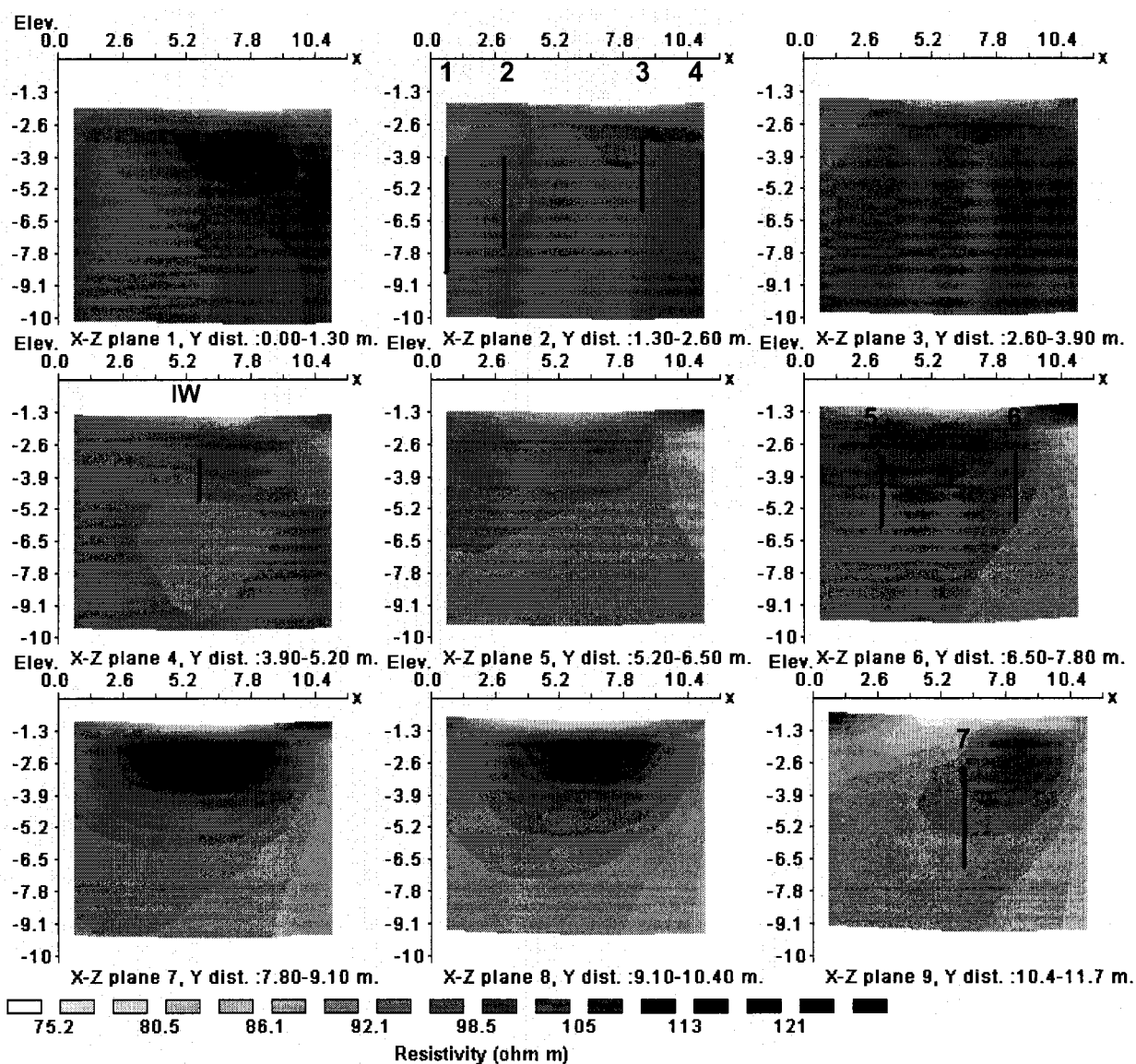
Figure 5.5. Surface ERT resistivity distributions for t=68 / t=17 d: a) map-view images (north is up), b) cross-sectional images from north to south. Lines on b) represent depths of electrode sections. When wells are located along the border of two cross-sections the electrode lines are located on the northern-most cross-section. See Figure 5.1 for well descriptions.

are greater than 100 Ωm indicate an increase in resistivity since t=17 d. Figure 5.5a shows the subsurface is heterogeneous over short distances based on the resistivity variations. Layer 1 has a low resistivity anomaly trending nearly north-south through the center of the electrode area with the lowest resistivities in the southern half of the anomaly, due to an

increase in saturation caused by the spring snow-melt and rains. Resistivities near 100 Ωm (no change) are shown in the area of the injection well in Layer 3 (bulk of the injection zone). As expected, resistivity changes are shown in areas outside the vicinity of the injection well; the high resistivity anomalies detected in Layers 2 and 3 at the northern and southern areas of the site likely reflect the influx of lower resistivity recharge water at these locations. Low resistivity anomalies in the deeper layers in the southeast quadrant of the site probably reflect redistributed residual KCl solution.

The cross-sectional images show a low resistivity discontinuity at a depth of approximately 1 m. This discontinuity is attributed to the aforementioned clay layer present at the top of the basalt within the test site. However, the clay layer appears to be discontinuous in the southern-most parts of the test site. These areas may provide more direct pathways of infiltrating recharge water. The resistivity distributions in the deeper layers suggest that higher resistivity water exists in the northeastern area of the site.

5.9 Cross-borehole ERT results and discussion

5.9.1 Injection well

Figure 5.6 depicts resistivities for grid elements along the axis of the injection well. These are presented in polar-plot form for Phase 2 of the cross-borehole ERT experiment; the values constitute changes from cross-borehole baseline (t=4 d) in directions toward the observation wells for t=15 d, t=26 d and t=34 d. Each spoke in the polar plots represents a line connecting the injection well and a different observation well. Inverted resistivity values are presented for seven levels in the injection well based on the model grid (Figure 5.3). Each level represents a 30-cm thick zone, except for Level 1, which is approximately 15-cm thick as explained earlier. A negative percent change depicted in Figure 5.6 indicates the area is more resistive than baseline. Figure 5.4b shows that the electrical conductivity of water in the injection well increased continuously during the injection phase, from 0.0294 μS/cm to 0.0542 μS/cm, most likely by desorption/diffusion of the residual KCl solution from the basalt matrix. The rate of tap-water movement out of the injection well was very slow (average rate of 6.5 l/d).
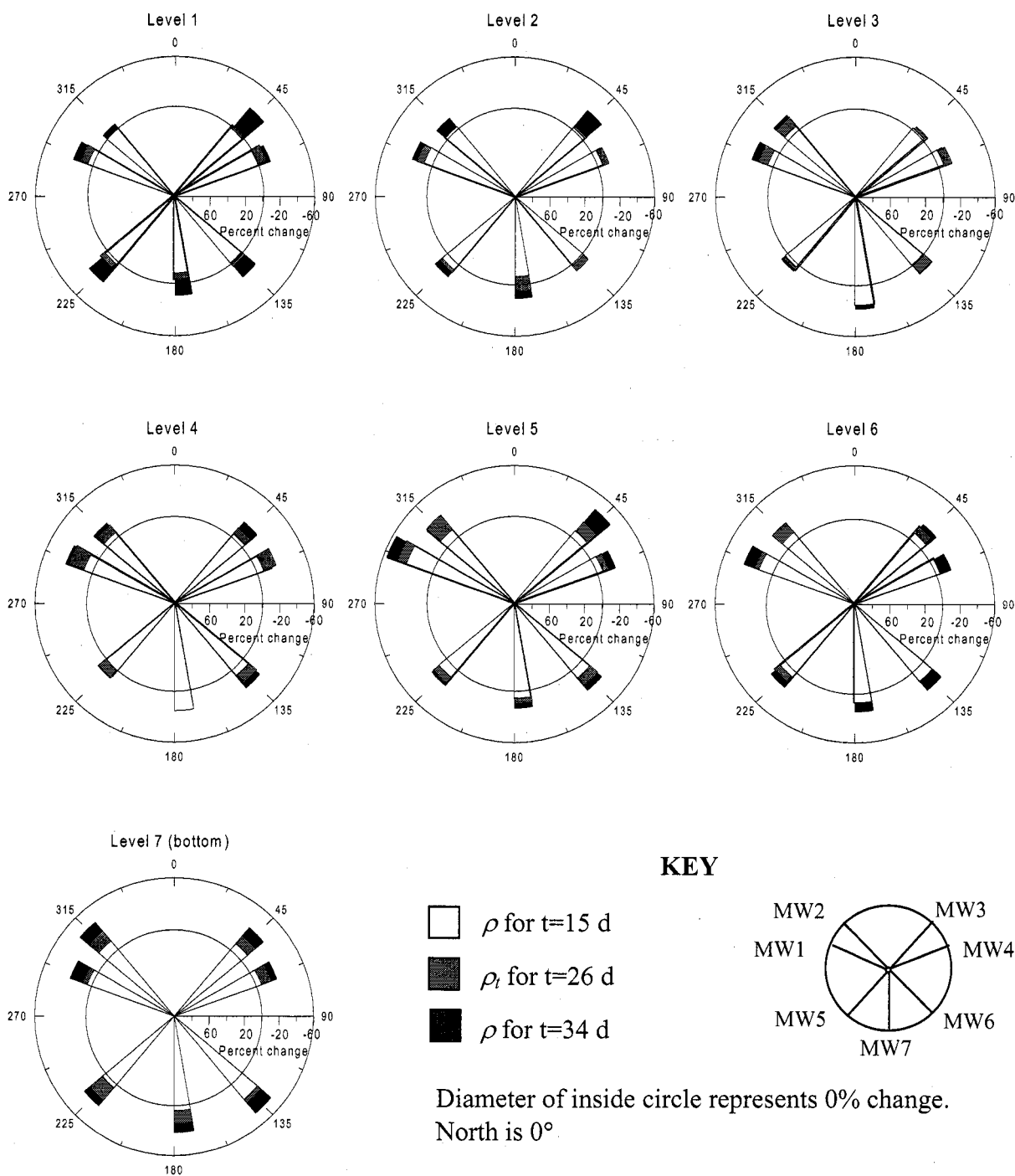
Figure 5.6. Polar plots of injection well resistivities as percent change from baseline for elements adjacent to the borehole within the subgrid region for the cross-borehole ERT experiments. A positive change is a reduction in resistivity; a negative change is an increase in resistivity. Level 1 and Level 7 are the uppermost level and bottommost levels, respectively. Each spoke represents resistivities for an observation well.

Figure 5.6 illustrates the heterogeneous nature of electrical resistivity changes in the fractured basalt. Locations adjacent to the injection well with significant increases in resistivity during the tap-water injection phase most likely indicate the presence of fluid transmitting fractures. Large, early-time, resistivity increases were detected in Levels 3 and 4 in the direction of MW7, Level 5 in the direction of MW1, and Level 7 in the direction of MW6. These resistivity increases most likely represent areas invaded by higher resistivity water. Late-time resistivity increases, such as those in Levels 1, 2, 4 and 5 in the direction of MW3, all of the Level 7 directions, and in Level 1 in the direction of MW5 may indicate sparsely fractured areas with predominately matrix flow. Locations where the resistivity values did not continue to increase significantly after t=15 d may represent zones flushed of KCl solution at an early time (i.e. Levels 3 and 4 in the direction of MW7). Decreased resistivity values detected at t=15 d in Levels 1 and 2 in the direction of MW7 are likely due to diffusion of KCl solution back into the injection well from dead-end fractures and pores.

5.9.2 Observation wells

Inverted observation well resistivity values for Phases 2 and 3 are shown in Figure 5.7 as line graphs of element elevation versus resistivity for four data sets. Examination of details about the resistivities, elemental tendencies of the data by time, and how the data are clustered provide insight into the changes in resistivity caused by the dilution and redistribution of the KCl plume.

The percent change of resistivities since baseline illustrate whether the resistivities have increased or decreased since baseline. Values approximating 0% change at early times represent areas of little change (e.g. MW2 and MW3). Resistivities with a positive percent change may be due to redistribution of the *in situ* KCl solution. Conversely, resistivities with a negative percent change indicate areas of shorter and/or faster flow paths, where dilution of the existing KCl solution is caused by mixing with tap water or recharge water. Areas where resistivities varied little with time (e.g. MW6 elevations 777.8 m and below) indicate points of stagnation within the system.

Specific locations (i.e. elevations) of resistivity changes over time within each well are delineated in Figure 5.7. Portions of the observation wells became more resistive while

MW1
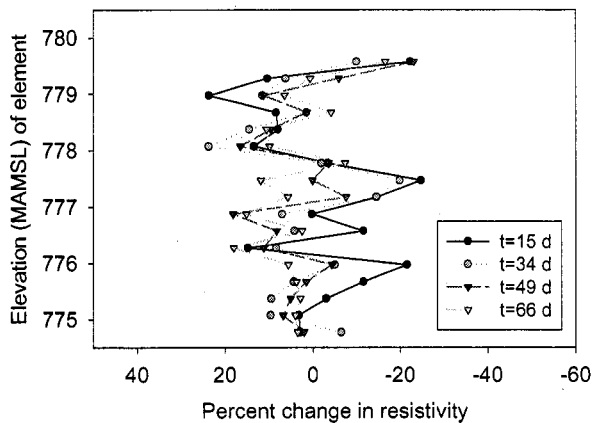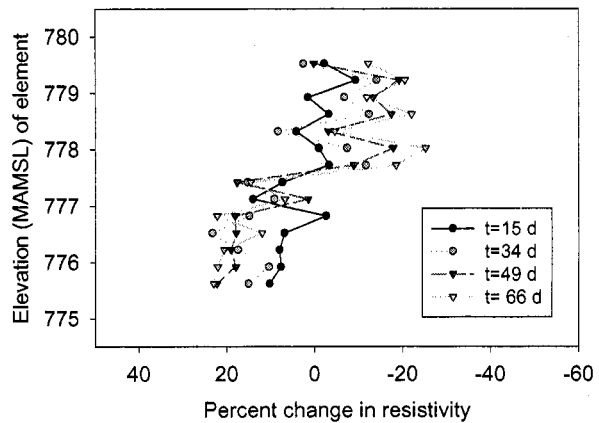
MW2
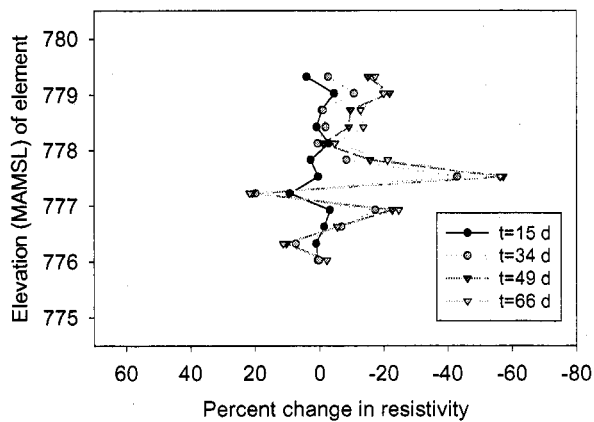
MW3
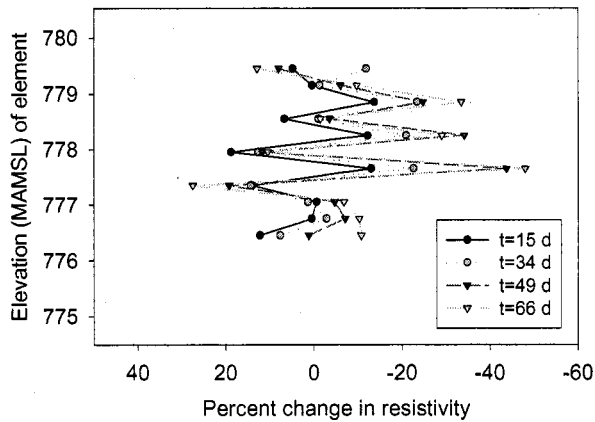
MW4
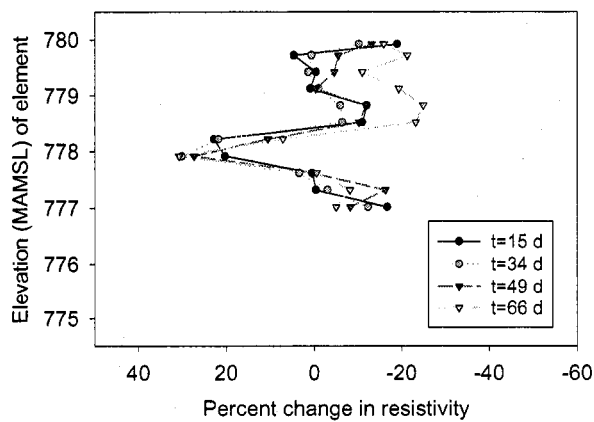
MW5
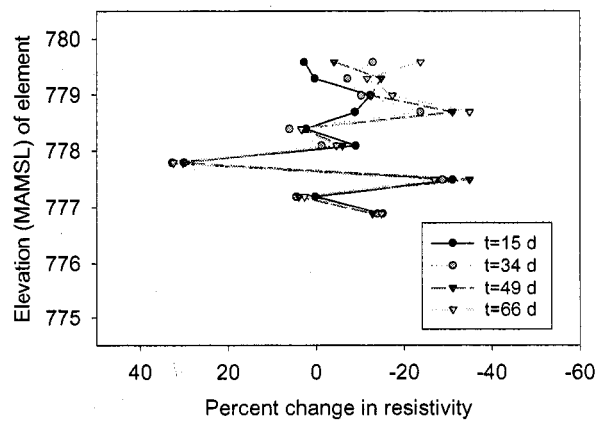
MW6
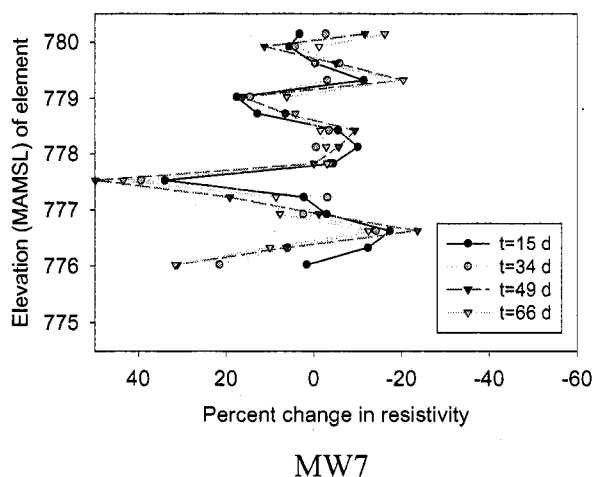
Figure 5.7. Graphs of observation well inverted resistivities as percent change in resistivity from baseline for elements adjacent to the borehole within the subgrid region for the cross-borehole experiments (see example locations in Figure 5.3). Phase 2 data are represented by circles; Phase 2 data are represented by upside-down triangles.

other portions became less resistive over time. Data that show similar increasing or decreasing tendencies may represent similar flow conditions (e.g. upper and lower portions of MW2). Zones showing increasing resistivities delineate dynamic pathways for resistive water movement. MW2, MW3, MW4 and MW5 contain significantly greater numbers of grid elements with increasing resistivity patterns compared to MW1, MW6 and MW7, findings that support the surface ERT data. At elevation 780.1 m in MW7, an increasing resistivity tendency began with a negative percent change; however, this elevation is 0.1 m above the constant head in the injection well, which strongly suggests that the increasing resistivity tendency was caused by factors other than tap water injection. Wells with increasing resistivities in the upper elevations, may indicate dilution by recharge from surface infiltration (i.e. upper halves of MW2, MW3 and MW5). The range of resistivity values at a single elevation does not span more than approximately 40 Ωm except for elevation 777.5 m in MW3 which increased nearly 80 Ωm, indicative of fracture flow and tap-water dilution. Zones showing decreasing resistivities delineate areas of relatively slow moving water; these areas reflect spatial redistribution of residual KCl solution over time. Zones showing decreasing resistivities tend to have more sporadic responses and are

generally deeper in succession. MW7 contains the lowest resistivities. Vacillating resistivities (e.g. MW6 elevation 777.8 m), and zones with alternating increasing and decreasing resistivities (e.g. bottom half of MW3) may reflect hydraulic gradient fluctuations shown in Figure 5.8. Zones with no definitive patterns correspond to the complex nature of the system.
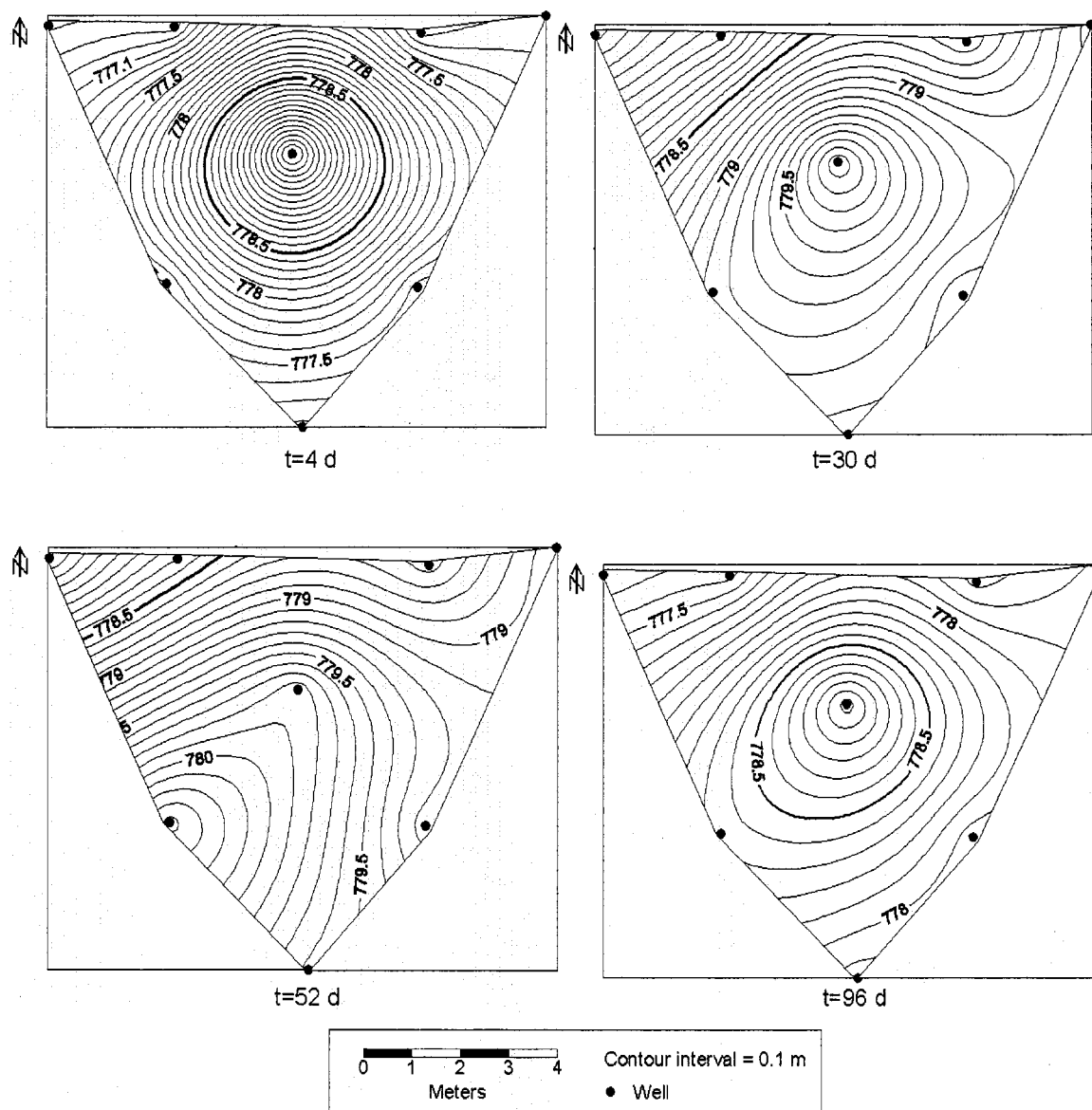
Figure 5.8. Ground-water elevation contour maps between wells at the research site. Elevations are in meters above MSL. Thick line represents the elevation contour line 778.5 m for reference purposes. See Figure 5.1 for well locations.

5.10 Summary and conclusions

Surface ERT imaged three-dimensional resistivity changes caused by dilution of the preexisting KCl plume on a broad scale during a tracer test in fractured basalt. Surface ERT provided very useful information on the changes in resistivity due to the general pattern of water movement during tap-water injection and seasonal recharge, and on the stratigraphy that influenced the water movement. However, this method is not capable of tracing the details of water movement at as small a scale as the cross-borehole data due to the decreased sensitivity with depth of the method.

Cross-borehole ERT between an injection well containing the source solution, and several nearby observation wells provided detailed information near the wells on the evolutionary plume dynamics during a tracer test in fractured basalt. Cross-borehole ERT resistivities near the injection well delineated specific locations over time where tap water exited the borehole reflecting fluid transmitting fractures or fracture zones. Cross-borehole ERT resistivities near the observation wells demarcate specific locations of resistivity change over time due to movement of different conductivity waters through fractures. Differentiation of high resistivities or resistivity tendencies over time caused by the influx of tap water or recharge water through analysis of the cross-borehole ERT data could not be achieved in most instances. Given the complexities of the experiment cross-borehole ERT provided a great deal of information stratigraphically that would have been homogenized in a strictly hydrologic method analysis. ERT data clearly show the heterogeneous migration patterns of the solutions and mechanisms of solute transport in fractured basalt.

Acknowledgements

References

Binley, A., Ramirez, A., and Daily, W., 1995. Regularized image reconstruction of noisy electrical resistance tomography data. In Process Tomography by Bech, M.S. et al (Eds), Proceedings of the 4th Workshop of the European Concerted Action on Process Tomography, Bergen, 6-8 April, 1995, 401-410.

Binley, A., 2001. Model inversion code.

Bush, J., and Seward, W.P., 1992. Geologic Field Guide to the Columbia River Basalt, northern Idaho and southeastern Washington. Idaho Geologic Survey Information Circular 49, 35p.

Chambers, J., Ogilvy, R., Meldrum, P., and Nissen, J., 1999. 3D resistivity imaging of buried oil- and tar-contaminated waste deposits. European Journal of Environmental and Engineering Geophysics 4, 3-15.

Dahlin, T., Bernstone, C., Loke, M.H., 2002. Case history: A 3-D resistivity investigation of a contaminated site in Lernacken, Sweeden. Geophysics 67 (6), 1692-1700.

Daily, W., Ramirez, A., LaBrecque, D., and Nitao, J., 1992. Electrical resistivity tomography of vadose water movement. Water Resources Research 28 (5), 1429-1442.

Daily, W., and Ramirez, A., 1995. Electrical resistance tomography during in-situ trichloroethylene remediation at the Savannah River Site. Journal of Applied Geophysics 33, 239-249.

Daily, W., Ramirez, A.L., LaBrecque, D., and Binley, A.M., 1995a. Detecting leaks in hydrocarbon storage tanks using electrical resistance tomography", UCRL-JC-120547; CONF-9511130-1, p. 14, Presented at Frontiers '95, San Luis Obispo, CA, Nov. 1995.

Daily, W., Ramirez, A., LaBrecque, D., and Barber, W., 1995b. Electrical resistance tomography experiments at the Oregon Graduate Institute. Journal of Applied Geophysics 33, 227-237.

Daily, W., and Ramirez, A.L., 2000. Electrical imaging of engineered hydraulic barriers. Geophysics 65 (1), 83-94.

deGroot Hedlin, C., and Constable, S., 1990. Occam's inversion to generate smooth, two-dimensional models from magnetotelluric data. Geophysics 55 (12), 1613-1624.

Kemna, A., Vanderborght, J., Kulessa, B., and Vereecken, H., 2002. Imaging and characterisation of subsurface solute transport using electrical resistivity tomography (ERT) and equivalent transport models. Journal of Hydrology, 267, 125-146.

LaBrecque, D.J., Ramirez, A.L., Daily, W.D., Binley, A.M., and Schima, S.A., 1996. ERT Monitoring of Environmental Remediation Processes, Measurement Science and Technology 7 (3), 375-383.

Li, T., 1990. Hydrogeologic characterization of a multiple aquifer fractured basalt system. PhD. Dissertation, University of Idaho, Moscow, Idaho.

Li, Y., and Oldenburg, D.W., 1992. Approximate inverse mapping in DC resistivity problems. Geophysics Journal International 109, 343-362.

Loke, M.H., and Barker, R.D., 1996. Lease squares inversion of apparent resistivity pseudosections by a quasi-Newton method. Geophysical Prospecting 44 (1), 131-152.

Loke, M.H., 2001. RES3DINV – 3D Resistivity and IP Inversion software.

Lundegard, P.D., LaBrecque, D., 1995. Air sparging in a sandy aquifer (Florence, Oregon, U.S.A.): Actual and apparent radius of influence. Journal of Contaminant Hydrology 19 (1), 1-27.

Nimmer, R.E., and Osiensky, J.L., 2002a. Using mise-à-la-masse to delineate the migration of a conductive tracer in partially saturated basalt. Environmental Geosciences 9 (2), 81-87.

Nimmer, R.E., and Osiensky, J.L., 2002b. Direct current and self potential monitoring of an evolving plume in partially saturated fractured rock. Journal of Hydrology 267 (3-4), 258-272.

Ogilvy, R., Meldrum, P., and Chambers, J., 1999. Imaging of industrial waste deposits and buried quarry geometry by 3-D resistivity tomography. European Journal of Environmental and Engineering Geophysics 3, 103-113.

Park, S.K., and Van, G.P., 1991. Inversion of pole-pole data for 3-D resistivity structure beneath arrays of electrodes. Geophysics 56 (7), 951-960.

Park, S. 1998. Fluid migration in the vadose zone from 3-D inversion of resistivity monitoring data. Geophysics 63 (1), 41-51.

Provant, A.P. 1995. Geology and Hydrogeology of the Viola and Moscow west quadrangles; Latah County, Idaho and Whitman County, Washington, [MS Thesis]: Moscow, Idaho, University of Idaho, 116p.

Qualls, R.J., 2005. Personal communication, Idaho State Climatologist.

Ramirez, A., Daily, W., LaBrecque, D., Owen, E., and Chesnut, D., 1993. Monitoring an underground steam injection process using electrical resistance tomography. Water Resources Research 29 (1), 73-87

Ramirez, A., Daily, W., Binley, A., LaBrecque D., and Roelant, D., 1996. Detection of leaks in underground storage tanks using electrical resistance methods. Journal of Environmental and Engineering Geophysics 1 (3), 189-203.

Sasaki, Y., 1992. Resolution of resistivity tomography inferred from numerical simulation. Geophysical Prospecting 40, 453-463.

Singa, K., and Gorelick, S.M., 2005. Saline tracer visualized with three-dimensional electrical resistivity tomography: Field-scale spatial moment analysis. Water Resources Research 41, W05023.

Skinner, D. and Heinson, G., 2004. A comparison of electrical and electromagnetic methods for the detection of hydraulic pathways in a fractured rock aquifer, Clare Valley, South Australia. Hydrogeology Journal 12, 576-590.

Slater, L.D., Binley, A., and Brown, D., 1997a. Electrical imaging of fractures using ground-water salinity change. Ground Water 35 (3), 436-442.

Slater, L., Zaidman, M.D., Binley, A.M., and West, L.J., 1997b. Electrical imaging of saline tracer migration for the investigation of unsaturated zone transport mechanisms. Hydrology and Earth System Sciences 1 (2), 291-302.

Slater, L., and Binley, A., 2003. Evaluation of permeable reactive barrier (PRB) integrity using electrical imaging methods. Geophysics 68 (3), 911-921.

Zaidman, M.D., Middleton, R.T., West L.J., and Binley, A.M., 1999. Geophysical investigation of unsaturated zone transport in the chalk in Yorkshire. Quarterly Journal of Engineering Geology 32, 185-198.

CHAPTER 6. THREE-DIMENSIONAL EFFECTS IN TWO-DIMENSIONAL, CROSS-BOREHOLE, ELECTRICAL IMAGING[5]

Robin E. Nimmer[a], James L. Osiensky[a] and Andrew M. Binley[b]

[a]Hydrology Program, Department of Geological Sciences, University of Idaho, PO Box 443022, Moscow, ID 83844-3022, USA

[b]Department of Environmental Science, Institute of Environmental and Natural Sciences, Lancaster University, Lancaster, LA1 4YQ, UK

Abstract

Cross-borehole, electrical resistance tomography (ERT) experiments utilize downhole electrodes, typically placed in a fluid-filled borehole or backfilled within the borehole to create electrical coupling with the host material. Commonly, the resistivity of the fill material is in contrast with the host material resistivity. In addition, the boreholes are three-dimensional, and inversion routines are typically two-dimensional causing artifacts in the form of "borehole inversion effects" to develop in the resulting resistivity images. Another 3-D effect resulting in inversion artifacts is a "shadow effect" caused by use of a 2-D code to invert data from a 3-D body located outside the image plane such as a contaminant plume. In both cases the inversion model misrepresents the spatial change in voltages as a corresponding spatial change in apparent resistivity. Borehole inversion effects and shadow effects result as the forward solver attempts to resolve the discrepancy in the voltages for numerous electrode pairs into a meaningful resistivity distribution.

Results of numerical modeling indicate that borehole inversion effects and shadow effects are affected by a variety of factors. Borehole inversion effects are shown to be related directly to the resistivity contrast between the borehole fill and the host medium, and to borehole diameter. These results are significant because borehole inversion effects may

---

mask or enhance a target heterogeneity. Shadow effects are shown to be related directly to the distance of the target heterogeneity out of the image plane to some limit beyond where the effects become insignificant.

Key words: electrical resistance tomography (ERT), borehole inversion effects, shadow effects, artifacts, resistivity, finite-element model

6.1 Introduction

6.1.1 Statement of the problem

Within the past fifteen years, much progress has been made in the development and application of cross-borehole electrical resistance tomography (ERT) to environmental problems. However, two common occurrences related to the collection and inversion of cross-borehole ERT data can lead to erroneous interpretations. Typically, a 2-D inversion code is used to estimate the subsurface resistivity distribution between two wells; however, in reality, current flow between the current and potential electrodes is 3-D. Use of a 2-D code where 3-D structures prevail (e.g. boreholes, contaminant plumes, etc.) may result in image artifacts caused by limitations of the 2-D forward solver. These image artifacts are called "3-D effects" for the purpose of this paper. Application of a 3-D inversion model with a 2-D slice through the image plane can reduce 3-D effects. The second ERT limitation is a weak sensitivity in the center volume between the columns of electrodes (boreholes). Even with the use of a 3-D inversion code, image resolution is poor in the center volume relative to the areas near the electrodes.

One type of 3-D effect results from the cylindrically shaped, discontinuities formed by boreholes (Osiensky, et al., 2004). In most cases, the only access to the subsurface for placement of electrodes is through boreholes. The 3-D nature of the borehole itself presents an issue when using a 2-D inversion model to interpret the data. Furthermore, electrodes generally must be positioned below the water table, in a backfilled portion of the borehole, or another form of coupling mechanism must be used (e.g. flexible tubular liners to press a string of electrodes against the borehole walls) to create reliable, electrical contact with the

host material. Often determination of the resistivity contrast between the borehole fill and host material is not as high a priority as maintaining good, reliable, electrical continuity with the borehole walls. In addition, the actual resistivity of the fill may not be known. Even with detailed knowledge of the electrical properties of the fill material, incorporation of this information into the inversion procedure would necessitate the use of a computationally demanding 3-D inversion routine. If the resistivity contrast of the fill, and the volume of the borehole are disregarded, the 2-D forward model within the inversion code generates spatial image artifacts as part of a numerical solution to a technically ill-defined problem. These "borehole inversion effects" may develop from a combination of factors including irregular current flow near an irregularly shaped borehole, cylindrical current flow through the borehole fill, heterogeneity of the borehole fill, poor electrical continuity between electrodes and borehole walls, and/or 3-D/2-D model treatment of boreholes as absent or as element shaped prisms.

Indurated rock, such as limestone, quartzite, lavas, granite or gneisses, may have resistivities as much as three orders of magnitude greater than nonindurated materials (Keller and Frischknecht, 1966; Telford, et al., 1990; Parkhomenko, 1967; Bear et al., 1993), thereby creating a significant resistivity contrast with the filled borehole. Consequently, 3-D effects should be of more concern in fractured rocks than in nonindurated sands, silts, clays and gravels.

Some researchers have identified borehole inversion effects in their cross-borehole ERT images. Daily and Ramirez (1995) conducted an ERT experiment to monitor *in situ* trichloroethylene (TCE) remediation by air sparging. Their tomograms revealed resistive sheaths around the boreholes. Bentonite drilling mud was interpreted to have seeped into the formation sands forming a conductive skin. Based on numerical modeling, they concluded that complex current flow conditions due to the presence of the bentonite mud caused the reconstruction algorithm to produce a resistive sheath artifact because the borehole conditions violated the 2-D restriction in the finite-element forward algorithm. Slater et al. (1997) used a 2-D code to invert ERT data collected during a conductive, tracer test in fractured limestone to delineate fractures. The downhole electrodes were located in water-filled boreholes. Some of the results from Slater et al. (1997) have been reinterpreted as artifacts resulting from borehole inversion effects. Figure 6.1 presents an image of the 2-D

inversion results from Slater, et al. (1997) where the large, high resistivity artifact in the center of the tomogram (between two boreholes) is now believed to be caused by borehole inversion effects (Slater, 2005).

Another type of 3-D effect results from the use of a 2-D code to invert ERT data for a target body with contrasting resistivity (e.g. contaminant plume), where the body is located outside the image plane. These "shadow effects" are artifacts generated by the 2-D model as a numerical solution to data derived for an incomplete 3-D problem (i.e., the effects of refraction of the electric field within the image plane from a heterogeneity located outside of the image plane), combined with the reduced resolution of the model at the center volume compared to areas near the electrodes. Vanderborght et al. (1995) noted this effect as causing the deviation of breakthrough curves between simulated and inverted data and found that the inverted images had more of a diffuse character.
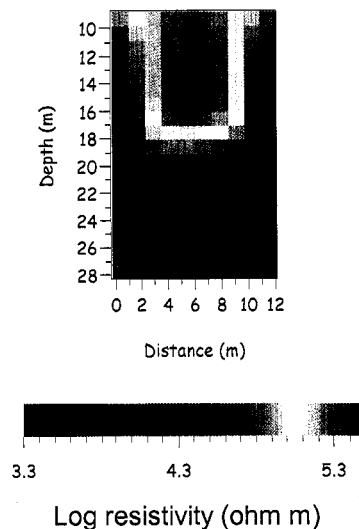
Figure 6.1. Resistivity image of borehole inversion effects (shown as relative resistivity high in red) modified from Slater et al. (1997).

6.1.2 Purpose of the experiment

The purpose of this paper is to evaluate the potential significance of ERT 3-D effects on potential tomogram misinterpretations specifically by examination of 1) borehole inversion effects, where the resistivity of the borehole fill contrasts with the host material,

and 2) shadow effects, where a 3-D heterogeneity is located outside of the image plane. The results presented herein have important ramifications relative to the application of ERT data to calibrate flow and transport models (e.g., Binley et al., 2002; Kemna et al., 2002; Vanderborght et al., 2005; Singha and Gorelick, 2005).

Synthetic data are created using a 3-D forward model. The data are then inverted using a 2-D code to generate a resistivity array along the image plane between two boreholes. Borehole inversion effects are evaluated by simulating two boreholes filled with material with contrasting resistivity relative to the host material; these conditions also are evaluated for different skip schedules. In addition, the significance of borehole diameter is demonstrated by incorporation of a buried, cubic-shaped, conductive heterogeneity (Target A) between the boreholes to illustrate how borehole inversion effects influence target image resolution. Shadow effects are evaluated by comparing the results of simulations with Target A centered and off-centered in the x-direction, and with Target B shifted out of the image plane in the y-direction (both targets have the same dimensions and same resistivity). While the 3-D effects evaluated in this paper are specific to the conditions modeled, the results should be applicable at the field scale.

6.2 Inversion artifacts

6.2.1 Borehole inversion effects

Voltage near a buried, single point source of current in an infinite, homogeneous medium is represented by (Telford, et al., 1990):

$$V = \left(\frac{I\rho}{4\pi}\right)\frac{1}{r}$$
Eqn 6.1

where: V is the voltage, ρ is the resistivity, r is the distance from the current electrode, and I is the current.

Current flow near a single, point-source of current embedded in a borehole filled with a conductive material generally is not spherical, and is dependent on the shape and depth of the borehole, and the conductivity contrast between the fill material and the geologic material forming the borehole walls (Osiensky, et al., 2004). Current flow near the electrode

generally is not spherical and no analytical solutions exist for this problem. Therefore, the analysis of borehole effects is performed through numerical modeling.

Two hypothetical borehole conditions were simulated numerically to illustrate equipotentials about a point source of current. Figure 6.2 presents two example cross-sectional-contour maps of voltages near a current electrode buried 1.5 m below land surface for a current of 0.5 amps. Case 1 shows the voltages about the current electrode in a homogeneous formation without the presence of a borehole. Case 2 is more realistic with the current electrode placed in a borehole with fill of contrasting resistivity relative to the formation. The borehole fill resistivity is 1 Ωm; the resistivity of the formation is 100 Ωm. These contour maps illustrate differences in current flow due to the presence of the partially penetrating borehole with two orders of magnitude contrast in resistivity. A point source of

a. Case 1

b. Case 2

c. Case 3
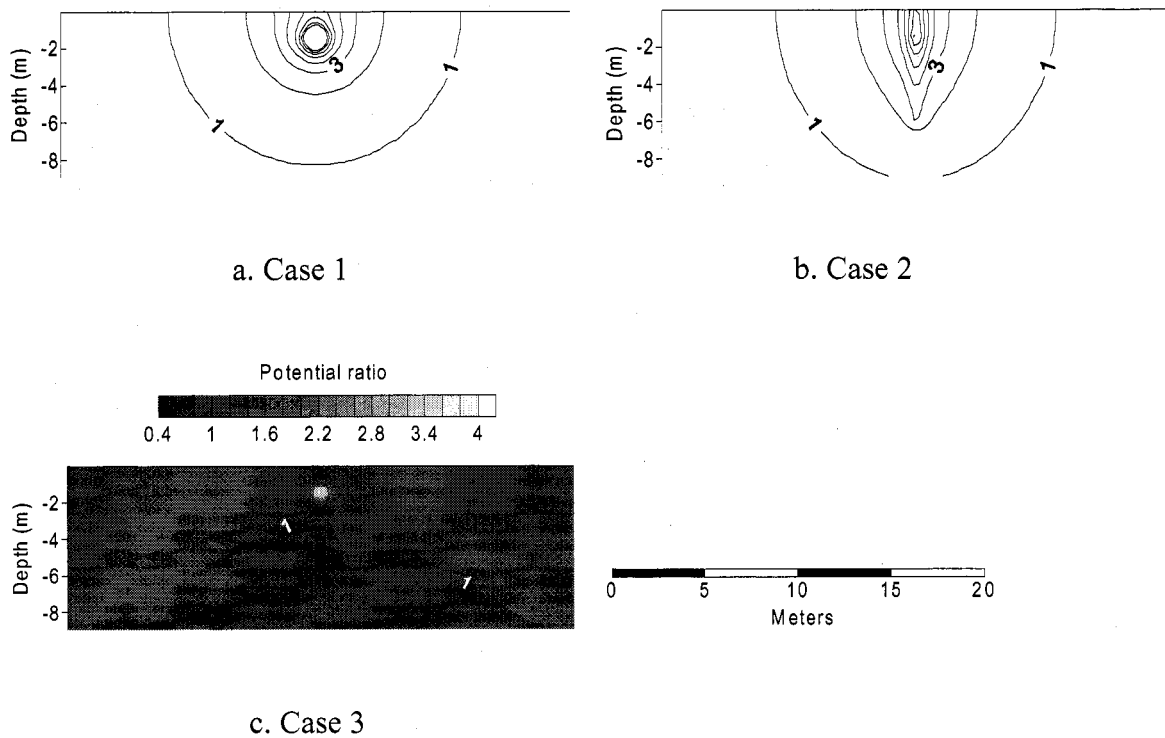
Figure 6.2. a) Case 1 - voltages (mV) for a buried current electrode without a borehole (100 Ωm). The current electrode is located at a depth of 1.5 m. b) Case 2 - voltages for a buried current electrode in a conductive borehole with a resistivity of 1 Ωm; boreholes are 6 m long. c) Case 3 - ratio Case 2/Case 1 depicting the spatial changes in apparent resistivity due to the presence of the borehole. Contour interval for a) and b) is 1 mV, and c) is 0.2.

current in a conductive, partially penetrating cylinder causes preferential flow in the borehole whereby the current density is decreased. Case 3 shows a contour map of voltage ratios (Case 2/Case 1) to depict spatial changes in apparent resistivity. Values greater than 1.0 indicate more resistive areas; values less than 1.0 indicate more conductive areas. It is obvious that the existence of the filled borehole for Case 2 changed the distribution of voltages about the current electrode compared to Case 1 without a borehole. Unless information about the borehole characteristics and borehole fill are provided as input data, the inversion model interprets spatial changes in voltages outside of the borehole as a spatial change in apparent resistivity, which of course is incorrect. Thus, borehole inversion effects result as the forward solver attempts to resolve the discrepancy in the voltages for numerous electrode pairs into meaningful changes in apparent resistivity.

6.2.2 Shadow effects

During the forward model simulations of a buried conductive heterogeneity without the presence of boreholes, the electric field is refracted relative to the homogeneous case. When the target is located outside of the 2-D image plane (e.g., as during cross-hole ERT between two boreholes), the resultant refractions in the electric field are misinterpreted by 2-D inversion algorithms as a body within the image plane. The inversion attempts to resolve the "cause" of the refraction without adequate information. The algorithm generates reasonable resistances (or apparent resistivities) for the refracted electric field to produce a resistivity array that includes "shadows" of the heterogeneity. Shima (1989 and 1992) suggests that the effect of anomalies lying outside the interest area can be reduced, and the uniqueness of the inversions can be improved by using a combination of measurements from along boreholes and cross-borehole. Shima (1989) also suggests examining a larger area to include outside the objective area for a more enhanced interpretation within the objective region. Sasaki (1992) recommends choosing a block discretization consistent with the resistivity ranges inside and outside the target region.

Refraction of the electric field occurs in the vicinity of heterogeneities with contrasting resistivity. When these heterogeneities lie outside, but near, the image plane, the effects of the refraction propagate through the image plane resulting in false changes in

apparent resistivity. Figure 6.3 presents a cross-sectional contour map of voltage ratios near a current electrode showing changes from a homogeneous resistivity distribution caused by a hypothetical target heterogeneity located completely out of the image plane (y=0) (target case/uniform case). The outer edge of the target (8 m^3 cubic heterogeneity) is located 3 m in front of the image plane; the geometric center is located at a depth of 1.5 m. The resistivity of the target is 1 Ωm, and the uniform background resistivity is 100 Ωm. The presence of the target caused refraction of the electric field. Both resistive and conductive changes are detected in the image plane with poor resolution of the actual target.

a.   b.
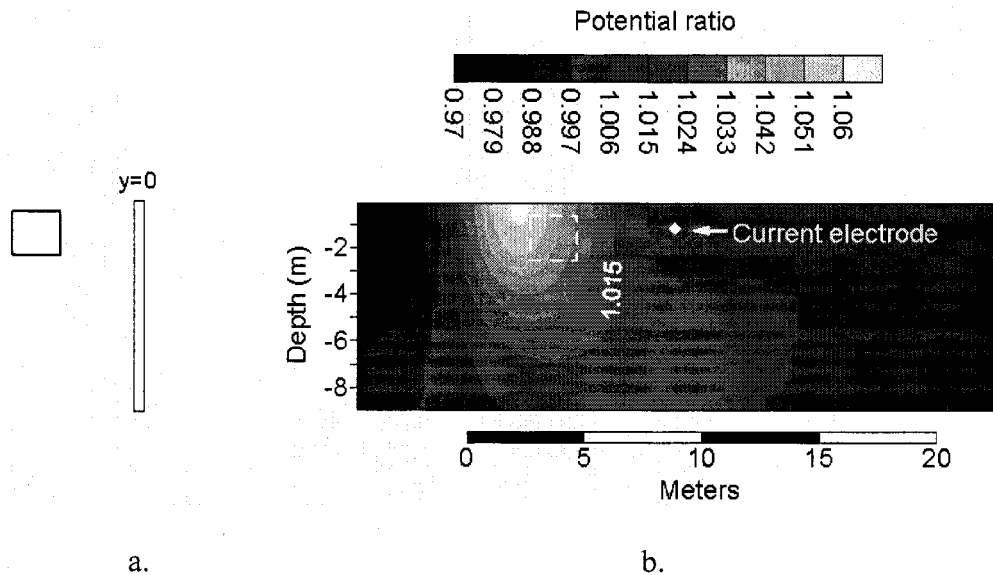
Figure 6.3. a) Orthogonal view of a target heterogeneity, side located 3 m in front of the image plane (y=0), b) Ratio of voltages (target case/uniform case) within the image plane (y=0) depicting the spatial changes in voltage caused by the addition of the target (represented by dashed box). Current = 0.5 amps.

6.3 Synthetic data models

In our synthetic ERT experiments, two boreholes are fitted with several electrodes to image the resistivity distribution in the volume between the boreholes. Forward and inverse finite-element models (FEM) are used to simulate field experiments containing possible borehole inversion effects and shadow effects. A 3-D forward model is used to simulate a

dipole-dipole array, and generate the transfer resistances (the voltage between an electrode pair divided by the current injected between another pair) based on the input resistivity values. The resistance values are used as input for a numerical, 2-D inversion model to generate a single resistivity distribution that best represents the measured data. Several simulations are performed to evaluate various borehole conditions, and positions of a single heterogeneity, on the inversion results.

6.3.1 Forward solution

The 3-D forward model utilizes a 61 x 45 x 47 rectangular, grid-centered, mesh with a four-electrode array. Element sizes in the x and y directions increase away from the centrally located boreholes. In the z-direction, element sizes increase with depth below the bottom of the boreholes. Model perimeter boundaries are non-conducting. It should be noted that the forward model discussed herein supplies resistances or apparent resistivities at the electrode locations; it is not the forward model within the inversion process.

Cross-borehole ERT experiments are conducted in boreholes, typically with a 0.1 m or greater diameter due to common drilling limitations, and to allow for multiple uses (e.g., monitoring, sampling, injection, etc.). The two boreholes for the modeled ERT experiments are simulated as prismatic heterogeneities, and not as actual cylinders; therefore, the results of the study are not geometrically exact. Boreholes with 0.1 m (~4 inch) diameters are simulated except where noted. Prisms composed of 2 x 2 x 30 cubic elements are used to simulate boreholes that are 15 m deep; the boreholes are 10 m apart and centered in the mesh. Figure 6.4 shows a cross-sectional view of a small portion of the forward model mesh in the borehole area. Prisms composed of 4 x 4 x 30 elements are used to simulate 0.2 m-diameter boreholes for comparison. Each borehole contains 16 electrodes on 1 m spacings located between land surface, z=0, and the bottom of the borehole, z=15 m.

A "skip-2" measurement schedule is applied in which two electrodes separate the current electrode pair (or potential electrode pair). This measurement schedule is used to increase the resolution further away from the borehole compared to an electrode pair with a smaller separation distance, while maintaining good resolution near the boreholes; in addition, this skip schedule improves the signal to noise ratio (Slater et al., 2000). A low-
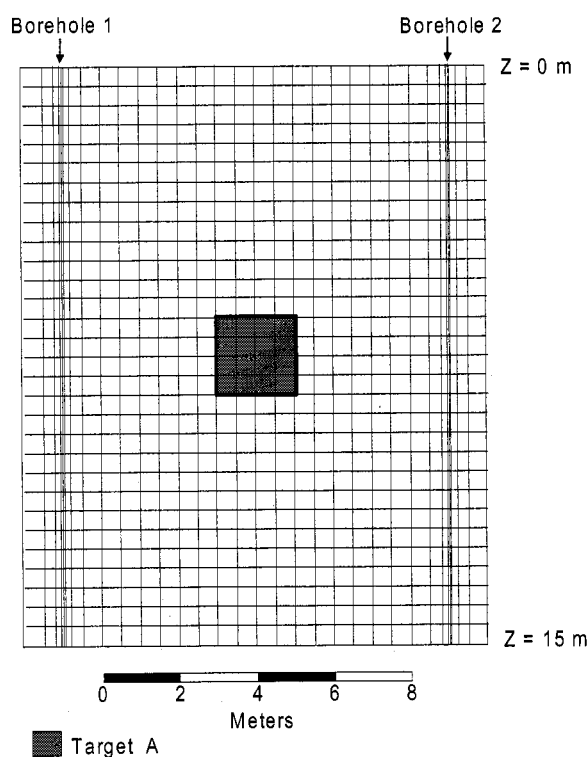
Figure 6.4. Cross-sectional view of a small portion of the forward model mesh showing the grid spacings near the two boreholes. The location of a single, 8 m^3 cubic heterogeneity (Target A) is shown between the boreholes. Boreholes are located 10 m apart. One electrode is located in each 1m thick layer in each borehole.

numbered skip schedule places the current (and potential) electrode pair in the same borehole and closer together; a larger-numbered skip schedule has the electrode pair split between two separate boreholes (i.e., one electrode in each borehole). Evaluation of different electrode configurations is described by Zhou and Greenhalgh (2000).

A baseline forward model was developed with a uniform resistivity of 100 Ωm. Two percent random noise was added to mimic field conditions. The transfer resistance output data were examined. Those with errors greater than ±2% were eliminated from all simulations prior to data inversion. These errors are a product of the model. Smoothing is unnecessary because the data are synthetic.

6.3.2 Numerical inversion

The inverse problem uses a different mesh than the forward model; the inversion model uses a node-centered, 2-D, quadrilateral mesh composed of 52 x 46 square elements (Figure 6.5). Outside the area shown in Figure 6.5 the elements increase in size away from the boreholes. The mesh is parameterized into resistivity blocks of four (2x2) elements. Each borehole location is defined by a column of 16 electrodes on 1-m spacings. The model weighting factors, a and b, are 0.001 and 0.01, respectively. These weighting factors control the degree to which the model smoothes the data.
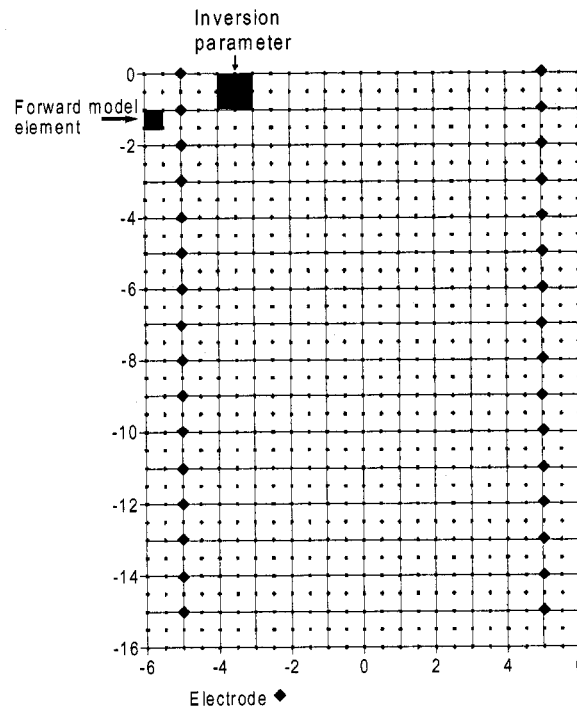
Figure 6.5. A small portion of the finite-element inversion model mesh and inversion parameterization in the borehole areas for the inversion process. Mesh extends beyond what is shown to reduce the effects of boundary conditions. Scales are in meters.

The inversion model attempts to reproduce the potential field by using a theoretical relationship based on Occam's approach of deGroot Hedlin and Constable (1990). The area

under investigation is parameterized using the finite-element mesh. The resistivity distribution is solved by the model using a minimization of the objective function:

$$\Phi(m) = \left[\mathbf{D} - \mathbf{F}(\mathbf{m})\right]^{T} \mathbf{W}^{-1} \left[\mathbf{D} - \mathbf{F}(\mathbf{m})\right] + \alpha m^{T} R m \qquad \text{Eqn 6.2}$$

where $m = \log_{e}\left(\rho^{-1}\right)$, ρ is the resistivity, $\mathbf{D}$ is the vector of measured resistance, $\mathbf{F}(\mathbf{m})$ contains the corresponding forward model resistances due to parameter $\mathbf{m}$, T is the matrix transfer, $\mathbf{W}$ is a vector of data variances used to weight individual measurements, R is a roughness matrix used to force smoothing of the resistivity distribution and to stabilize the inverse solution and α is a smoothing parameter. An iterative solution is reached when the objective function is minimized to a small value. .

6.4 Model simulations and results analysis

Selected conditions are simulated to evaluate potential 3-D borehole inversion effects and shadow effects in ERT experiments. Borehole inversion effects are examined by modeling several sets of conditions, each simulating ERT between two, 10.2-cm (4-inch) diameter boreholes. The first set of conditions has a one order of magnitude contrast between the borehole-fill material and the host formation. The next model simulates a borehole-fill material with two orders of magnitude contrast with the host formation. Two additional skip schedules are compared to analyze the optimal schedule using the previously modeled set of conditions. The borehole diameter is doubled to evaluate the potential significance of hole size on borehole inversion effects. A cubic heterogeneity (Target A) is introduced between the boreholes (see Figure 6.4 for location) to evaluate the significance of borehole inversion effects on the ERT image precision.

To study shadow effects, Target A, centered in the y-direction in previous simulations, is repositioned at distances of 1, 3 and 5 m away from the image plane in separate simulations and is renamed. In the x-direction, Target A is centered (x=4 to 6 m) and off-centered (x=2 to 4 m) in separate simulations. All tomograms are presented on log-resistivity scales, where a value of 2 represents the background resistivity. Not all the resultant tomograms of the model simulations presented share a common resistivity scale

because the purpose of this work is to illustrate characteristic artifacts and subtle differences that otherwise might be masked. Resistivity changes derived by the inversion model that do not represent actual changes in resistivity are called reconstruction artifacts.

The resolution of ERT is a function of many factors including data accuracy, electrode geometry, electrode sampling schemes, and other factors (Daily and Ramirez, 1995). Changes in the measurement scheme, number of electrodes, and the variables in the model itself (e.g. smoothing factors) lead to different solutions. Four grid elements comprise the smallest area that can be resolved by the inversion model developed for this investigation because a single parameter is 2x2. Although the model simulations represent simplified conditions, general characteristics of borehole inversion effects, and shadow effects are illustrated relative to tomograms typical of cross-borehole ERT field experiments. Borehole inversion effects often are included under the category of noise. Other forms of noise result from poor electrode coupling with the host rock, random errors associated with the transmitter/receiver, and errors caused by extraneous effects (Slater et al., 2000).

6.4.1 Borehole inversion effects

To benchmark the accuracy of the inversion model, uniform conditions of 100 Ωm were simulated, with satisfactory results. Model output as resistivity values ranged from 95.6 to 105.9 Ωm. This range in resistivity values is considered to be within acceptable limits, and is caused by minor errors in the forward and reverse algorithms.

6.4.1.1 Borehole fill.

Simulations of ERT between two boreholes with a borehole fill resistivity of 1 Ωm within a formation with a resistivity of 100 Ωm were performed. Figure 6.6a shows the image of a borehole fill/formation resistivity contrast $(BH\rho_{Contrast}) = 0.01$. Artifacts resulting from borehole inversion effects are evident as the highly resistive borders that frame the image, particularly the columns that parallel the boreholes and the conductive zone that is imaged between the boreholes. These artifacts result from preferential current flow up and down the borehole rather than directly into the formation, causing the inversion algorithm to

generate artifacts to account for the decrease in current density, and distortions in the electric field. There is no significant change from the uniform case when the $BH\rho_{Contrast} = 0.1$.

6.4.1.2 Skip schedule.

To ascertain the optimal skip schedule to use for the simulations, a range of skip schedules between skip-2 and skip-15 was tested. The test runs consisted of two, 0.1 m-diameter boreholes with $BH\rho_{Contrast} = 0.01$. Figures 6.6a, b and c are the resulting tomograms for skip-2, skip-5 and skip-15 schedules, respectively. The larger skip schedules exaggerate the borehole inversion effects near the center, supporting the use of the skip-2 schedule for the remainder of the model simulations. The larger skip schedules also result in lower sensitivity near the boreholes where the primary resistivity contrast occurs. It is important to note that the artifacts or noise cannot be eliminated by the selection of the skip schedule. The skip schedule must be carefully selected by also weighing target identification; Zong and Greenhalgh (2000) showed for dipole-dipole measurements that targets between boreholes are better defined with the current (and potential) electrodes placed in different boreholes (i.e. large skip schedule).
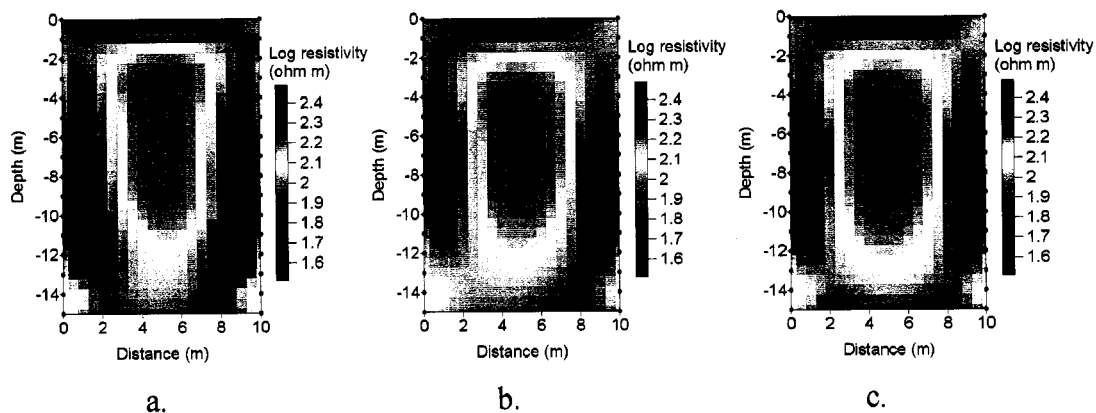
Figure 6.6. Tomograms of borehole effects of two, 0.1-m diameter boreholes with a $BH\rho_{Contrast} = 0.01$: a) skip-2 schedule, b) skip-5 schedule, c) skip-15 schedule. Electrode locations are shown as solid circles. No target heterogeneity exists between the boreholes for these simulations.

6.4.1.3 Borehole diameter.

Two, 0.2 m-diameter boreholes with contrasting fill resistivities were simulated to illustrate the significance of borehole diameter on borehole inversion effects. Each borehole is four elements wide in the x- and y-directions. This required a slight modification to the model grid used to simulate 0.1m diameter boreholes. The larger borehole diameter results in decreased current density compared to the 0.1 m boreholes, and this causes greater inversion process errors. Consequently, the weighting factor, 'a', in the inversion model was increased to 0.005 to reduce the amount of noise fitted; weighting factor 'b' remained the same as for the 0.1 m-diameter borehole simulations. These data were filtered based on the associated uniform model using the same criteria as the 0.1m-diameter borehole grid.

Two models were run with 0.2 m diameter boreholes and a skip-2 schedule. The first model used $BH\rho_{Contrast} = 0.1$ and the second model used $BH\rho_{Contrast} = 0.01$. Figure 6.7a shows the results for $BH\rho_{Contrast} = 0.1$. Figure 6.7b shows the results for $BH\rho_{Contrast} = 0.01$. Comparison of Figures 6.6a with Figures 6.7b that increasing the borehole diameter causes the resistive artifacts to intensify due to the decrease in current density. The resistivity patterns between Figures 6.7a and b are similar because the geometry of current flow is similar for both scenarios. Inaccuracies created by the 2-D forward solver during the
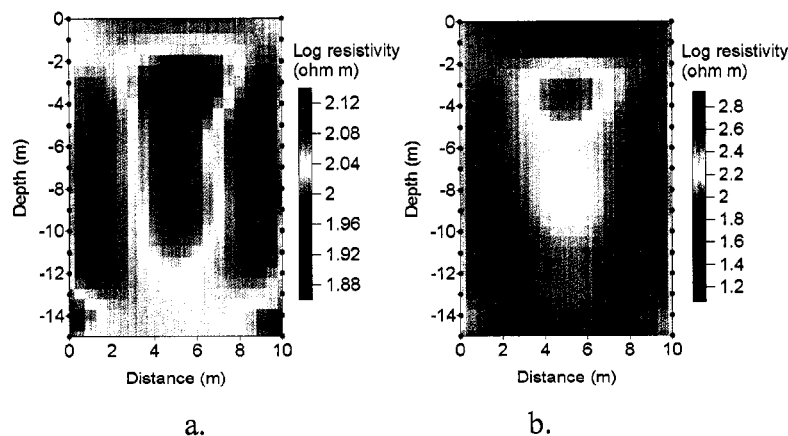
Figure 6.7. Tomograms of borehole effects with two, 0.2-m diameter boreholes with a) $BH\rho_{Contrast} = 0.1$ and b) $BH\rho_{Contrast} = 0.01$. (Note that the log resistivity scales differ from that in Figure 6.6). No target heterogeneity exists between the boreholes for these simulations. Skip-2 schedule was used for both simulations.

inversion process are greater for the larger diameter boreholes, resulting in greater borehole effects.

6.4.2 Borehole inversion effects plus heterogeneity

An 8 m^3 cubic heterogeneity is modeled initially in a homogeneous medium without boreholes, and then again with boreholes of contrasting resistivities in order to evaluate interferences by borehole inversion effects. Figure 6.8 shows the locations of the four named Targets. Target A_c is centered in the x-direction; Target A_{nc} is non-centered in the x-direction. The resistivity contrast of the target will be referred to hereinafter as $T\rho_{Contrast}$ (the ratio of the target resistivity/formation resistivity); $T\rho_{Contrast} = 0.01$ for these model simulations (target resistivity of 1 Ωm within a formation of resistivity 100 Ωm).
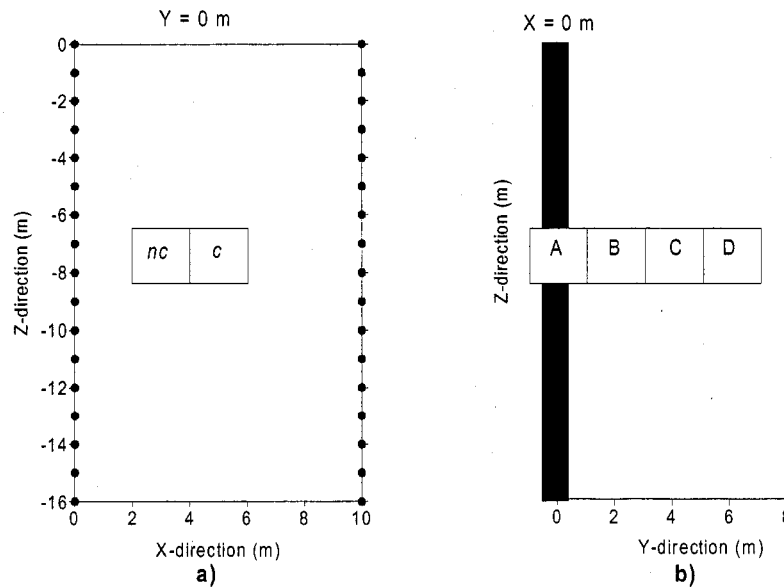
Figure 6.8. Diagram showing 8 m^3 Target locations (circles represent electrodes). a) y=0 m plane, subscripts *nc* represents a target that is not centered and subscript *c* represents a target that is centered. b) x=0 plane; Targets B, C and D are used in shadow effect simulations.

6.4.2.1 Centered target. (Target A_c)

Figure 6.9a is a tomogram showing the resolution of Target A_c with $T\rho_{Contrast} = 0.01$

within a uniform formation without boreholes (i.e., $BH\rho_{Contrast} = 1.0$). Target A_c is imaged as

a resistivity low. However, everything outside of the obvious target image is generated due

to noise added by the inversion routine or as reconstruction artifacts of the algorithm caused

by the resistivity low. The large size of the anomaly relative to the actual target body, and

the high magnitude of the inverted resistivity relative to the true target resistivity may be

explained by a combination of the 2-D approximation of a 3-D structure, use of a low-

numbered skip schedule which is better suited for near-borehole analysis, the smoothness-

constraint, or noise added by the inversion routine.

Two additional model runs were completed to simulate Target A_c between two

conductive boreholes. Figure 6.9b shows the resultant images for $BH\rho_{Contrast} = 0.10$ and

$T\rho_{Contrast} = 0.01$. Target A_c is detected at the correct location as a resistivity low. However,

by increasing the $BH\rho_{Contrast}$ by one order of magnitude to 0.01, the image in Figure 6.9c

becomes dominated by borehole inversion effects. This implies that greater borehole

inversion effects lead to better definition of the inverted target resistivity in some cases.

Table 6.1 lists the arithmetic-mean resistivity values (of four center-most elements) derived

by the inversion model at the location of the geometric center of Target A_c for various

a.   b.   c.
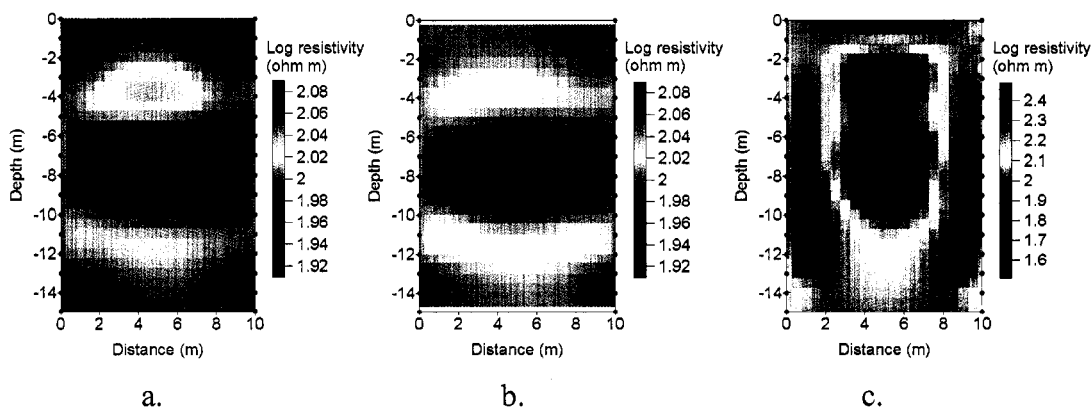
Figure 6.9. Tomograms of a centered 8 m^3 cube (represented by box), Target A_c, with
$T\rho_{Contrast} = 0.01$: a) no boreholes, b) two boreholes with $BH\rho_{Contrast} = 0.1$ and c)
two boreholes with $BH\rho_{Contrast} = 0.01$.

modeled scenarios. Based on the images in Figure 6.9 and data from Table 6.1, the following observations are noteworthy: 1) $BH\rho_{Contrast} = 0.01$ causes the inverted resistivity at the geometric center of Target A_c, and the target size to be reproduced more accurately than without borehole inversion effects, 2) $BH\rho_{Contrast} = 0.10$ improves the resolution of Target A_c inverted resistivity, and target location is reproduced accurately; however, target size is overestimated significantly for the reasons described above.

	Target name	Arithmetic-mean resistivity (Ωm) at geometric center of target within y=0 plane	
		Centered	Non-centered
No BH	None	81.87	74.41
BH$\rho_{Contrast}$=0.10	Target A	87.08	77.09
BH$\rho_{Contrast}$=0.01	Target A	46.92	65.85
BH Ratioed	Target A	90.06	NA
Shadow: out 1 m	Target B	89.17	87.61
Shadow: out 3 m	Target C	97.38	99.97

NA = not applicable

Table 6.1. Comparison of arithmetic mean, resistivity values derived by the inversion model at the geometric center of the target for several scenarios for Target A (centered at y=0 m), Target B (centered at y=2 m) and Target C (centered at y=4 m). $T\rho_{Contrast} = 0.01$ for all simulations.

6.4.2.2 Non-centered target (Target A$_{nc}$)

To evaluate resolution for targets not exactly centered between two columns of electrodes, Target A$_{nc}$ with $T\rho_{Contrast} = 0.01$ is offset 2 m (see Figure 6.8a for location). Figure 6.10a shows the inverted resistivity distribution for Target A$_{nc}$ in an otherwise uniform formation without the presence of boreholes. The resistivity low more accurately represents the true resistivity compared to the centered target due to a better sensitivity near the electrodes, yet the lowest resistivity is shifted 1.25 m to the left of the target's geometric center. Figure 6.10b shows the inversion model results for the target between two boreholes

with $BH\rho_{Contrast} = 0.01$. Target dimensions are better represented by the size of the anomaly compared to the results ffor Target A_{nc} without the presence of boreholes. Borehole inversion effects cause the resistivity low to be shifted 1.75 m to the right in the x-direction from the position of Target A_{nc} by overwhelming the influence of the target. These simulations demonstrate borehole inversion effects could have significant positive ramifications relative to target definition in some instances; however, misinterpretations relative to interpretation of target details are also possible.

a.   b.
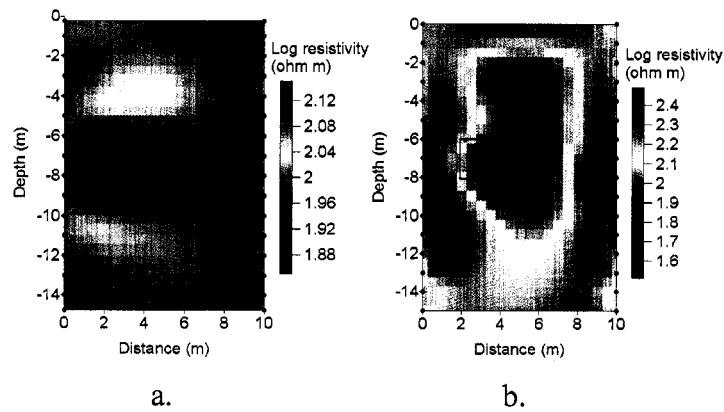
Figure 6.10. Images of a non-centered, 8 m³ cube (represented by box) (Target A_{nc}): a) two columns of electrodes without boreholes, and b) columns of electrodes in two boreholes with $BH\rho_{Contrast} = 0.01$.

6.4.3 Reduction of borehole inversion effects

Reduction of borehole inversion effects is crucial for ERT experiments when the shape and character of the target is not known a priori. Where the collection of time sequenced data is possible, analysis of ERT field data as inverted ratios of R_{rat} reduces the borehole inversion effects if the resistivity of the borehole fill/fluid remains relatively unchanged between data collection periods. R_{rat} is defined as (Daily et al., 1995):

$$R_{rat} = \left(\frac{R_{t2}}{R_{t1}}\right) * R_h$$

Eqn. 6.3

where: R_{t1} is the transfer resistance at time t_1, R_{t2} is the transfer resistance at a subsequent time t_2, and R_h is the transfer resistance for the comparable homogeneous resistivity distribution predicted by the forward model.

Figure 6.11 shows the results of the inverted R_{rat} values, where the baseline case has two boreholes with $BH \rho_{Contrast} = 0.01$, and the subsequent case also incorporates Target A_c (centered target) with $T\rho_{Contrast} = 0.01$. These were simulated to evaluate the condition of a target developing between measurement periods (e.g., a contaminant leak). Though showing a "cleaner" picture by reducing borehole effects significantly, the figure shows that the details of Target A_c are lost in comparison with the case of borehole inversion effects included (i.e., non-ratioed data). This image leads to the possibility that borehole inversion effects may actually be advantageous when the data are imaged both ways (single data sets plus ratioed data sets) depending on the size, shape, orientation and location of the target. Borehole inversion effects enhance the contrast of the target (Table 6.1) and more accurately represent its size in this case. In fact, the geometric mean resistivity distribution at Target A_c derived by inversion of R_{rat} values is actually 10% greater than the case of Target A_c without boreholes, whereby definition of the target is diminished. Inversion of R_{rat} values provides a means to differentiate anomalies from artifacts. One can qualitatively determine the degree of the borehole inversion effects by comparison of the data imaged both ways.
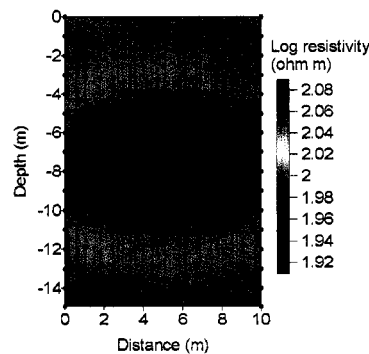
Figure 6.11. Image of inverted R_{rat} values, where R_{t1} has two boreholes with a $BH \rho_{Contrast} = 0.01$, and R_{t2} also incorporates Target A_c with a $T\rho_{Contrast} = 0.01$.

6.4.4 Shadow effects

Inversion artifacts may also result from the use of 2-D inversion codes for 3-D structures located outside the 2-D image plane. Development of inversion shadow effects is evaluated for an 8 m^3, target heterogeneity with $T\rho_{Contrast} = 0.01$ located completely out of the image plane (y=0 m) by distances of y=1 m (Target B), y=3 m (Target C) and y=5 m (Target D) (see Figure 6.8 for locations).

Modeled results for Target B are shown as images in Figure 6.12. Figure 6.12a shows the image for Target B$_c$ (centered in the x-direction between two columns of electrodes), and Figure 6.12b shows the image for Target B$_{nc}$ (2 m to the right of center) between the same two columns of electrodes. In both instances the resistivity low is a "shadow" of the target and is actually an artifact rather than an anomaly. The electric field is refracted out of the image plane as the current passes through the target. The 2-D inversion code interprets the refracted electric field as a change in the resistivity distribution causing a shadow of the target to be generated within the image plane. The location of the resistivity shadows fairly accurately locates the target in the x- and z-directions.

Table 6.1 lists calculated arithmetic-mean resistivity values within the image plane (y=0) at the center of Targets B and C in the x- and z-directions; there is no change from the homogeneous distribution with the inclusion of Target D. In comparison to the data for Target A, the shadow resistivities for Targets B and C are greater. Resolution of the shadow

a.   b.
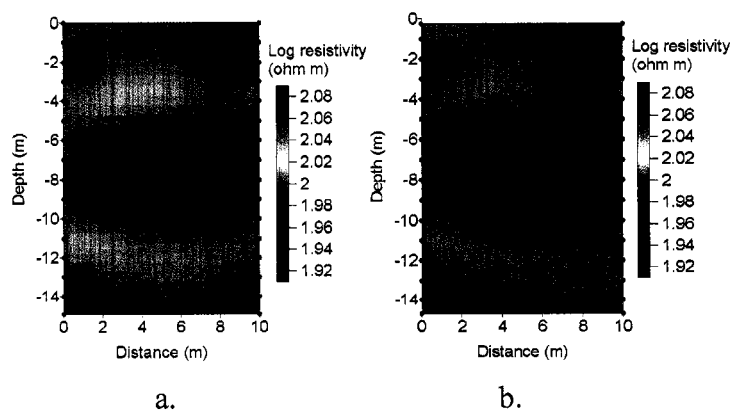
Figure 6.12. Image of shadow effects (resistivity low) caused by Target B (8 m^3 cube represented by box) with $T\rho_{Contrast} = 0.01$ out of y-plane by 1 m: a) Target B$_c$, b) Target B$_{nc}$.

decreases as the distance of the target out of the image plane increases. The shadow of Target B_{nc} has a slightly better resistivity accuracy than the shadow of Target B_c due to the closer electrode proximity. Target C results in less than 5% change from homogeneous conditions with the absence of the target (image not shown). Target C_{nc} causes essentially no change to the homogeneous resistivity distribution.

Figure 6.13 is a graph of the arithmetic mean resistivities calculated by the inversion model within the image plane for targets located at various distances out of the image plane. This graph illustrates the models response to Target B is affected more when the target is located nearer to the electrodes and less than 1.5 m out of the image plane. However, the shadow of Target C_c is detectable at 3 m outside the image plane unlike the Target C_{nc}.
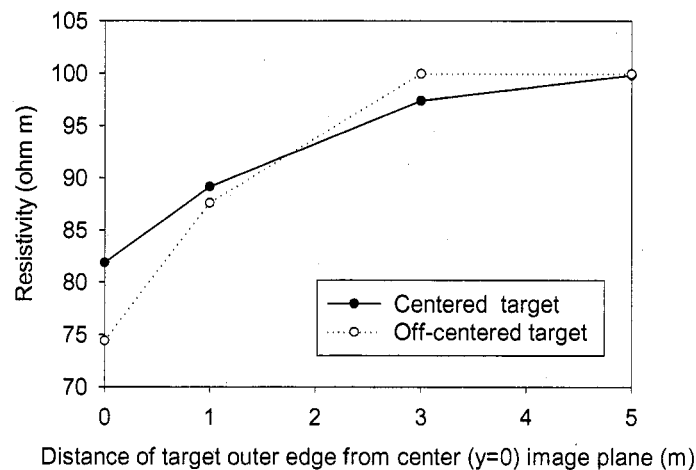
Figure 6.13. Graph of arithmetic mean resistivity within the image plane at the center of the target in the x- and z-directions for centered (x=4 to 6 m) and non-centered (x=2 to 4 m) targets. Actual target resistivities are 1 Ωm.

6.5 Conclusions

The 2-D inversion algorithm misinterpret the voltage distribution from a 3-D body; the resultant resistivities are then generated with inherent errors. The modeling results show that borehole inversion effects are proportional to current density (current per unit area of cross-section). Therefore, the effects increase as the resistivity contrast of the boreholes

increases and as the surface area of the boreholes increases. The algorithm may misrepresent the location of a target heterogeneity located between two boreholes or completely mask it altogether due to borehole inversion effects. Analysis of time-sequenced data sets as ratios helps to reduce borehole inversion effects. However, in some instances the existence of borehole inversion effects actually are advantageous and help to increase target recognition. Consequently, inverted ratioed data analyzed in conjunction with inverted non-ratioed data provide for an enhanced analysis.

Presence of a target heterogeneity located outside the image plane causes refraction of the electric field. The algorithm misinterprets the resultant change in the electric field as a change in the distribution of apparent resistivity within the image plane. Shadow effects are dependent upon the target location within the plane and distance away from the plane. The algorithm incorrectly represents the true homogeneous resistivity of the image plane through shadow effects and may result in misleading interretations.

References

Binley, A., Cassiani, G., Middleton, R., and Winship, P., 2002. Vadose zone flow model parameterisation using cross-borehole radar and resistivity imaging. Journal of Hydrology 267, 147-159.

Bear, J., Tsang, C-F., and de Marsily, G., 1993. Flow and Contaminant Transport in Fractured Rock. San Diego, CA: Academic Press.

Daily, W., and Ramirez, A., 1995. Electrical resistance tomography during in-situ trichloroethylene remediation at the Savannah River Site. Journal of Applied Geophysics 33, 239-249.

Daily, W., Ramirez, A., LaBrecque, D., and Barber, W., 1995. Electrical resistance tomography experiments at the Oregon Graduate Institute. Journal of Applied Geophysics, 33, 227-237.

deGroot Hedlin, C., and Constable, S. 1990. Occam's inversion to generate smooth, two-dimensional models from magnetotelluric data. Geophysics 55 (12), 1613-1624.

Keller, G.V., and Frischknecht, F.C., 1966. Electrical Methods in Geophysical Prospecting. Oxford [England]; New York: Pergamon Press.

Kemna, A., Vanderborght, J., Kulessa, B., Vereecken, H., 2002. Imaging and characterisation of subsurface solute transport using electrical resistivity tomography (ERT) and equivalent transport models. Journal of Hydrology 267, 125-146.

Osiensky, J.L., Nimmer, R.E., and Binley, A.M. 2004. Borehole cylindrical noise during hole-surface and hole-hole resistivity measurements. Journal of Hydrology 289 (1-4), 78-94.

Parkhomenko, E.I., 1967. Electrical Properties of Rocks. New York: Plenum Press.

Sasaki, Y., 1992. Resolution of resistivity tomography inferred from numerical simulation. Geophysical Prospecting 40, 453-463.

Shima, H., 1989. Effects on reconstructed images of surrounding resistivity structures in resistivity tomography. Expanded Abstracts with Biographies, Technical Program, International SEG Meeting, 59, 385-389.

Shima, H., 1992. 2-D and 3-D resistivity image reconstruction using crosshole data. Geophysics 57 (10), 1270-1281.

Singha, K., and Gorelick, S.M., 2005. Saline tracer visualized with three-dimensional electrical resistivity tomography: Field scale spatial moment analysis. Water Resources Research 41, W05023.

Slater, L.D., Binley, A., and Brown, D., 1997. Electrical imaging of fractures using ground-water salinity change. Ground Water 35 (3), 436-442.

Slater, L.D., 2005. Personnel communication.

Slater, L., Binley, A.M., Daily, W., and Johnson. R., 2000. Cross-hole electrical imaging of a controlled saline tracer injection. Journal of Applied Geophysics 44, 85-102.

Telford, W.M, Geldart, L.P., and Sheriff, R.E., 1990. Prospecting Geophysical Methods. Cambridge [England]; New York: Cambridge University Press.

Vanderborght, J., Kemna, A., Hardelauf, H., and Vereecken, H., 2005. Potential of electrical resistivity tomography to infer aquifer transport characteristics from tracer studies: A synthetic case study. Water Resources Research 41, W06013.

Zhou, B., and Greenhalgh, S.A., 2000. Cross-hole resistivity tomography using different electrode configurations. Geophysical Prospecting 48, 887-912.

CHAPTER 7. CONCLUSIONS AND RECOMMENDATIONS

7.1 Conclusions

7.1.1 Field Experiment

This study has shown that two out of the three electrical, geophysical methods tested are capable of the detection and delineation of an evolving conductive plume, and the subsequent dilution of the plume by controlled injection of tap water, and natural recharge in partially saturated, fractured basalt. Self potential (SP), mise-á-la-masse (MALM), and electrical resistance tomography (ERT) were used to follow the migration patterns of the injected fluids by examination of changes in voltages and resistivity. The field experimental results show that the injected KCl solution and subsequent tap water migrated away from the injection well during the radial-injection, tracer experiment.

The original hypothesis that addition of KCl solution to the vadose zone in fractured basalt would cause a definable SP anomaly to develop over time could not be proved. It was anticipated that SP's would be channeled preferentially into the KCl plume causing distinct distortions in the SP field when compared to the pre-plume baseline conditions. Because these anomalies did not develop, SP was not an effective tool to monitor the evolution of the slow growing KCl plume in the partially saturated vadose zone in fractured basalt because the signal caused by the plume was not strong enough or changes caused by the plume were overwhelmed by noise. Not surprisingly then, SP was not sensitive to the injection of tap water due to the resulting low conductivity contrast or the overwhelming noise.

The injection of a direct MALM current into the source of an evolving KCl plume in the vadose zone in fractured basalt allowed the plume dynamics to be mapped over time. Energization of the KCl plume through the KCl-source injection well allowed current to flow preferentially through the evolving plume in the direction of migration of KCl solution demonstrating electrical continuity via the injected fluid. Comparison of hole-surface MALM voltages with baseline voltages allowed the general patterns of plume growth to be mapped over time in two dimensions (x,y) reflecting the preferential flow-paths taken by the saline solution. This information is very beneficial given that only one borehole was

necessary to conduct the experiment. Hole-hole MALM delineated an apparent current pathway that developed in the injection well during the experiment. This current pathway was interpreted to be a preferential fluid pathway. Unfortunately, the threshold conductivity contrast needed for detection by hole-surface and hole-hole MALM did not develop during Phase 2 of the experiment because of a decreasing resistivity contrast caused by mixing of tap water and KCl solution within the fractures and basalt matrix.

Surface ERT, by providing a 3-D resistivity image, was able to offer complimentary information to some of the other methods on the evolutionary dynamics of the KCl plume dilution in a partially saturated vadose zone in fractured basalt. Although data collection periods differed among the various electrical methods used during this experiment, the 3-D nature of surface ERT provided comprehensive images of the subsurface conditions without disturbance to the subsurface. However, surface ERT data provided conflicting details that were not consistent with measured changes in hole-surface MALM voltages, and could be due to the insensitivity of MALM to the KCl dilution by tap water. This method is not practical for detecting small-scale features such as fracture locations, or for imaging at great depths, as the sensitivity of the method decreases with depth, and features become homogenized.

Cross-borehole ERT between an injection well containing the source material (i.e., tap water), and several nearby observation wells, in a vadose zone in fractured basalt provided detailed information near the wells on the evolutionary plume dynamics. Inversions of the transfer resistance data between the injection well and observation wells during the plume dilution by tap water allowed the vertical, spatial delineation of changes in resistivity along preferential current pathways from the injection well and into the observation wells. These changes in resistivity over time identified vertical distributions of fracture zones as preferential pathways for the migration of KCl solution as well as the dilution and redistribution of the KCl solution.

Application of electrical geophysical methods during the radial injection tracer test in partially saturated fractured basalt supplied valuable information on the hydrogeology of the field site. Behavior of the resistivity changes monitored over time signifies heavily fractured zones that form conduits for preferential flow of water through the subsurface

128

7.1.2 Cross-borehole ERT modeling

Hypothetical, ERT modeling allowed for the evaluation of 2-D, inversion model artifacts caused by the 2-D interpretations of 3-D targets centered within the image plane. The 3-D effects (artifacts) from boreholes intensify with a high resistivity contrast between the borehole fill and the host material, and with larger borehole diameters. These artifacts are caused by increasing preferential current flow up and down the borehole resulting in a decrease in current density near the electrode. Borehole inversion effects may cause misrepresentations of target heterogeneity locations where a target is introduced between the boreholes filled with material of different resistivity than the host medium; the target may be disguised completely by significant borehole inversion effects. Conversely, borehole inversion effects may actually enhance target heterogeneities in some circumstances as the artifact intensifies the target anomaly. A low-numbered, electrode, skip schedule can slightly reduce borehole inversion effects given the higher sensitivity nearer the electrodes. Inversions of ratioed time-series data significantly reduce borehole inversion effects to near elimination. It is advantageous to invert raw apparent resistivity values as well as ratios of time-sequenced data for a more insightful analysis. A good understanding of the potential ramifications of borehole inversion effects to data interpretation is crucial in ERT experiments when the details of a target heterogeneity are not known.

Evaluation of image artifacts from a 3-D target heterogeneity located outside an image plane was conducted by means of hypothetical, ERT modeling using a 2-D, inversion model. The 3-D effects from the target are greatest at small distances out of the image plane; the intensity of the artifact decreases with distance. These artifacts are a result of a distortion in the electric field by the heterogeneity whereby the model develops a resistivity distribution reflecting this distortion. Unlike borehole inversion effects where artifacts do not accurately represent a resistivity change in any direction, shadow effects for a target heterogeneity accurately represent a resistivity change in the x and z directions but position it incorrectly within the y-direction. Shadow effects escalate when the target is positioned nearer the column of electrodes resulting from an increased sensitivity nearer the electrodes. Shadow effects can be useful in field experiments when it is the intention of ERT to broadly detect subsurface contamination. However, precise identification of heterogeneity locations or

application of the data for hydrologic parameter calculations expose the problematic nature of shadow effects in ERT data analyses.

7.2 Recommendations

There are several recommendations of how to conduct the optimum electrical, geophysical field experiment:

1. If conducting a similar experiment, the injection well should be drilled prior to the other wells. MALM should then be performed two times, each with a different borehole-fill resistivity. Development of a pseudo-plume anomaly from contoured voltage ratios can be evaluated to establish the optimum placement of monitoring wells.

2. A slightly higher concentration tracer solution is suggested for better detection by electrical methods; although, taking into account density effects.

3. If conducting a pole-pole experiment, do not bundle the distant current wire to other wires to minimize current loss, and placement of distant electrodes as close to infinity as possible.

4. Use thick insulation wire to connect electrodes to the switch boxes along the cable (connected to the transmitter/receiver) to reduce current loss.

5. Install depth discrete sampling points and measure tracer concentrations from collected waters for comparison with geophysical data.

6. Based on prior knowledge of a site, conduct ERT model simulations to determine the optimal electrode spacing and skip schedule.

7. Analyze only ratioed ERT data if borehole inversion effects could be a problem from large diameter boreholes or high-contrasting resistivity fill with the host material.

8. Downhole, ERT electrodes should be installed in a core hole or in the smallest-diameter borehole possible if the borehole is fluid filled or will have a high-resistivity contrast backfill where non-ratioed, ERT data will be evaluated.

Suggestions for future work are:

1. To confirm the hydrologic analysis of water-level rises, measure water levels and electrical conductivity of the borehole waters during the same season to analyze for similar trends.

2. Conduct ERT field experiments with different borehole-fill resistivities to compare with the modeling results in Chapter 7.

APPENDIX 1. LETTERS OF REPUBLICATION PERMISSION

PERMISSION TO USE MATERIAL COPYRIGHTED BY
AMERICAN ASSOCIATION OF PETROLEUM GEOLOGISTS

AAPG COPYRIGHT PERMISSION NUMBER: __75006__ (Include this reference number with all payments.)

For: Robin Nimmer Ph.D. student , University of Idaho dissertation entitled "Electrical Characterization of a Three-Phase, Tracer, Injection Test" to be defended September 2005 the inclusion of:
DESCRIPTION OF ITEM: text of Nimmer and Osiensky article "Using Mise-à-la-Masse to delineate the migration of a conductive tracer in partially saturated basalt", AAPG DEG Environmental Geosciences, V.9/2 (June 2002) p. 81-87

We are in agreement UMI may supply single copies of this dissertation upon demand.

FEES:

PROCESSING FEE

$__0__ : This permission is granted contingent upon payment of this processing fee where one is assessed. This is not a license fee. A license fee may or may not be assessed in addition to a processing fee (please see next paragraph). Processing fees may not be required in all circumstances.

LICENSE FEE

A license fee of $__0__ is assessed for this usage.

TOTAL FEES PAYABLE: $__0__

WHERE TO SEND FEES

Please make checks or money orders payable to AAPG in U.S. funds, payable on a U.S. bank. Remit to: AAPG Permissions, P.O. Box 979, Tulsa, OK 74101-0979 USA. If paying by Visa, MC or American Express please include cardholder's name, card name, card number, expiry date, and a contact number (phone or fax). If you prefer, you may phone credit-card payment to (918) 560-9431. With all payments, please include the Copyright Permission Number at the top of this page to ensure proper credit.

PERMISSION

To the extent we hold copyright the permission granted in this letter is non-exclusive and for one-time use only of the copyrighted material cited in the attached request, and is subject to the following terms and conditions. Unless specifically authorized below, this permission does not include the use of the material in any other edition or derivative work, nor by any other means of reproduction. It does include permission to capture electronically or reproduce in digital format, sound tapes, motion pictures, or phonograph recordings. It does not include permission for use in abridgments or selections that may be made of or from the publication, nor for book club editions, nor for translations. Additional approval is required for any subsequent use of this material. The following terms also apply this permission:

1. The permission to use this material is contingent upon receipt of all fees assessed by this document within 90 days after the date of this permission. If such payment is not made, this permission will be void. If no fees are assessed no further communication is necessary.

2. As a condition of the grant of permission contained in this letter, AAPG requires the following:

   (a) a full citation in your bibliography for each AAPG publication from which a table or figure of text is taken;

   (b) in figure and title captions a statement or citation including the author, identification of the AAPG publication from which the figure or table was taken,

   (c) you must use the identical copyright notice as it appears in our publication; i.e. "AAPG©[date], and the phrase "reprinted by permission of the AAPG whose permission is required for further use"

3. This permission is for one edition only; permission must be requested specifically for any subsequent editions, formats, or derivations.

4. Non-exclusive permission is granted and is valid throughout the world in the English language only, unless otherwise stated here:_____

5. This permission applies only to material for which AAPG holds copyright, and does not apply to any part or selection copyrighted by another publisher. It is the responsibility of each requester to determine the source of all material and to obtain necessary copyright permission(s) from all appropriate sources. Carefully read the credits and citations accompanying the original publication of the desired material to determine these issues.

6. As a matter of courtesy, it is always a good idea to notify each author whose material you are using, preferably with a copy of the proposed usage or alteration.

7. If more than 15% of your forthcoming work (exclusive of index and bibliography) is composed of material from AAPG publications, this permission is automatically void; please request a new permission with an estimate of the total percentage.

8. This permission is void if publication does not take place within 36 months from the date written at the end of this form. A new request must be submitted at that time.

9. Material covered by this permission may not be used in any way that could cause it to enter the public domain by means of or because of this permission. All publication permitted by this permission must include full protection of the copyright status of the material owned by the American Association of Petroleum Geologists.

10. A complimentary copy of the publication for the AAPG Foundation Library would be appreciated but is not mandatory. The AAPG Foundation Library is a non-profit entity serving AAPG members as well as the larger geological community. All complimentary copies will be gratefully acknowledged.

Authorized by: _____ Date: 28 July 2005
        Mary C. Grosvald, AAPG Permissions

ELSEVIER
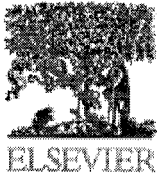
1 April 2005   Our ref: HG/QC/APR05/J013

Mrs. Robin Nimmer
University of Idaho
nimm9536@uidaho.edu

Dear Mrs. Nimmer

JOURNAL OF HYDROLOGY, Vol 267, No 3-4, 2002, pp 258-272, Nimmer et al, "Direct Current and..."

As per your email dated 15 March 2005, we hereby grant you permission to reprint the aforementioned material at no charge **in your thesis** subject to the following conditions:

1. If any part of the material to be used (for example, figures) has appeared in our publication with credit or acknowledgement to another source, permission must also be sought from that source. If such permission is not obtained then that material may not be included in your publication/copies.

2. Suitable acknowledgment to the source must be made, either as a footnote or in a reference list at the end of your publication, as follows:

"Reprinted from Publication title, Vol number, Author(s), Title of article, Pages No., Copyright (Year), with permission from Elsevier".

3. Reproduction of this material is confined to the purpose for which permission is hereby given.

4. This permission is granted for non-exclusive world **English** rights only. For other languages please reapply separately for each one required. Permission excludes use in an electronic form. Should you have a specific electronic project in mind please reapply for permission.

5. This includes permission for UMI to supply single copies, on demand, of the complete thesis. Should your thesis be published commercially, please reapply for permission.

Yours sincerely
Helen Gainford
Rights Manager

Taylor & Francis
Taylor & Francis Group

325 Chestnut Street, Suite 800
Philadelphia, PA 19106
Tel: 215 625-8900
Fax: 215 625-2940
elaine.inverso@taylorandfrancis.com

REPUBLICATION PERMISSION AGREEMENT AND INVOICE # J1614

April 12, 2005

Robin E. Nimmer
1629 E. 6th Street
Moscow, ID 83843

We are pleased to grant permission to you for the republication of:

Selection: **Charged Body Potential Monitoring of an Electrolyte Plume Emanating from a Dripping Source, Pages 737-752**

From: **Journal of Environmental Science and Health, Part A, 2003, 38 (5)**

Within the following publication: **PhD Thesis**

Location: **University of Idaho**

Pub date: **2005**

Format(s): Print:☒ CD-ROM:☐ E-Book:☐ Web Site:☐ Elec Storage:☐

This permission is subject to the following conditions:

1. This permission is a non-transferable grant for **English** language use, as described below, in the following territory only: **North America.**

2. Payment (nonrefundable) of **$0** is due within 4 months of the date of this grant. If payment is not received by then, this permission will become void. Please make payment payable to the Permissions Dept. at the address above. Our tax ID # is 13-315-0750.

3. Each copy/electronic transmission containing our material must bear the following credit line:

   Copyright (Insert Copyright Year) From (Insert Title) by (Insert Author Name). Reproduced by permission of Taylor & Francis Group, LLC, http://www.taylorandfrancis.com

4. Permission is granted on a one-time, non-exclusive basis.

5. If applicable, this permission extends only to the usage specified above during the time period specified above. Any other use (including re-use) requires additional permission from Taylor & Francis Group, LLC.

6. <u>This permission extends only to material owned or controlled by us</u>. Please check the credits in our book for material which the copyright is not owned or controlled by us. You should apply to the owner of the copyright for permission use material that is not ours.

7. Permission will be void if Taylor & Francis material exceeds 10% of the total pages in your publication.

The terms of the above permission are accepted and agreed to:

Robin Nimmer   _Robin Nimmer_   _July 25, 2005_
Agreed (please print name and sign):   Date

For Taylor & Francis Group, LLC
Elaine Inverso, Permissions Coordinator

APPENDIX 2. NON-ELECTRICAL, FIELD EXPERIMENT DATA

Water level elevation (m) data

Days since KCI injection	ES1	ES2	ES3	ES4	ES5	ES6	ES7	Inj Well
-12	776.415	776.473	776.749	777.02	777.017	777.081	776.703	
13	776.479	776.181	776.776	776.95	777.017	777.057		779.995
41	776.784	776.751	776.92	777.005	777.41	777.761	776.816	779.995
44	776.781	776.754	776.908	777.029	777.414	777.401	776.804	779.995
46	776.714	776.723	776.889	777.023	777.386	777.203	776.776	779.995
57	776.699	776.778	776.944	777.151	777.538	777.292	776.984	779.995
60	776.58	776.687	776.853	777.039	777.481	777.304	776.853	779.995
68	776.491	776.744	776.938	777.093	777.49	777.45	777.033	779.995
74	776.775	776.799	776.99	777.087	777.487	777.627	777.069	779.995
76	776.763	776.866	777.063	777.148	777.508	777.538	777.157	779.995
80	776.784	776.848	777.066	777.13	777.496	777.453	777.173	779.995
91	777.058	777.735	777.938	779.035	778.959	778.669	778.188	779.995
92	777.046	777.586	777.865	778.995	778.919	778.523	778.084	779.995
93	777.022	777.549	777.904	778.944	778.886	778.453	778.023	779.995
95	777.144	777.619	778.06	778.901	778.88	778.392	778.102	779.995
96	777.144	777.607	778.041	778.858	778.886	778.377	778.078	779.995
99	777.162	777.503	777.993	778.73	778.855	778.352	778.157	779.995
100	777.189	777.506	778.069	778.883	778.852	778.809	778.288	779.995
101	777.205	777.604	778.157	778.989	778.953	778.916	778.788	779.995
102	777.193	777.924	778.288	779.175	779.133	779.221	779.264	779.995
103	777.208	777.93	778.401	779.194	779.255	779.087	779.169	779.995
104	777.211	777.833	778.407	779.117	779.166	778.922	778.989	779.995
106	777.36	777.869	778.511	779.154	779.151	778.901	778.953	779.995
107	777.375	777.881	778.489	779.133	779.111	778.886	778.919	779.995
110	777.33	777.942	778.578	779.206	779.288	779.166	779.2	779.995
111	777.394	777.945	778.614	779.355	779.535	779.27	779.474	779.852

Days since KCl injection	ES1	ES2	ES3	ES4	ES5	ES6	ES7	Inj Well
114	777.82	778.137	778.721	779.474	780.282	779.45	780.193	779.791
115	777.537	778.137	778.715	779.456	780.288	779.422	780.209	779.788
116	777.503	778.131	778.657	779.447	780.288	779.389	780.093	779.733
117	777.479	778.122	778.657	779.416	780.279	779.34	780.044	779.748
118	777.482	778.159	778.611	779.379	780.257	779.282	779.928	779.782
123	777.449	778.354	778.666	779.346	780.526	779.352	780.129	780.071
124	777.598	778.296	778.621	779.322	780.486	779.285	779.959	780.017
125	777.589	778.278	778.578	779.224	780.446	779.255	779.84	779.98
126	777.592	778.211	778.572	779.16	780.455	779.187	779.657	779.934
128	777.586	778.299	778.547	779.093	780.44	779.139	779.575	779.873
130	777.586	778.336	778.489	778.947	780.428	779.038	779.398	779.849
132	777.634	778.476	778.496	778.965	780.611	779.087	779.52	779.824
136	777.741	778.777	778.621	779.184	780.702	779.3	779.626	779.837
139	777.921	778.735	778.77	779.34	780.833	779.581	779.885	779.907
142	777.955	778.951	778.791	779.273	780.586	779.413	779.632	779.913
144	777.793	778.686	778.602	779.032	780.276	779.166	779.337	779.913
146	777.699	778.47	778.483	778.794	780.117	778.974	779.169	779.858
149	777.732	778.235	778.48	778.736	780.038	778.913	779.053	779.794
159	777.552	777.833	778.108	778.371	779.319	778.489	778.468	779.547
167	777.354	777.552	777.834	778.02	778.773	778.139	778.081	779.334
172	777.211	777.363	777.663	777.822	778.343	777.935	777.849	779.16

Electrical conductivity measurements of borehole water samples

Electrical conductivity of borehole waters was measured using a Corning Checkmate 90 Meter Module and conductivity sensor. No data indicates there was not enough water in the borehole for sample collection.

Days since saline injection	ES1	ES2	ES3	ES4	ES5	ES6	ES7	Inj Well
-1	912	1227	970	2260			1477	1153
1	906	1223	907	2140			1399	6010
12	894	1228	867	2280			1542	6010
38	898	1223	884	2070	1924	1221	1460	6010
57	853	1224	987	2170	1836	1854	1649	6050
78	837	1404	1620	2120	1726	1612	2130	294
85	916	1336	2120	1845	1586	1477	1990	
95	848	1217	1128	968	1437	1111	1460	428
107	915	1038	984	899	1105	1080	1287	546
111	959	979	926	926	1091	1057	1336	542
124	925	845	927	916	713	1007	1162	680
139	857	776	935	955	652	984	1122	801
174	926	989	1058	967	938	932	1101	985

141

Precipitation data

Precipitation data in water equivalents for Moscow were provided by the Idaho State Climatologist, Russell J. Qualls.

Days since KCL inj	cm of rain		Days since KCL inj	cm of rain		Days since KCL inj	cm of rain		Days since KCL inj	cm of rain
-5	0		19	2.6416		43	0.0127		67	0.0127
-4	0		20	2.2098		44	0.0127		68	0.2286
-3	0		21	0.0508		45	0		69	0.5334
-2	0.0762		22	0		46	0.0127		70	0
-1	0.0254		23	0.0127		47	0		71	0.381
0	0.6858		24	0.5334		48	0		72	0
1	0		25	0.4572		49	0		73	0
2	0.0254		26	2.0066		50	0.0127		74	0
3	0.0762		27	0		51	0.0127		75	0.2286
4	0.0508		28	0		52	0.0127		76	0.0254
5	0.127		29	0.2286		53	0.0127		77	0.0254
6	0		30	0.5588		54	0		78	0.0127
7	0.1524		31	0.6858		55	0.1778		79	0.0127
8	0		32	0		56	0.4572		80	0.8128
9	0		33	0.4572		57	0.1016		81	0.0127
10	0.1016		34	0.0127		58	0.0508		82	0.0127
11	0.889		35	1.1176		59	1.4478		83	0
12	0		36	1.1684		60	0		84	0
13	0.1524		37	0.0762		61	0		85	0
14	0.508		38	0.5842		62	0.0127		86	0.3048
15	0.4572		39	2.2606		63	0.2794		87	0.4572
16	0.0127		40	0.4826		64	0.3048		88	2.0574
17	0.0127		41	0.0254		65	0.1778		89	0.0508
18	0.2794		42	1.1176		66	0.254		90	0.0127

142

Days since KCL inj	cm of rain	Days since KCL inj	cm of rain	Days since KCL inj	cm of rain	Days since KCL inj	cm of rain
91	0.0127	122	0.0762	153	0.0508		
92	0.3048	123	0	154	0		
93	0.0127	124	0.0508	155	0		
94	0	125	0	156	0		
95	0.1524	126	0.3556	157	0		
96	0	127	0.0127	158	0		
97	0.4826	128	0.0127	159	1.2192		
98	0.2032	129	0.3556	160	1.1684		
99	0.1524	130	0.1778	161	0.7112		
100	1.0414	131	0.9144	162	0.0508		
101	0.3556	132	1.143	163	0		
102	0	133	0.0508	164	0		
103	0	134	0.5842	165	0		
104	0	135	0.4826	166	0		
105	0	136	0.0254	167	0		
106	0	137	0	168	0.2794		
107	0.3048	138	2.1082	169	0		
108	0.2794	139	0	170	0		
109	1.9304	140	0	171	0.3302		
110	0.0127	141	0	172	0		
111	0	142	0	173	0		
112	0.0762	143	0.3048	174	0.3048		
113	0.4572	144	0.0127	175	0		
114	0.0508	145	0	176	0		
115	0.127	146	0				
116	0	147	0				
117	0.0762	148	0				
118	0.0127	149	0				
119	0.1016	150	0.0127				
120	0.6096	151	0				
121	0.5842	152	1.1176				

Soil temperature and soil suction data

Soil suction measurements were collected by a tensiometer located 13 m east of the injection well. A "Quick Draw" soil moisture probe series 2900 was used for data collection. The porous ceramic probe tip was located 15 cm below land surface. Soil temperature measurements were collected using an electronic soil temperature meter with electrodes located 12 m west of the injection well. The electrodes were located 15 cm below land surface.

Days since KCl inj	Soil Temp. (°C)	Soil Moisture (cb)		Days since KCl inj	Soil Temp. (°C)	Soil Moisture (cb)
3	6.93	18		104	0.35	6.5
6	8	32		106	1.75	4
7	9.83	26.5		116	3.75	2.5
11	7.4	15		128	4.8	2.2
12	5.6	27				
17	2.7	30				
18	4.3	30.5				
25	5.5					
27	3.15					
28	2.8					
34	2.5	4.5				
35	1.45	2.5				
44	2.3	4				
46	3.4	3.2				
61	1	0.8				
66	2.9					
68	1.6	4.2				
74	2.5	2				
89	1	1.3				
97	2.9	3.5				
99	2.3	5.5				

Paradise Creek water elevation data

Stream stage measurements for Paradise Creek were collected at Paradise Creek Gage Station number 13346800 operated by the United States Geological Survey (USGS) (see Figure 1.1). The gauging station is located at the University of Idaho, approximately 240 m almost due east of the field site. Fifteen-minute unit values are available upon request from the Hydrographer, SW Unit Chief, USGS, WRD, Idaho District, 208 387-1366.

Neutron probe data

Standardized counts of the neutron probe data are listed below. Measurements were collected using a 503DR probe. There are no data for ES2, ES3 and ES4 at t=41 d after KCl injection due to a dead battery within the neutron probe. No data elsewhere indicates the head within the well was too high for data collection.

	Days since KCl injection				
Elev (m) within ES1	-2	13	41	115	123
779.305	0.87988	0.862198	0.8598323	1.046711	1.062319
779.005	0.863442	0.8587104	0.8677905	1.029078	1.040464
778.705	0.902568	0.8809969	0.8905528	1.058325	1.068038
778.405	0.918322	0.8917149	0.9014205	1.034588	1.036196
778.105	0.875599	0.8798911	0.8851617	0.97177	0.982329
777.805	0.948202	0.9368833	0.9370187		
777.505	0.911729	0.9138312	0.9186206		
777.205	0.900685	0.8015481	0.9344515		
776.905	0.954623	0.9476012			

	Days since KCl injection				
Elev (m) within ES2	-2	13	41	115	123
779.2551	0.824572	0.7685437	0.8119973	1.182859	1.188663
778.9551	0.848288	0.7684587	0.8438302	1.180485	1.182858
778.6551	0.858219	0.8340422		1.235164	1.24825
778.3551	0.852568	0.9372235		1.135809	1.161943
778.0551	0.936216	1.0086764		1.215158	
777.7551	1.005137	1.0724736			
777.4551	1.082277	1.044573			
777.1551	1.04649	1.0412555			
776.8551	1.047774	0.7481286			
776.5551	0.760017				

146

	Days since KCl injection				
Elev (m) within ES3	-2	13	41	115	123
779.0562	1.046918	1.0281558		1.398016	1.313215
778.7562	1.063442	1.0563967			
778.4562	1.029795	1.0124192			
778.1562	1.074914	1.0539299			
777.8562	1.01464	1.0079109			
777.5562	0.82363	0.8160088			

	Days since KCl injection				
Elev (m) within ES4	-2	13	41	115	123
779.1858	1.034418	1.0242429			
778.8858	0.876627	0.8617727			
778.5858	1.044606	1.0363219			
778.2858	0.922089	0.9117047			
777.9858	1.175257	1.1589826			
777.6858	1.176113	1.1673188			
777.3858	1.146661	0.977033			

	Days since KCl injection				
Elev (m) within ES5	-2	13	41	115	123
779.7532	0.895719	0.8980095	0.9032175		
779.4532	0.927055	0.9369684	0.9400993		
779.1532	0.946747	0.9381592	0.9442067		
778.8532	1.034846	1.0217761	1.0339723		
778.5532	0.806421	0.7999319	0.8215814		
778.2532	0.738699	0.7354542	0.7496149		
777.9532	0.745976	0.7443858	0.776827		
777.6532	1.138442	1.1419701			

	Days since KCl injection				
Elev (m) within ES6	-2	13	41	115	123
779.3216	0.884675	0.8746172	0.9670546		
779.0216	0.944777	0.9402007	1.0155742		
778.7216	0.747089	0.741834	0.7841862		
778.4216	0.70762	0.7065328	0.8003594		
778.1216	0.726969	0.7159748			
777.8216	0.868836	0.8588806			
777.5216	1.36387	1.3385505			

	Days since KCl injection				
Elev (m) within ES7	-2	13	41	115	123
779.956	0.867723	0.864835	0.9044155		
779.656	0.862842	0.8529262	0.8957727		
779.356	0.879366	0.8782749	0.9080096		
779.056	0.815582	0.8154134	0.8105425		
778.756	0.898545	0.9022627	0.9287181		
778.456	0.937757	0.928377	0.9371898		
778.156	0.923716	0.8821878	0.9428376		
777.856	0.934932	0.9311841	0.9472018		
777.556	0.77363	0.7678632	0.7779394		
777.256	0.717551	0.7957639	0.711963		
776.956	0.883562	0.8692583	0.9555023		